

FILE COPY

6

AD-A216 864

SAIC 89/1555

**NUMERICAL MODELING OF Pn GEOMETRIC SPREADING AND
EMPIRICALLY DETERMINED ATTENUATION OF Pn AND Lg
PHASES RECORDED IN EASTERN KAZAKHSTAN**

Thomas J. Sereno, Jr.

Science Applications International Corporation
10260 Campus Point Drive
San Diego, California 92121

August 1989

Semiannual Technical Report
1 January 1989 to 30 June 1989

The views and conclusions contained in this document are those of the authors and should not be interpreted as representing the official policies, either expressed or implied, of the Defense Advanced Research Projects Agency or the US Government.

DTIC
S ELECTE D
JAN 11 1990
B

Sponsored By:

Defense Advanced Research Projects Agency (DARPA)
Nuclear Monitoring Research Office (NMRO)
Seismic Detection Capability Modeling

ARPA Order No. 4511 (Amendment 19)

Issued by AFTAC under Contract F08606-88-C-0033.

DISTRIBUTION STATEMENT A
Approved for public release;
Distribution Unlimited

90 01 10 158

**NUMERICAL MODELING OF Pn GEOMETRIC SPREADING AND
EMPIRICALLY DETERMINED ATTENUATION OF Pn AND Lg
PHASES RECORDED IN EASTERN KAZAKHSTAN**

Thomas J. Sereno, Jr.

Science Applications International Corporation
10260 Campus Point Drive
San Diego, California 92121

August 1989

Semiannual Technical Report
1 January 1989 to 30 June 1989

The views and conclusions contained in this document are those of the authors and should not be interpreted as representing the official policies, either expressed or implied, of the Defense Advanced Research Projects Agency or the US Government.

Sponsored By:

Defense Advanced Research Projects Agency (DARPA)
Nuclear Monitoring Research Office (NMRO)
Seismic Detection Capability Modeling

ARPA Order No. 4511 (Amendment 19)

Issued by AFTAC under Contract F08606-88-C-0033.

REPORT DOCUMENTATION PAGE

1a. REPORT SECURITY CLASSIFICATION Unclassified		1b. RESTRICTIVE MARKINGS	
2a. SECURITY CLASSIFICATION AUTHORITY		3. DISTRIBUTION/AVAILABILITY OF REPORT Approved for public release, distribution unlimited	
2b. DECLASSIFICATION/DOWNGRADING SCHEDULE			
4. PERFORMING ORGANIZATION REPORT NUMBER(S) SAIC-89/1555		5. MONITORING ORGANIZATION REPORT NUMBER(S)	
6a. NAME OF PERFORMING ORGANIZATION Science Applications International Corporation	6b. OFFICE SYMBOL (if applicable)	7a. NAME OF MONITORING ORGANIZATION Air Force Technical Applications Center/TTR	
6c. ADDRESS (City, State, and ZIP Code) 10260 Campus Pt. Drive San Diego CA 92121		7b. ADDRESS (City, State, and ZIP Code) HQ AFTAC/TTR Patrick Air Force Base FL 32925-6001	
8a. NAME OF FUNDING/SPONSORING ORGANIZATION Defense Advanced Research Projects Agency	8b. OFFICE SYMBOL (if applicable) DARPA	9. PROCUREMENT INSTRUMENT IDENTIFICATION NUMBER F08606-88-C-0033,	
8c. ADDRESS (City, State, and ZIP Code) 1400 Wilson Blvd. Arlington VA 22209		10. SOURCE OF FUNDING NUMBERS	
		PROGRAM ELEMENT NO. 62714E	PROJECT NO. DT/8121
		TASK NO. SOW 3.2	WORK UNIT ACCESSION NO.
11. TITLE (Include Security Classification) Numerical Modeling of Pn Geometric Spreading and Empirically Determined Attenuation of Pn and Lg Phases Recorded in Eastern Kazakhstan			
12. PERSONAL AUTHOR(S) Thomas J. Sereno, Jr.			
13a. TYPE OF REPORT Semiannual #1	13b. TIME COVERED FROM 1/1/89 TO 6/30/89	14. DATE OF REPORT (Year, Month, Day) 1989 August	15. PAGE COUNT 116
16. SUPPLEMENTARY NOTATION			
17. COSATI CODES		18. SUBJECT TERMS (Continue on reverse if necessary and identify by block number)	
FIELD	GROUP	Regional Seismology, Seismic Moment, Synthetic Seismograms, NRDC Seismic Stations, Generalized Inversion, Elastic and Anelastic Models	
8	11		
19. ABSTRACT (Continue on reverse if necessary and identify by block number)			
<p>This report summarizes two studies of regional wave attenuation. The first is a theoretical study of the dependence of P_n geometric spreading on the velocity gradient in the upper mantle. This is important because most methods for estimating P_n attenuation require assumptions regarding geometric spreading. It is found that P_n attenuation is very sensitive to the velocity gradient in the upper mantle. For example, the P_n amplitude at 1000 km is a factor of 20 larger for a model with a weak velocity gradient (equivalent to the earth-flattening transformation of a homogeneous upper mantle) than for a model consisting of layer over an infinite halfspace. Also, P_n geometric spreading is frequency-dependent for an upper mantle model with a simple linear velocity gradient. This is because the P_n waveform resembles the interference head wave at distances within a few hundred kilometers of the critical distance, but at</p>			
20. DISTRIBUTION/AVAILABILITY OF ABSTRACT <input type="checkbox"/> UNCLASSIFIED/UNLIMITED <input checked="" type="checkbox"/> SAME AS RPT. <input type="checkbox"/> DTIC USERS		21. ABSTRACT SECURITY CLASSIFICATION Unclassified	
22a. NAME OF RESPONSIBLE INDIVIDUAL Dr. Dean A. Caluter		22b. TELEPHONE (Include Area Code) (407) 494-5263	22c. OFFICE SYMBOL AFTAC/TTR

longer ranges is dominated by the mantle turning ray. Thus, methods that assume frequency-independent geometric spreading (e.g., spectral ratio methods) can lead to overestimates of Q if velocity increases with depth in the upper 50-100 km of the mantle.

The second study is an empirical parameterization of regional wave spectra recorded near the eastern Kazakhstan nuclear explosion test site. The results are compared to a similar parameterization of data recorded by the NORESS array in Norway. It is found that the attenuation of Lg spectra between 0.5 and 2.5 Hz in eastern Kazakhstan is very similar to the Lg attenuation observed at NORESS. It is also found that the single-station ambient noise levels in eastern Kazakhstan are similar to the array-averaged noise levels at NORESS. The Pn spectra between 1 and 10 Hz in eastern Kazakhstan are similar to the Pn spectra recorded at NORESS at similar distances. However, the absolute levels appear to be as much as a factor of two higher in eastern Kazakhstan for fixed source moment. Therefore, the magnitude thresholds for detecting Pn may be as much as 0.3 higher in Scandinavia than in eastern Kazakhstan. It is uncertain which of these Pn models more accurately describes the average attenuation in the Soviet Union, but the comparison gives a measure of the amount of regional variability that can be expected.



Accession For	
NTIS GRA&I	<input checked="" type="checkbox"/>
DTIC TAB	<input type="checkbox"/>
Unannounced	<input type="checkbox"/>
Justification	
By _____	
Distribution/	
Availability Codes	
Dist	Avail and/or Special
A-1	

Table of Contents

LIST OF FIGURES	v
LIST OF TABLES	xi
1. INTRODUCTION	1
1.1 Project Objectives	1
1.2 Current Status	1
1.3 Outline of the Report	2
2. NUMERICAL MODELING OF Pn GEOMETRIC SPREADING	5
2.1 Introduction	5
2.2 Approach	5
2.3 Results for Elastic Earth Models	5
2.3.1 <i>Crustal and Upper Mantle Velocity Models</i>	5
2.3.2 <i>Broadband Pn Amplitudes</i>	6
2.3.3 <i>Frequency Dependence of Pn Geometric Spreading</i>	10
2.4 Results for an Anelastic Earth Model	18
2.5 Implications for Q Estimation	18
2.6 Discussion	25
3. ATTENUATION OF Pn AND Lg PHASES RECORDED IN EASTERN KAZAKHSTAN	27
3.1 Introduction	27
3.2 Event and Station Locations	27
3.3 Data Processing	31
3.4 Attenuation and Source Parameters for Regional Phases	32
3.4.1 <i>Lg Inversion Results</i>	35
3.4.2 <i>Pn Inversion Results</i>	41
3.5 Noise Spectra	45
3.6 Comparison to NORESS Data	45
3.7 Summary	48
4. CONCLUSIONS	53
ACKNOWLEDGMENTS	55

REFERENCES	57
APPENDIX A: NRDC WAVEFORMS	61
APPENDIX B: NRDC SPECTRA AND INVERSION RESULTS	83
DISTRIBUTION LIST	109

LIST OF FIGURES

	Page
Figure 2.1. Velocity models used in the synthetic seismogram calculations. The solid curve is the earth-flattening transformation for a homogeneous upper mantle. Note the break in the velocity axis.	8
Figure 2.2. Temporal P_n displacement amplitude (1–15 Hz) as a function of epicentral distance for the three elastic earth models. The solid curve is the analytic attenuation of a canonical head wave scaled to the calculated amplitude for Model 1 at 200 km.	9
Figure 2.3. Record section plot of P_n particle velocity for (a) Model 1, (b) Model 2 and (c) Model 3. Travel times are reduced at 8.1 km/s. The amplitudes of each trace are scaled independently.	11
Figure 2.4. Perspective plot of P_n displacement spectra as a function of epicentral distance computed for (a) Model 1, (b) Model 2 and (c) Model 3.	14
Figure 2.5. (a) Schematic ray diagram for the primary turning ray (P) and the first whispering gallery phase ($WG1$). (b) Record section plot of P_n particle velocity for Model 3 reduced at 8.1 km/s. Travel-time curves for P , $WG1$, and the head wave are superimposed.	17
Figure 2.6. Temporal P_n amplitude (1–15 Hz) for Models 2 and 4. The solid curve is the analytic attenuation of a canonical head wave.	19
Figure 2.7. Record section plot of P_n particle velocity for Model 4. Travel times are reduced at 8.1 km/s. The amplitudes of each trace are scaled independently.	20
Figure 2.8. Perspective plot of P_n displacement spectra as a function of epicentral distance computed for Model 4.	21
Figure 3.1. Map showing the station locations (triangles) and event locations (numbers) for the NRDC data set. The numbers correspond to the event numbers in Table 3.2.	30
Figure 3.2. P_n geometric spreading. The solid curve is the P_n attenuation with distance at 1.25 Hz calculated for an elastic earth model with upper mantle velocity gradient equivalent to the earth-flattening transformation of a homogeneous medium (Model 2, Section 2). The dashed curve plots a power law distance dependence $r^{-1.25}$ determined by a least squares fit to the synthetic P_n attenuation.	34

Figure 3.3. $L_g Q(f)$ models consistent with the NRDC observations. The value of $L_g Q$ at 1 Hz (Q_0) is plotted against the exponent of a power law frequency dependence (η). These models combine with different source levels to produce data variances that differ by less than 1%. 36

Figure 3.4. Derived source levels (S_0) for (a) $L_g Q(f) = 650$ and (b) $L_g Q(f) = 345f^{0.4}$. The event numbers are from Table 3.2. Events recorded at multiple stations have an S_0 estimate from each station. Note that the higher Q_0 model reduces the variance in the derived source levels from multiple station observations. 37

Figure 3.5. Moment versus magnitude for presumed earthquakes in the NRDC data set. The moments are calculated from the L_g source levels using (3.5) and are plotted against the m_b reported in the PDE Bulletin (Events 1, 2, 3, 5, and 9 in Table 3.2). The solid lines are moment versus magnitude relations determined in previous studies (Table 3.3). The dashed horizontal lines are moments of earthquakes not reported in the PDE Bulletin. 39

Figure 3.6. $P_n Q(f)$ models consistent with the NRDC observations. The value of $P_n Q$ at 1 Hz (Q_0) is plotted against the exponent of a power law frequency dependence (η). These models combine with different source levels to produce data variances that differ by less than 1%. 42

Figure 3.7. Derived source levels (S_0) for (a) $P_n Q(f) = 1175$ and (b) $P_n Q(f) = 300f^{0.5}$. The event numbers are from Table 3.2. Events recorded at multiple stations have an S_0 estimate from each station. 43

Figure 3.8. Moment versus magnitude for presumed explosions in the NRDC data set. The moments are calculated from the P_n source levels using (3.6) and are plotted against L_g magnitude (Events 11, 13, 14, 16, 18, 19–21 in Table 3.2). The asterisks are moments calculated for the $P_n Q(f) = 300f^{0.5}$ model and the squares are for the $P_n Q(f) = 1175$ model. Note that the moments for the lower Q_0 model are about a factor of 2 higher than the moments associated the higher Q_0 model. The solid line is the explosion moment versus magnitude relation determined by *Sereno et al.* [1988] from NORESS observations. 44

Figure 3.9. Ambient noise displacement spectra for a 5-s window. The solid curve is the average noise spectrum at the three NRDC stations calculated from 26 samples taken prior to P_n . The dashed curves indicate one standard deviation. The dotted curve is the average ambient noise spectrum at NORESS based on 43 samples taken prior to P_n [*Henson and Bache, 1988*]. 46

- Figure 3.10. Theoretical Lg spectra at 800 km for a magnitude 3.0 event based on the inversion results using the NRDC (solid) and NORESS data (dashed). The bottom curve is the average NORESS ambient noise scaled to the Lg signal window length at 800 km. This curve is plotted only for reference. The actual Lg spectrum is contaminated by the coda of previous arrivals which is larger than the ambient noise. 47
- Figure 3.11. Theoretical Pn spectra at 800 km for a magnitude 3.0 explosion based on the inversion results using the NRDC (solid curves) and NORESS data (dashed). The results for two NRDC Pn models are plotted since parameter trade-offs cannot be resolved on the basis of source moment. Model parameters are listed in Table 3.4. The bottom curve is the average NORESS ambient noise scaled to a 10-s window length. 49
- Figure A.1. Waveforms for Event 1 (Table 3.2). This is an m_b 4.3 earthquake reported in the PDE Bulletin. The calibration values are 0.012781 and 0.012929 nanometers per digital count for stations KKL and BAY, respectively. 62
- Figure A.2. Waveform for Event 2 (Table 3.2). This is an m_b 4.3 earthquake reported in the PDE Bulletin. The calibration value is 0.012929 nanometers per digital count for station KKL. 63
- Figure A.3. Waveform for Event 3 (Table 3.2). This is an m_b 4.6 earthquake reported in the PDE Bulletin. The calibration value is 0.012929 nanometers per digital count for station KKL. 64
- Figure A.4. Waveform for Event 4 (Table 3.2). The event type is unknown. The calibration value is 0.012929 nanometers per digital count for station KSU. 65
- Figure A.5. Waveforms for Event 5 (Table 3.2). This is an m_b 4.6 earthquake reported in the PDE Bulletin. The calibration values are 0.411528 and 1.63832i nanometers per digital count for stations KKL and BAY, respectively. 66
- Figure A.6. Waveforms for Event 6 (Table 3.2). The event type is unknown. The calibration values are 0.012781 and 0.012929 nanometers per digital count for stations KKL and BAY, respectively. 67
- Figure A.7. Waveform for Event 7 (Table 3.2). This is probably an earthquake but was not reported in the PDE Bulletin. The calibration value is 0.012929 nanometers per digital count for station BAY. 68

- Figure A.8. Waveform for Event 8 (Table 3.2). The event type is unknown. The calibration value is 0.006406 nanometers per digital count for station KKL. 69
- Figure A.9. Waveforms for Event 9 (Table 3.2). This is an m_b 4.4 earthquake reported in the PDE Bulletin. Note the exceptionally strong S_n at KKL and BAY. The calibration value is 0.006406 nanometers per digital count for all three stations. 70
- Figure A.10. Waveforms for Event 10 (Table 3.2). This is probably an earthquake but was not reported in the PDE Bulletin. The magnitude of this event is approximately 3.3. The data recorded at Bayanaul are plotted in two panels because there is a data gap near 20 s. Note the strong S_n phase at both stations. The calibration value is 0.006406 nanometers per digital count for both stations. 71
- Figure A.11. Waveforms for Event 11 (Table 3.2). This is probably an explosion. The L_g magnitude is approximately 2.6. Note the small L_g/P_n ratio for this event. The calibration value is 0.006406 nanometers per digital count for both stations. 72
- Figure A.12. Waveform for Event 12 (Table 3.2). The event type is unknown. The calibration value is 0.006406 nanometers per digital count for KSU. 73
- Figure A.13. Waveforms for Event 13 (Table 3.2). This is an explosion in the Lake Balkash area [Thurber *et al.*, 1989]. Note the presence of a strong R_g phase at stations KSU and BAY. The L_g magnitude of this event is approximately 2.5. The calibration value is 0.006406 nanometers per digital count at all three stations. 74
- Figure A.14. Waveforms for Event 14 (Table 3.2). This is probably an explosion. The L_g magnitude of this event is approximately 2.3. The calibration value is 0.006406 nanometers per digital count at both stations. 75
- Figure A.15. Waveforms for Event 15 (Table 3.2). The event type is unknown. The calibration values are 1.638321 and 0.006406 nanometers per digital count for stations KSU and KKL, respectively. 76
- Figure A.16. Waveform for Event 16 (Table 3.2). The event is probably an explosion. The L_g magnitude for this event is approximately 2.6. The calibration value is 0.006406 nanometers per digital count for station KSU. 77
- Figure A.17. Waveforms for Event 17 (Table 3.2). This event is an earthquake in the Tien Shan area [Thurber *et al.*, 1989]. The calibration 78

value is 0.006406 nanometers per digital count for all three stations.

Figure A.18. Waveforms for Event 18 (Table 3.2). This event is probably an explosion. The L_g magnitude is approximately 2.5. The calibration value is 0.006406 nanometers per digital count for both stations. 79

Figure A.19. Waveforms for Event 19 (Table 3.2). This event is a 10-ton calibration explosion [Thurber *et al.*, 1989; Given *et al.*, 1989]. The vertical scale is adjusted for the waveform at KSU (the data at BAY and KKL are not clipped). The L_g magnitude for this event is approximately 2.9. The calibration value for station KSU is 0.006406 nanometers per digital count and it is 1.638321 for stations BAY and KKL. 80

Figure A.20. Waveforms for Event 20 (Table 3.2). This event is a 10-ton calibration explosion [Thurber *et al.*, 1989; Given *et al.*, 1989]. The vertical scale is adjusted for the waveform at KSU (the data at BAY and KKL are not clipped). The L_g magnitude for this event is approximately 2.9. The calibration values are 0.050629, 0.102188, and 1.638321 nanometers per digital count for stations BAY, KKL and KSU, respectively. 81

Figure A.21. Waveforms for Event 21 (Table 3.2). This event is an explosion in the Lake Balkash area (compare to Event 13). Note the strong R_g phase. The L_g magnitude for this event is approximately 2.9. The calibration value is 0.012929 nanometers per digital count for station BAY. 82

Figure B.1. Spectra for Event 1 (Table 3.2). See text for explanation. 87

Figure B.2. Spectra for Event 2 (Table 3.2). See text for explanation. 88

Figure B.3. Spectra for Event 3 (Table 3.2). See text for explanation. 89

Figure B.4. Spectra for Event 4 (Table 3.2). See text for explanation. 90

Figure B.5. Spectra for Event 5 (Table 3.2). See text for explanation. 91

Figure B.6. Spectra for Event 6 (Table 3.2). See text for explanation. 92

Figure B.7. Spectra for Event 7 (Table 3.2). See text for explanation. 93

Figure B.8. Spectra for Event 8 (Table 3.2). See text for explanation. 94

Figure B.9. Spectra for Event 9 (Table 3.2). See text for explanation. 95

Figure B.10. Spectra for Event 10 (Table 3.2). See text for explanation. 96

Figure B.11. Spectra for Event 11 (Table 3.2). See text for explanation.	97
Figure B.12. Spectra for Event 12 (Table 3.2). See text for explanation.	98
Figure B.13. Spectra for Event 13 (Table 3.2). See text for explanation.	99
Figure B.14. Spectra for Event 14 (Table 3.2). See text for explanation.	100
Figure B.15. Spectra for Event 15 (Table 3.2). See text for explanation.	101
Figure B.16. Spectra for Event 16 (Table 3.2). See text for explanation.	102
Figure B.17. Spectra for Event 17 (Table 3.2). See text for explanation.	103
Figure B.18. Spectra for Event 18 (Table 3.2). See text for explanation.	104
Figure B.19. Spectra for Event 19 (Table 3.2). See text for explanation.	105
Figure B.20. Spectra for Event 20 (Table 3.2). See text for explanation.	106
Figure B.21. Spectra for Event 21 (Table 3.2). See text for explanation.	107

LIST OF TABLES

	Page
Table 2.1. Elastic upper mantle models.	7
Table 2.2. (a) Q estimates and the exponent of a power law geometric spreading function determined using spectral ratios for synthetic Pn phases computed for Model 1 (layer over a halfspace). The Q estimates are in the upper right diagonal and the spreading exponents are in the lower left diagonal. Entries are given for each pair of epicentral distances. For example, the Q estimated from the spectral ratio between 500 and 900 km is 17156 and the spreading exponent is -2.23. (b) Q values and exponents of a power law geometric spreading function determined analytically for a head wave propagating in a medium with $Q = 50000$ (compare to Table 2.2a).	23
Table 2.3. (a) Q estimates and the exponent of a power law geometric spreading function determined using spectral ratios for synthetic Pn phases computed for Model 2. Entries are in the same format as those in Table 2.2a. (b) Q estimates and the exponent of a power law geometric spreading function determined using spectral ratios for synthetic Pn phases computed for Model 4. Entries are in the same format as those in Table 2.2a.	24
Table 3.1. NRDC station location.	28
Table 3.2. Event parameters.	29
Table 3.3. Moment versus magnitude relations.	40
Table 3.4. Pn attenuation and source parameters.	50
Table B.1. Pn inversion results ($Q(f) = 1175$).	84
Table B.2. Pn inversion results ($Q(f) = 300f^{0.5}$).	85
Table B.3. Lg inversion results ($Q(f) = 650$).	86

(THIS PAGE INTENTIONALLY LEFT BLANK)

1. INTRODUCTION

1.1 Project Objectives

The objective of this two-year study is to simulate detection and location capability of seismic networks including regional stations and arrays in and around the Soviet Union. Three specific research tasks are:

- (1) Enhance and validate the extended version of the Seismic Network Assessment Program for Detection [*SNAP/D*, Ciervo *et al.*, 1985] called *SNAP/DX* [Bratt *et al.*, 1987] to more accurately represent the treaty monitoring capability of seismic networks including regional stations and arrays.
- (2) Normalize *SNAP/DX* to the observed performance of existing stations and expected conditions in and around the Soviet Union.
- (3) Apply the normalized simulation methods to assess the treaty monitoring capability of existing and proposed networks.

1.2 Current Status

Nearly half of the research effort during the first six months of this contract was directed toward the first task (*SNAP/DX* enhancement). This includes incorporating the ability to simulate detection capability normalized by frequency dependent amplitude-distance curves, source functions, and station noise. However, since formal test and evaluation of the new simulation program has not been completed, I will defer its description until the first annual report. The remainder of the research effort during this period was applied to the normalization task.

The key to meaningful simulations of detection and location capability is accurate normalization to the observed performance of existing stations and arrays. This normalization includes the determination of frequency dependent amplitude-distance curves for regional seismic phases, noise spectra appropriate for primary and secondary phases, source spectra and scaling relations, and beam gain for array stations. Two separate databases of regional seismograms and spectra are being assembled as part of this normalization effort. These are:

- **NORESS/ARCESS.** Data recorded by the NORESS and ARCESS arrays in Scandinavia from regional events with M_L between 2.0 and 4.0 will be used as the primary basis for the normalization. NORESS and ARCESS are prototype arrays for regional treaty monitoring and are within regional distances to parts of the western USSR. Also, many of the events are small chemical explosions located in Scandinavia and in the western USSR. Therefore, these data provide a reasonable basis for normalizing the detection capability of a network of stations and arrays in and around the Soviet Union.

- **NRDC.** Data collected by three stations in Eastern Kazakhstan, USSR, as part of a joint project between the Natural Resources Defense Council (NRDC) and the Academy of Sciences of the Union of Soviet Socialist Republics are used to compare regional wave propagation characteristics and noise spectra at one site in the USSR with those in Scandinavia. The attenuation models used to normalize our simulations are derived primarily from data recorded at NORESS and ARCESS. The NRDC data provide an excellent opportunity to test the validity of extrapolating these models to wave propagation in the Soviet Union.

We have processed data from over forty regional events recorded by the NORESS and ARCESS arrays and have acquired waveform data from an additional sixty events. The processing involves interactive picking of regional phases, phase velocity and azimuth determination, amplitude, dominant frequency, and the calculation of Fourier signal and noise spectra. These data will supplement the database of nearly 200 events recorded at NORESS used by *Sereno et al.* [1988] to derive frequency dependent amplitude-distance curves for P_n and L_g . Using data from multiple stations should help resolve the trade-offs among source and path parameters described by *Sereno et al.* [1988].

Data from 21 regional events recorded by one or more of the NRDC stations have been processed. The P_n and L_g spectra are inverted for source and attenuation parameters and the results are compared to models derived previously using NORESS data [*Sereno et al.*, 1988]. Although the amount of NRDC data is insufficient to resolve parameter trade-offs with much certainty, the spectra are consistent with the attenuation models derived for Scandinavia. The NRDC data and the results of this analysis are presented in a section of this report.

As is the case for many attenuation estimation methods, the generalized inverse technique used by *Sereno et al.* [1988] to parameterize the distance dependence of regional wave spectra requires the assumption of the geometric spreading function. This assumption for L_g is based on an interpretation as a sum of higher-mode surface waves and has been carefully studied using synthetic seismogram techniques [*Herrmann and Kijko*; 1983] and by comparing moments derived from surface waves to long-period L_g amplitudes [*Street et al.*, 1975]. However, much less work has been done on the geometric spreading of P_n . Spectral ratio methods assume that P_n spreading is independent of frequency. Other methods assume a power-law range dependence. In this report I investigate the sensitivity of P_n geometric spreading to the velocity gradient in the upper mantle. Particular emphasis is placed on the frequency dependence of P_n geometric spreading and implications for Q estimation methods that assume frequency-independent spreading.

1.3 Outline of the Report

This report is divided to two major sections. The first section reports on (1) the sensitivity of P_n geometric spreading to the velocity gradient in the upper mantle determined using synthetic seismogram techniques and (2) the relationship between

apparent $P_n Q$ determined using spectral ratios and upper mantle anelasticity. The second section reports on regional data recorded in eastern Kazakhstan as part of the NRDC experiment. The attenuation of Lg and P_n are parameterized using generalized inverse techniques and the results are compared to our earlier results for data recorded at NORESS [Serenio *et al.*, 1988].

(THIS PAGE INTENTIONALLY LEFT BLANK)

2. NUMERICAL MODELING OF P_n GEOMETRIC SPREADING

2.1 Introduction

The attenuation of regional P_n phases has important implications for the velocity and anelastic structure of the upper mantle and for many practical issues in nuclear explosion monitoring such as event detection and identification. Yet, very few studies of regional P_n attenuation have been conducted. While it has long been recognized that the attenuation of P_n is a strong function of the velocity gradient in the upper mantle [e.g., Hill, 1972], there have been no quantitative descriptions of the sensitivity of P_n attenuation to upper mantle elastic and anelastic structure for distances between 200 and 1000 km and frequencies between 1 and 15 Hz (ranges relevant for regional nuclear explosion monitoring). The objectives of this study are to (1) determine the sensitivity of P_n geometric spreading (between 200 and 1000 km and 1 to 15 Hz) to the compressional-wave velocity gradient in the upper mantle and (2) determine the relationship between upper mantle anelasticity and apparent P_n Q estimates that are based on the assumption of frequency-independent geometric spreading.

2.2 Approach

Synthetic seismograms are computed for three elastic models with different velocity gradients in the upper mantle. The synthetic seismograms are computed using wavenumber integration [Apsel, 1979]. Synthetic P_n amplitude spectra for these different models are compared as a function of distance to determine the sensitivity of P_n geometric spreading to the velocity gradient in the upper mantle.

To determine the relationship between upper mantle anelasticity and apparent P_n Q estimates, synthetic P_n phases are computed for an anelastic model of the crust and upper mantle. The P_n attenuation for this model is compared to the P_n attenuation for the elastic model with the same velocity structure. Apparent P_n Q is estimated from the synthetics using a spectral ratio method and is compared to the known Q structure of the model.

2.3 Results for Elastic Earth Models

This section reports the results of the synthetic seismogram calculations for three elastic models of the crust and upper mantle in Scandinavia. The elastic models are approximated by setting the quality factor for shear waves and compressional waves equal to 50000 in the crust and upper mantle.

2.3.1 Crustal and Upper Mantle Velocity Models

The crust is approximated by a homogeneous 40-km-thick layer with compressional-wave velocity equal to 6.5 km/s, shear-wave velocity equal to 3.75 km/s, and density equal to 2700 kg/m³. The three models for the upper mantle velocity are listed in

Table 2.1 and compared in Figure 2.1. The velocity at the top of the mantle (α_{MOHO}) is 8.1 km/s for all three models.

Model 1 is a simple crustal layer over a mantle halfspace. This model is included to verify the accuracy of the numerical method since the attenuation for this model can be calculated analytically. Models 2 and 3 approximate upper mantle gradients of 0.0013 s^{-1} and 0.0020 s^{-1} , respectively. The gradient for Model 2 is approximately equal to the earth-flattening transformation of a homogeneous upper mantle (the solid curve in Figure 2.1). The gradient for Model 3 is slightly greater than the gradient in the upper 60 km of the mantle reported by *King and Calcagnile* [1976] for Fennoscandia and western Russia (0.0017 s^{-1}). Mantle density (ρ) is calculated from the compressional-wave velocity (α) using the relation, $\rho = 379 \alpha + 252$.

The wavenumber integration method requires that the earth model consist of a stack of homogeneous layers. Listed in Table 2.1 are the number of layers used to approximate the linear velocity gradient, the thickness of the mantle layers, and the total thickness of the mantle gradient zone. At larger depths the model is a halfspace with velocity equal to the velocity at the base of the gradient. The layer thickness required to approximate a linear velocity gradient depends on the wavelength at the ray turning point [e.g., *Burdick and Orcutt*, 1979; *Chapman and Orcutt*, 1985]. All three models use a mantle layer thickness of 0.8 km which is approximately 1.5 times the P_n wavelength at 15 Hz (the maximum frequency used in the calculation). The total thickness of the gradient zone was selected so that the pre-critical reflection from the bottom of the stack did not interfere with the primary turning ray at the largest epicentral distance (e.g., to avoid model truncation phases). That is, the gradient extends to great enough depth so that the synthetic seismograms at distances less than or equal to 1000 km are independent of the structure below the gradient.

Synthetic displacement spectra for an explosion source were computed between 0 and 20 Hz for distances between 200 and 1000 km. Both source and receiver were located at the free surface. The response was calculated over a phase velocity interval appropriate for P_n (8.0 km/s to 20.0 km/s). A cosine-squared taper was applied between 15 and 20 Hz to the synthetic spectra prior to transforming to the time domain. The explosion source time history is represented by a pressure step function and the source moment was set to 4.0×10^{13} nt-m.

2.3.2 Broadband P_n Amplitude

Figure 2.2 plots temporal P_n displacement amplitude as a function of distance for each of the three elastic models. The amplitude variation of a canonical head wave with distance is $r^{-1/2} l_h^{-3/2}$ where r is epicentral distance and l_h is the length of the head wave segment [e.g., *Aki and Richards*, 1980]. The agreement between this analytic expression (the solid curve in Figure 2.2) and the synthetic P_n amplitudes computed for Model 1 (squares in Figure 2.2) gives confidence in the accuracy of the numerical method.

Table 2.1 Elastic Upper Mantle Models

Model Number	α_{Moho} (km/s)	Velocity Gradient (s^{-1})	Number of Layers	Layer Thickness (km)	Total Thickness (km)
1	8.1	0.0000	1	∞	∞
2	8.1	0.0013	76	0.800	60.0
3	8.1	0.0020	76	0.800	60.0

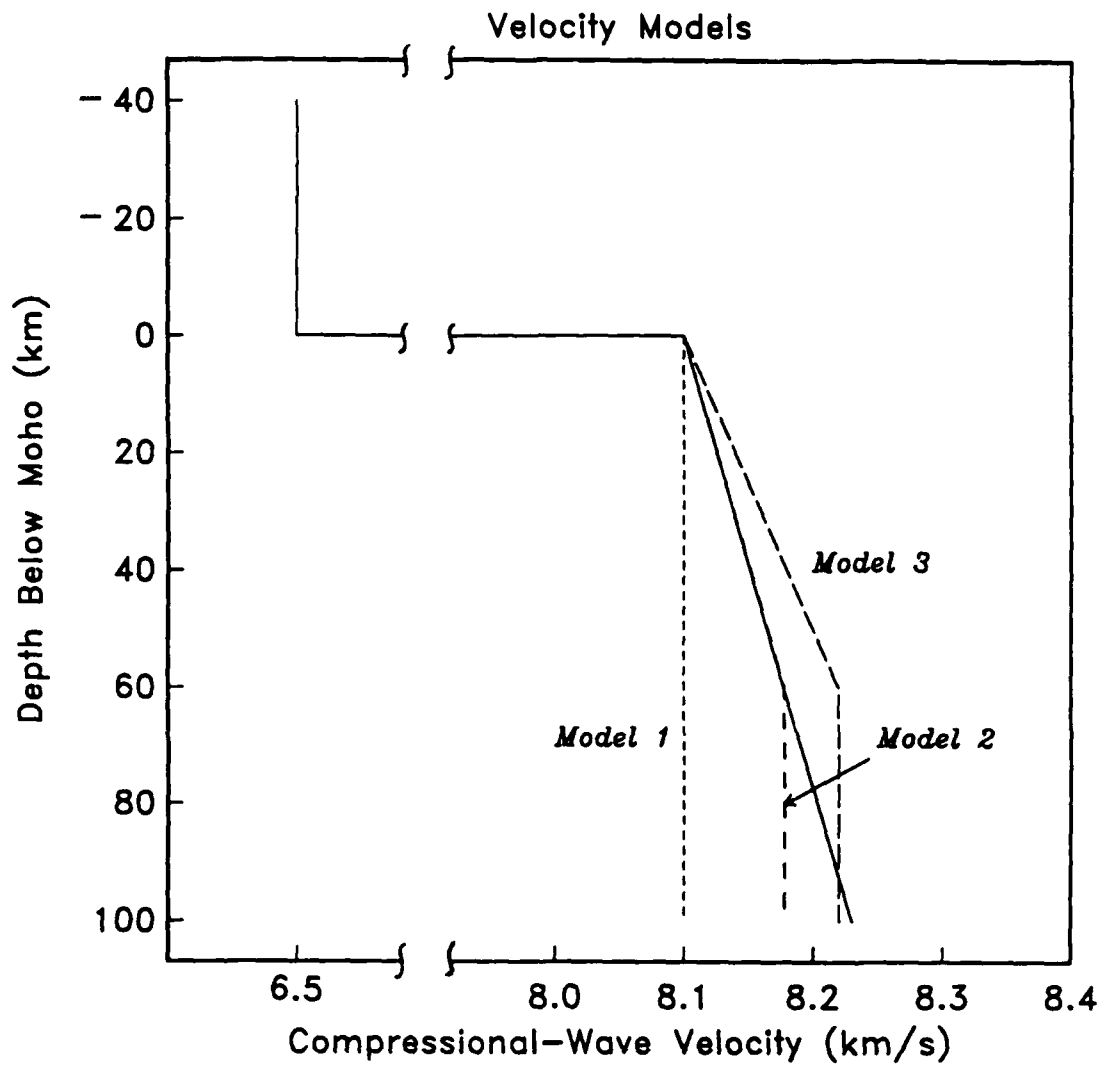


Figure 2.1. Velocity models used in the synthetic seismogram calculations. The solid curve is the earth-flattening transformation for a homogeneous upper mantle. Note the break in the velocity axis.

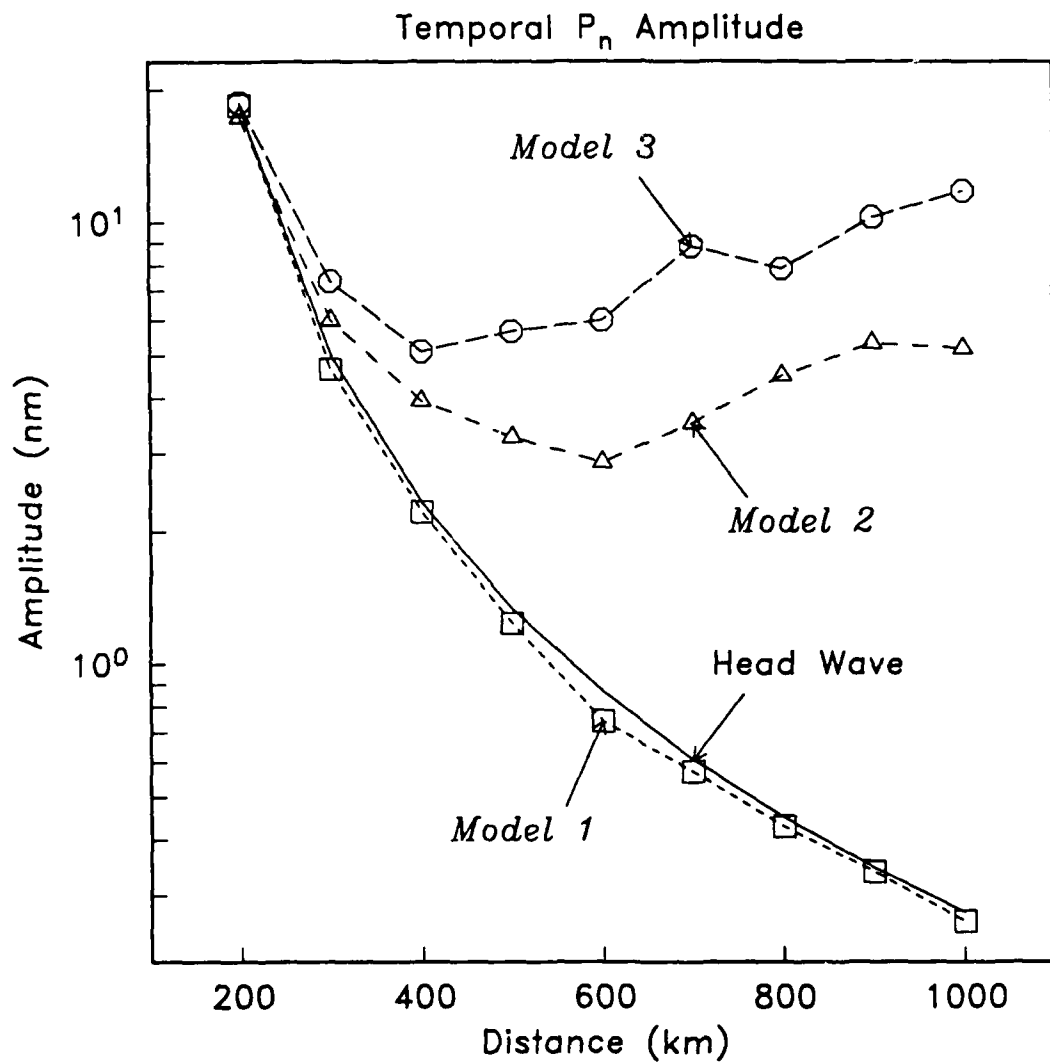


Figure 2.2. Temporal P_n displacement amplitude (1–15 Hz) as a function of epicentral distance for the three elastic earth models. The solid curve is the analytic attenuation of a canonical head wave scaled to the calculated amplitude for Model 1 at 200 km.

All three models produce similar P_n attenuation between 200 and 300 km (the cross-over distance for these models is approximately 110 km). However, the head wave amplitude at 1000 km is close to a factor of 20 smaller than the turning wave amplitude for Model 2 and almost a factor of 45 smaller than turning wave amplitude for Model 3. Note also that P_n amplitude increases between 600 and 1000 km for both linear gradient models. These results are similar to those of Hill [1972], although his calculations were restricted to distances less than 400 km and were for a thinner crustal model. It is clear from Figure 2.2 that the P_n amplitude is extremely sensitive to the velocity gradient in the upper mantle.

2.3.3 Frequency Dependence of P_n Geometric Spreading

The P_n waveforms computed for the linear gradient models are similar to the head wave at short ranges (within a few hundred kilometers of the critical distance) but evolve into a turning wave with increasing distance. The distance over which this transition occurs depends on the crustal thickness and the velocity gradient in the mantle. Since the turning ray has a time dependence that is the derivative of the head wave [e.g., Aki and Richards, 1980], the change in the P_n waveform with distance implies a strong frequency dependence in the geometric spreading for upper mantle models characterized by linear velocity gradients.

For example, Figures 2.3a–2.3c display synthetic P_n particle velocity for the three elastic models described in Section 2.3.1. Velocity is plotted since the head wave produces static displacement. Note that the amplitudes are scaled to be the same on each trace. The synthetic P_n waveforms are delta functions at all ranges for Model 1 (Figure 2.3a). The geometric spreading for this model is independent of frequency. At distances less than about 300 km, the P_n travel paths for the two gradient models are almost identical to the P_n head wave (the turning depth is less than 1.5 km below the Moho). Thus, at these distances the P_n waveforms computed for the gradient models are similar to the P_n head waves computed for Model 1. However, the turning wave dominates for ranges greater than 500–600 km and the P_n waveform has a time dependence that is the derivative of the head wave.

Figure 2.4a - 2.4c are perspective plots of the P_n displacement spectra as a function of epicentral distance for the three elastic models. The spectra are calculated for a 1-s window centered on P_n . These plots combine the observations made from Figures 2.2 and 2.3 into a quantitative description of the frequency and range dependence of P_n geometric spreading. Note that the spectral shape (ω^{-1}) is constant for all ranges for Model 1 and is equal to the source pressure spectrum. The P_n spectra for the two gradient models fall off as ω^{-1} at short ranges, but are nearly flat beyond 500-600 km due to the increasing contribution of the turning ray.

The scalloping in the P_n spectra for Model 3 beyond 700 km (Figure 2.4c) is due to the separation of the primary turning wave and the first whispering gallery phase [Menke and Richards, 1980]. Figure 2.5a is a schematic ray diagram illustrating the ray paths for the primary turning ray (P) and the first whispering gallery phase ($WG1$)

(a) Model 1: Layer over Halfspace

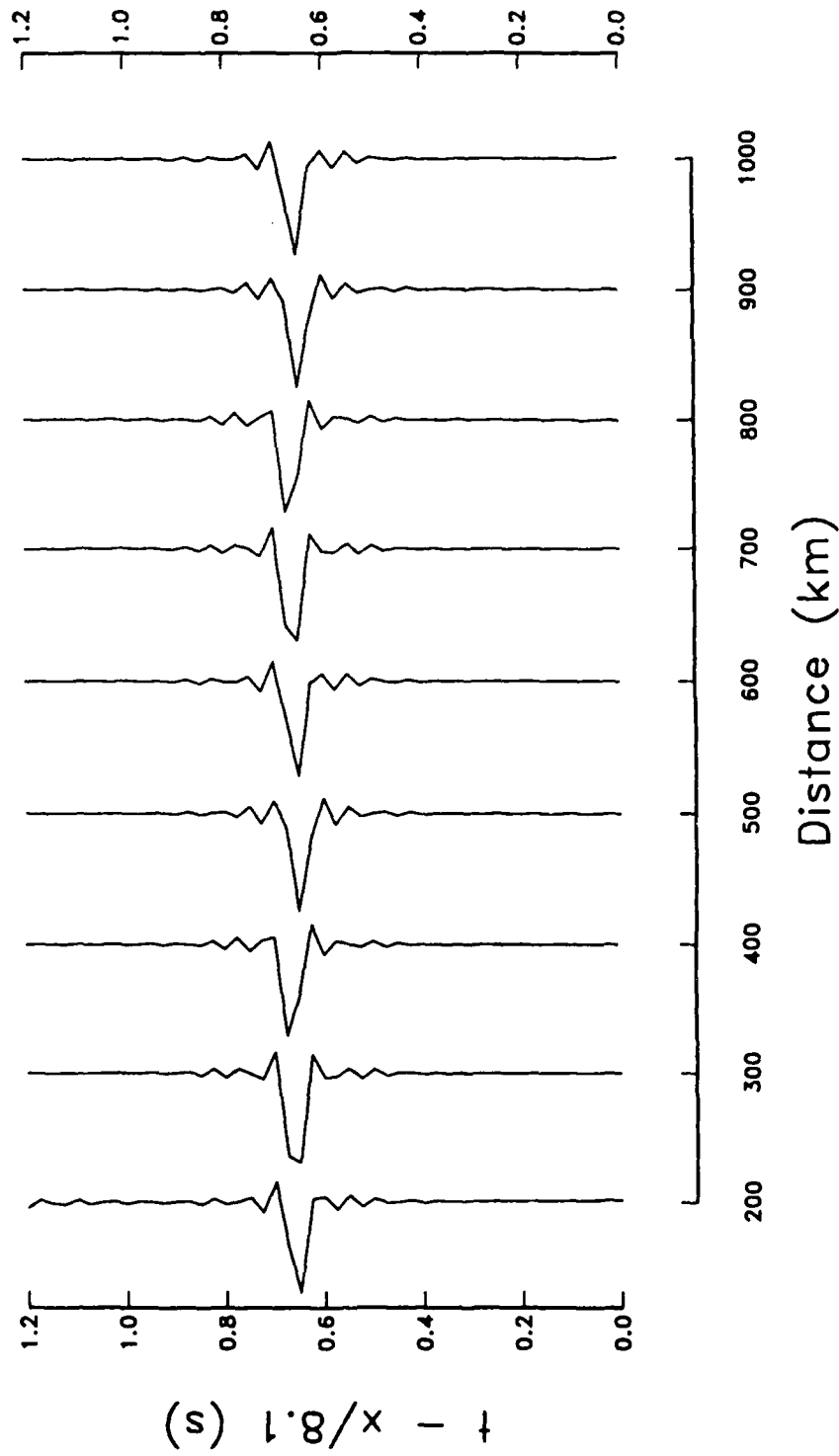


Figure 2.3. Record section plot of P_n particle velocity for (a) Model 1, (b) Model 2 and (c) Model 3. Travel times are reduced at 8.1 km/s. The amplitudes of each trace are scaled independently.

(b) Model 2: $\delta\alpha/\delta z = 0.0013 \text{ s}^{-1}$

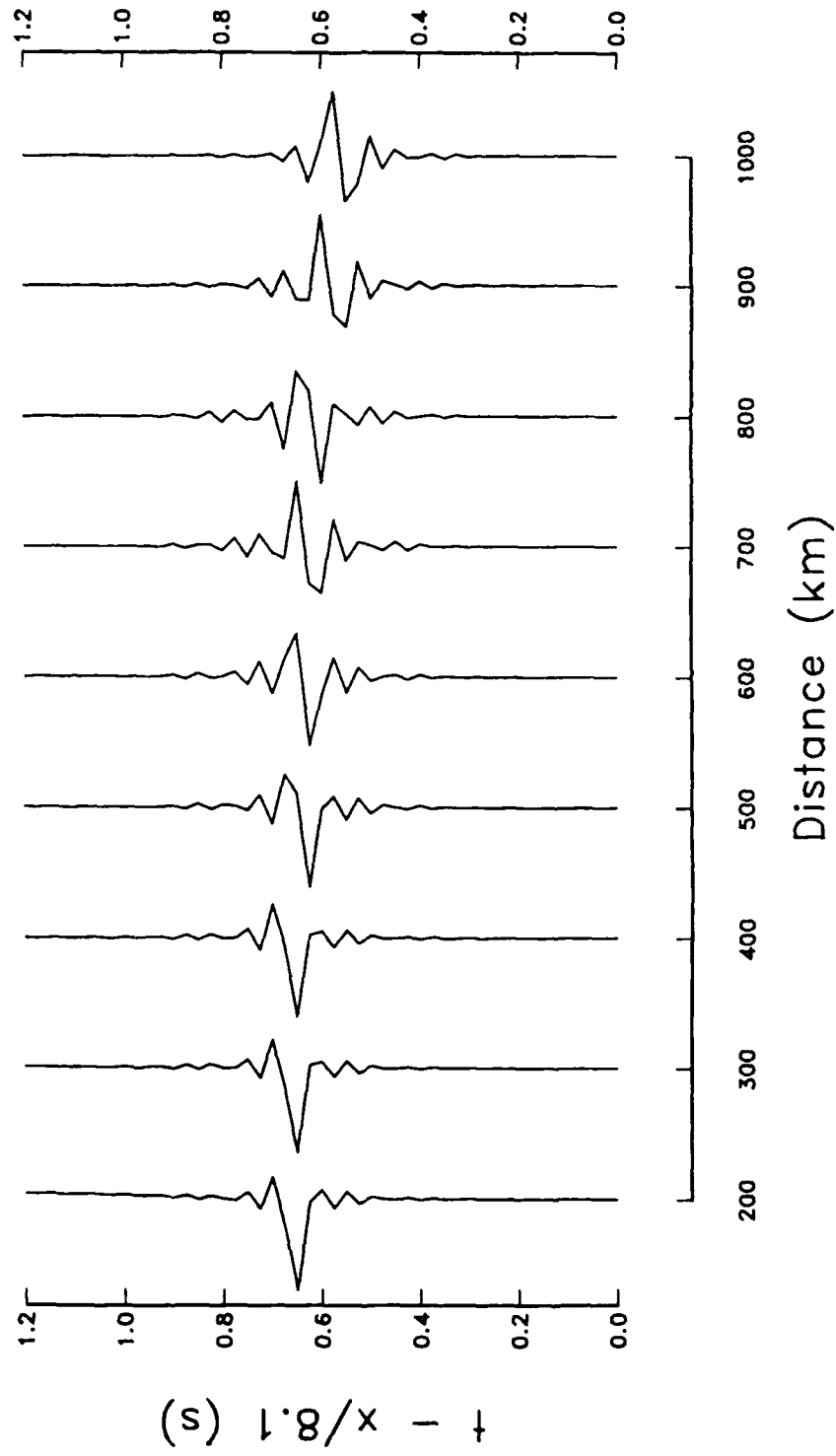


Figure 2.3. Continued.

(c)

Model 3: $\delta\alpha/\delta z = 0.002 \text{ s}^{-1}$

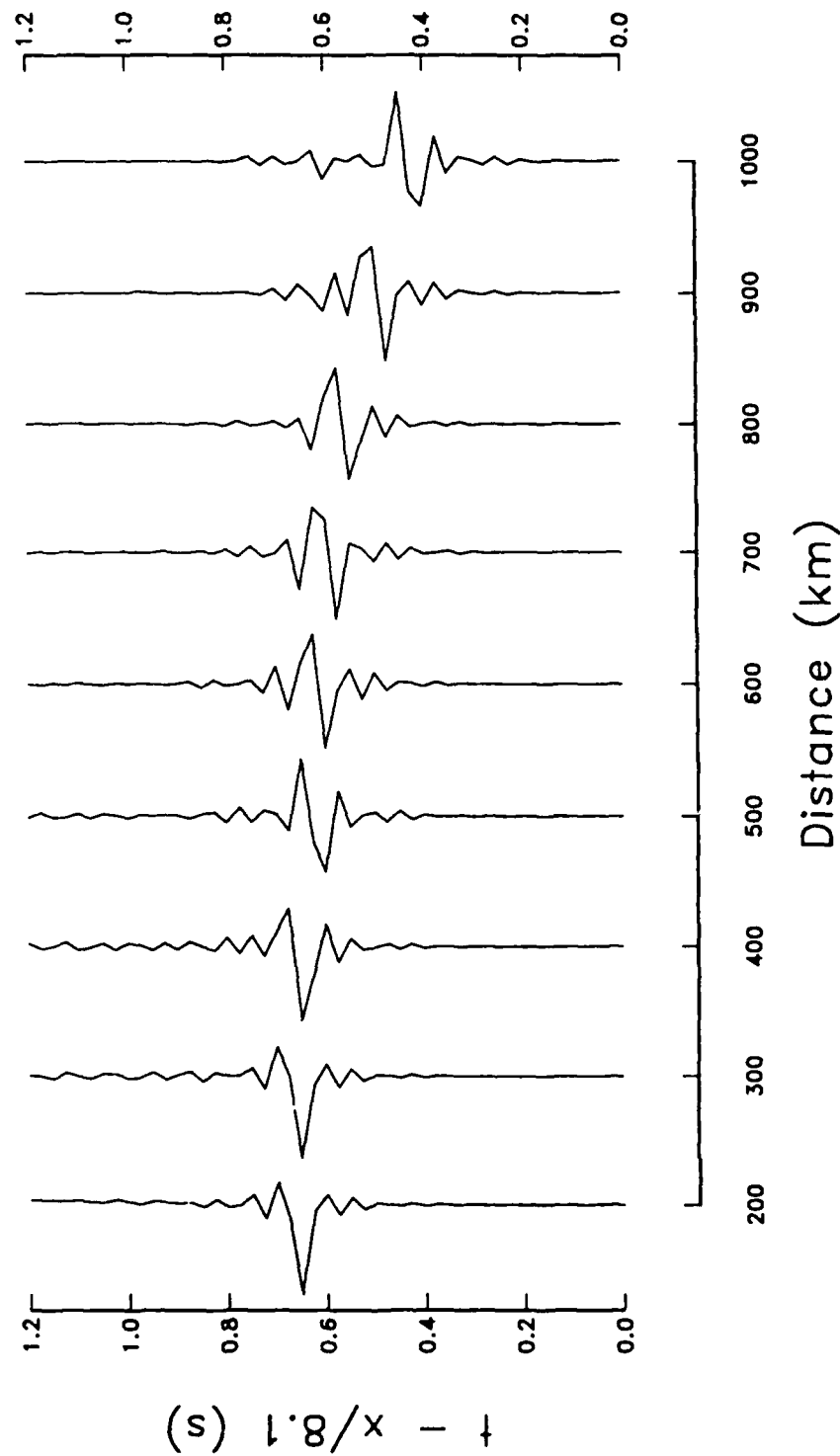


Figure 2.3. Continued.

(a) **P_n Displacement Spectra
Model 1: Layer Over Halfspace**

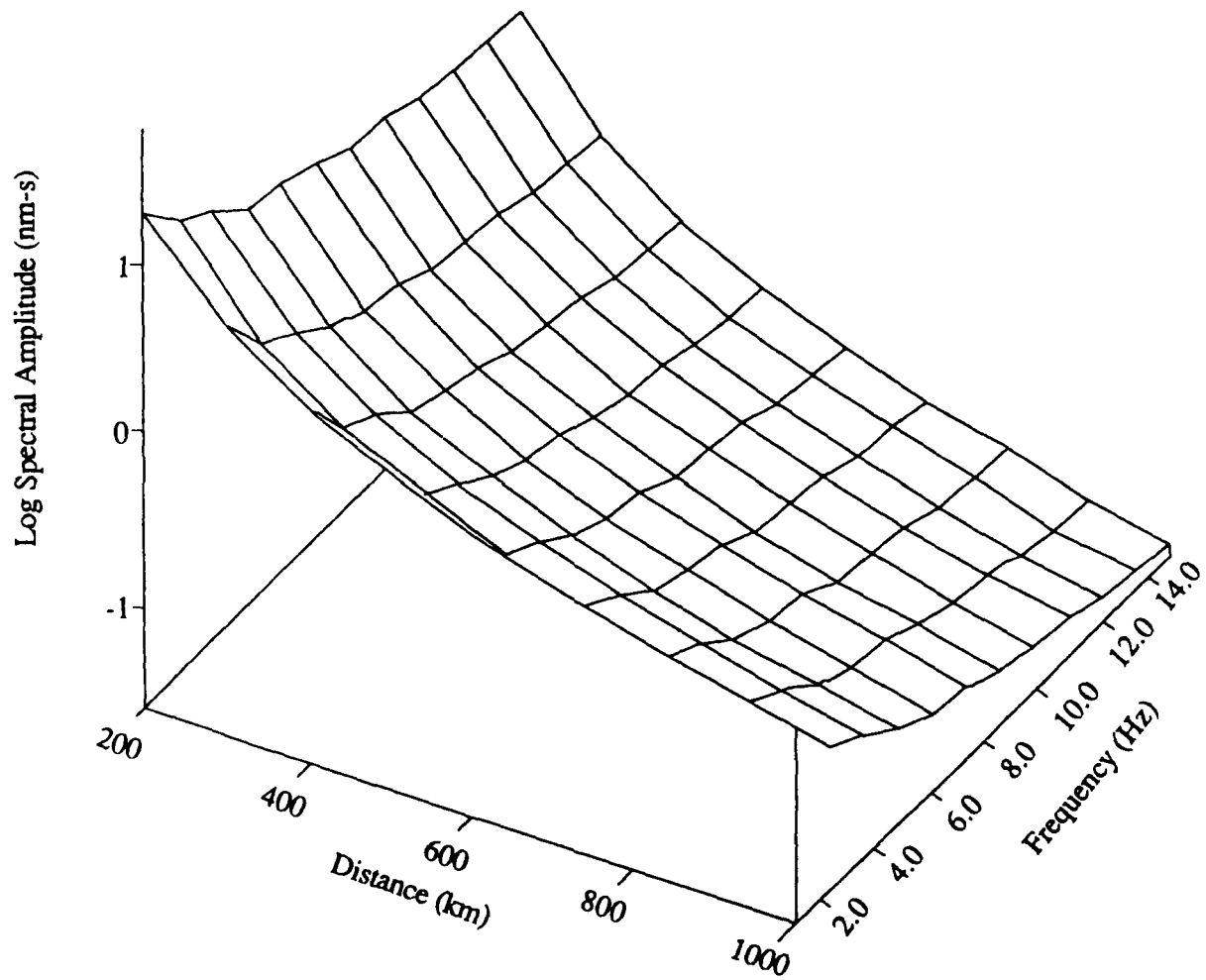


Figure 2.4. Perspective plot of P_n displacement spectra as a function of epicentral distance computed for (a) Model 1, (b) Model 2 and (c) Model 3.

(b) **Pn Displacement Spectra**
Model 2: $\delta\alpha / \delta z = 0.0013 \text{ S}^{-1}$

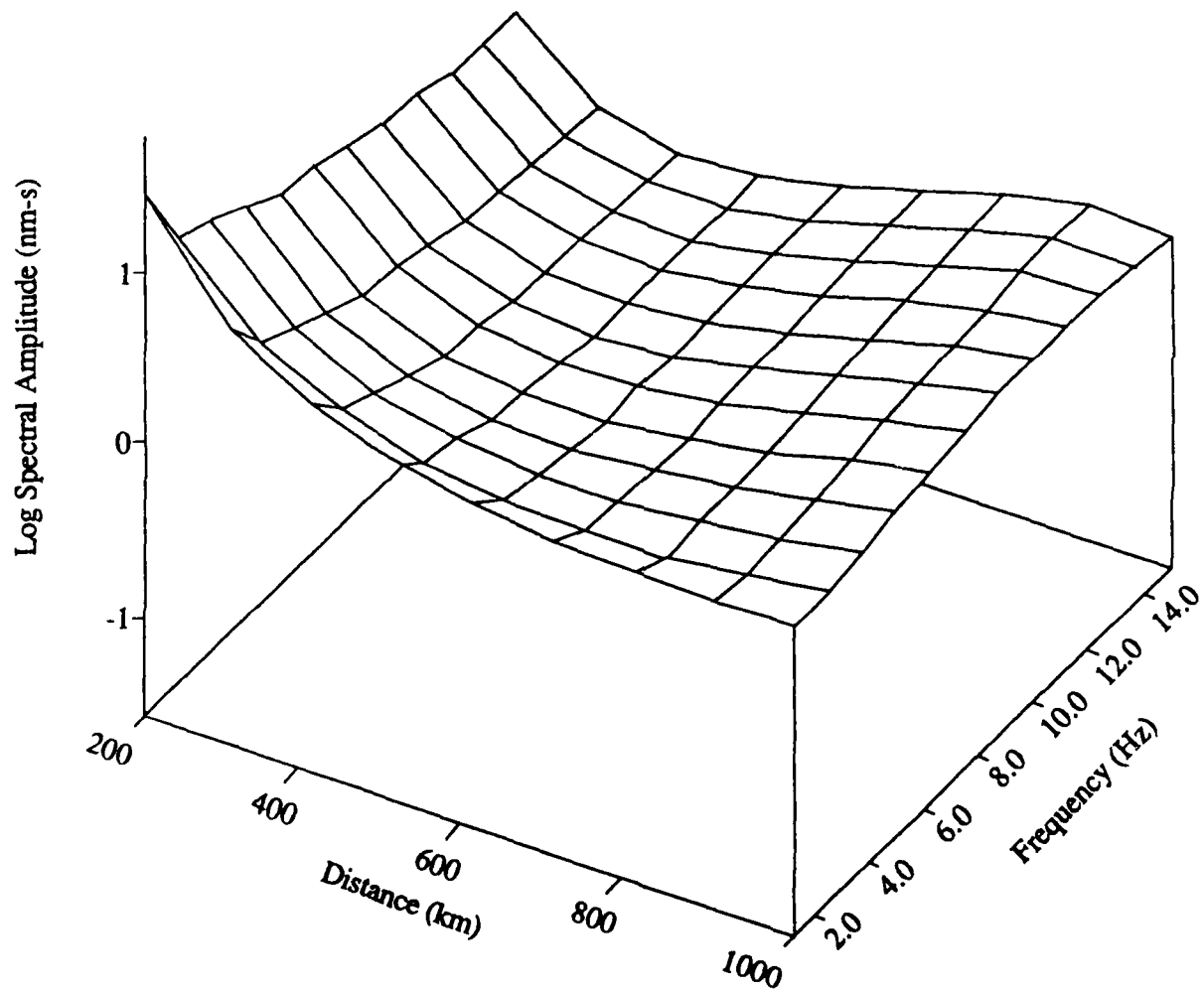


Figure 2.4. Continued.

(c) **Pn Displacement Spectra**
Model 3: $\delta\alpha / \delta z = 0.0020 \text{ S}^{-1}$

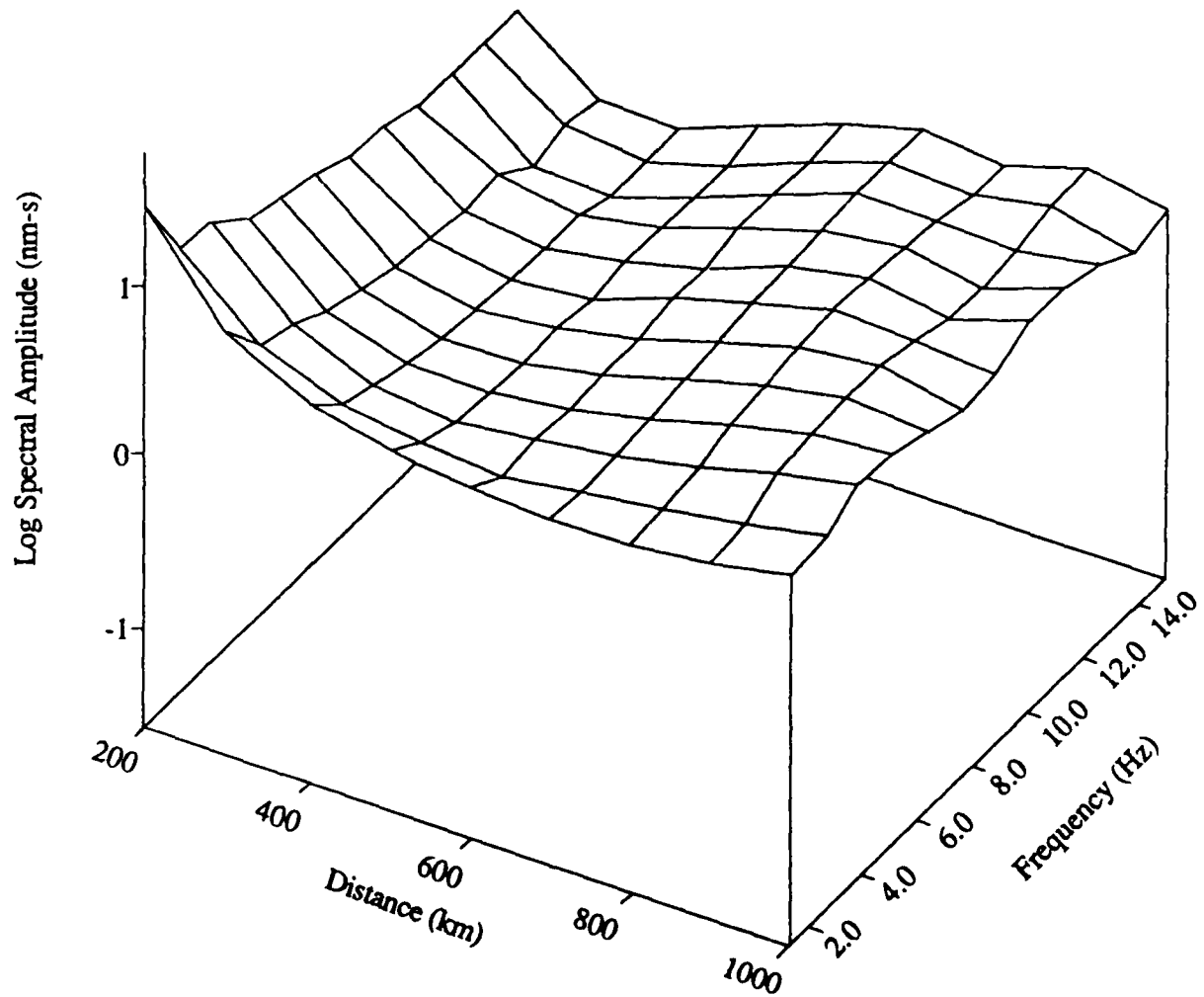
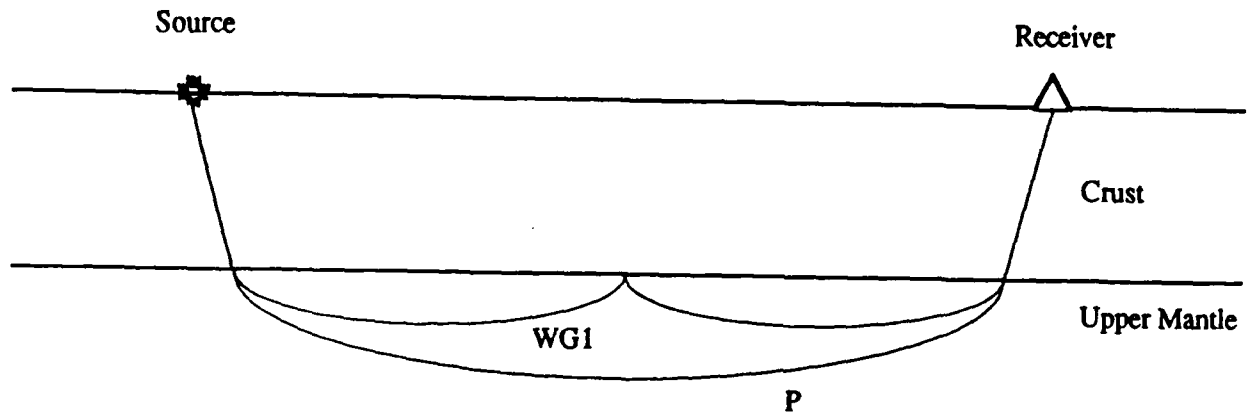


Figure 2.4. Continued.

(a)



(b)

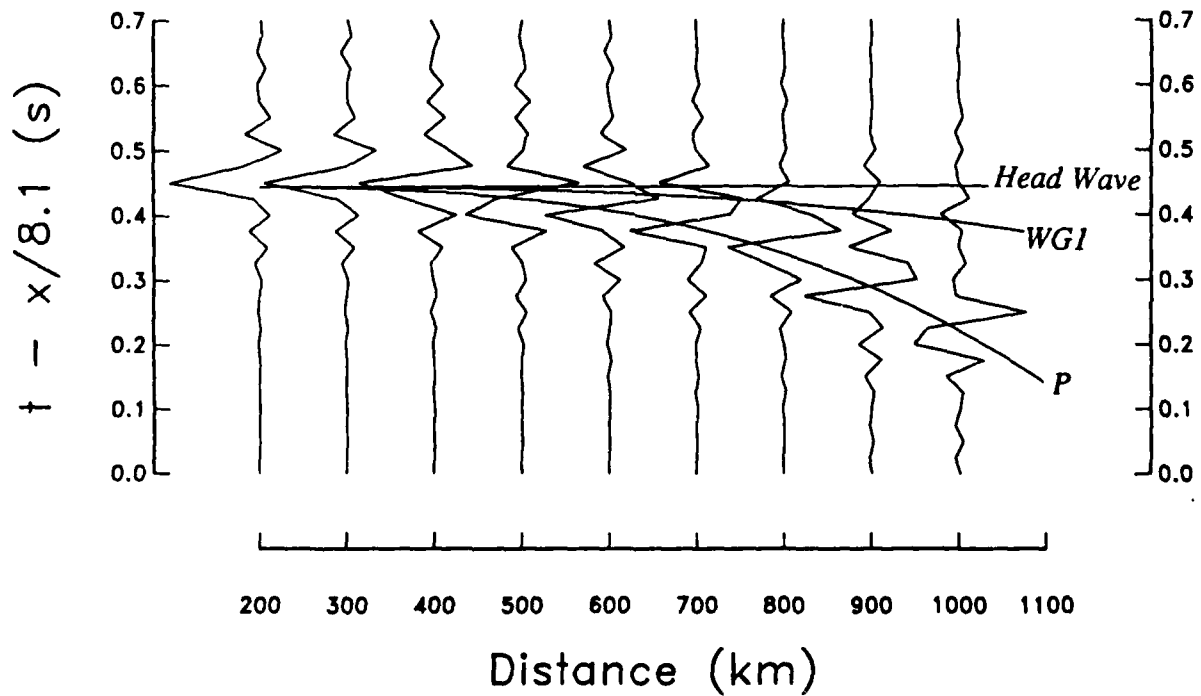


Figure 2.5. (a) Schematic ray diagram for the primary turning ray (*P*) and the first whispering gallery phase (*WG1*). (b) Record section plot of *P_n* particle velocity for Model 3 reduced at 8.1 km/s. Travel-time curves for *P*, *WG1*, and the head wave are superimposed.

which includes an upward reflection at the Moho. Figure 2.5b is the Pn record section for Model 3 with travel-time curves for P , $WG1$, and the head wave superimposed. Note the appearance of $WG1$ beyond about 700 km. At longer ranges the time separation between P and $WG1$ increases and the spectral modulation moves toward lower frequencies.

2.4 Results for an Anelastic Earth Model

This section reports the results of the synthetic seismogram calculations for an anelastic model of the crust and upper mantle. The velocities and densities are the same as Model 2 described in the previous section. The P - and S - wave quality factors were set to 1000 and 500 in the crust, respectively [Kennett, 1985]. The mantle quality factors were set to 2000 and 1000 for compressional and shear waves, respectively. These values are simply used for demonstration purposes and are not necessarily representative of upper mantle anelasticity in Fennoscandia. For notational convenience this will be referred to as Model 4.

Figure 2.6 plots temporal Pn amplitude for Models 2 and 4. The solid curve is the analytic attenuation for a head wave. The Pn attenuation for the anelastic model with a linear gradient (Model 4) is almost identical to the Pn attenuation of a head wave in an elastic medium for distances less than 400 km. Figure 2.7 is a record section of Pn particle velocity and Figure 2.8 is the perspective plot of Pn displacement spectra as a function of distance for Model 4. The obvious effect of including anelastic attenuation is the reduction in the amount of high frequencies (compare Figure 2.7 with Figure 2.3b and Figure 2.8 with Figure 2.4b). The large reduction in high frequencies between 900 and 1000 km is due to scalloping caused by interference with the first whispering gallery phase.

Evernden *et al.* [1986] report that Pn attenuation in the eastern United States can be described by r^{-2} geometric spreading and a constant Q of 9000. Their results are based primarily on amplitudes measured between 1 and 3 Hz. Chun *et al.* [1989] report that the attenuation of Pn waves between 1 and 15 Hz in eastern Canada increases with increasing frequency. Their model is consistent with the Evernden *et al.* [1986] model at low frequency but predicts smaller Pn amplitudes at frequencies greater than a few Hertz. Figure 2.8 shows that the Pn attenuation for Model 4 is only weakly dependent on frequency (except for the modulation due to the interference of the whispering gallery phase). Therefore, the frequency dependence of Pn attenuation described Chun *et al.* [1989] suggests that if the velocity gradient in the upper mantle is greater than zero, then the Q (crustal or upper mantle) in eastern North America is lower than the value used in Model 4.

2.5 Implications for Q Estimation

It is obvious from Figures 2.3b and 2.3c that unless the velocity gradient in the upper 50–100 km of the mantle is negative, the Q estimates that are derived using spectral

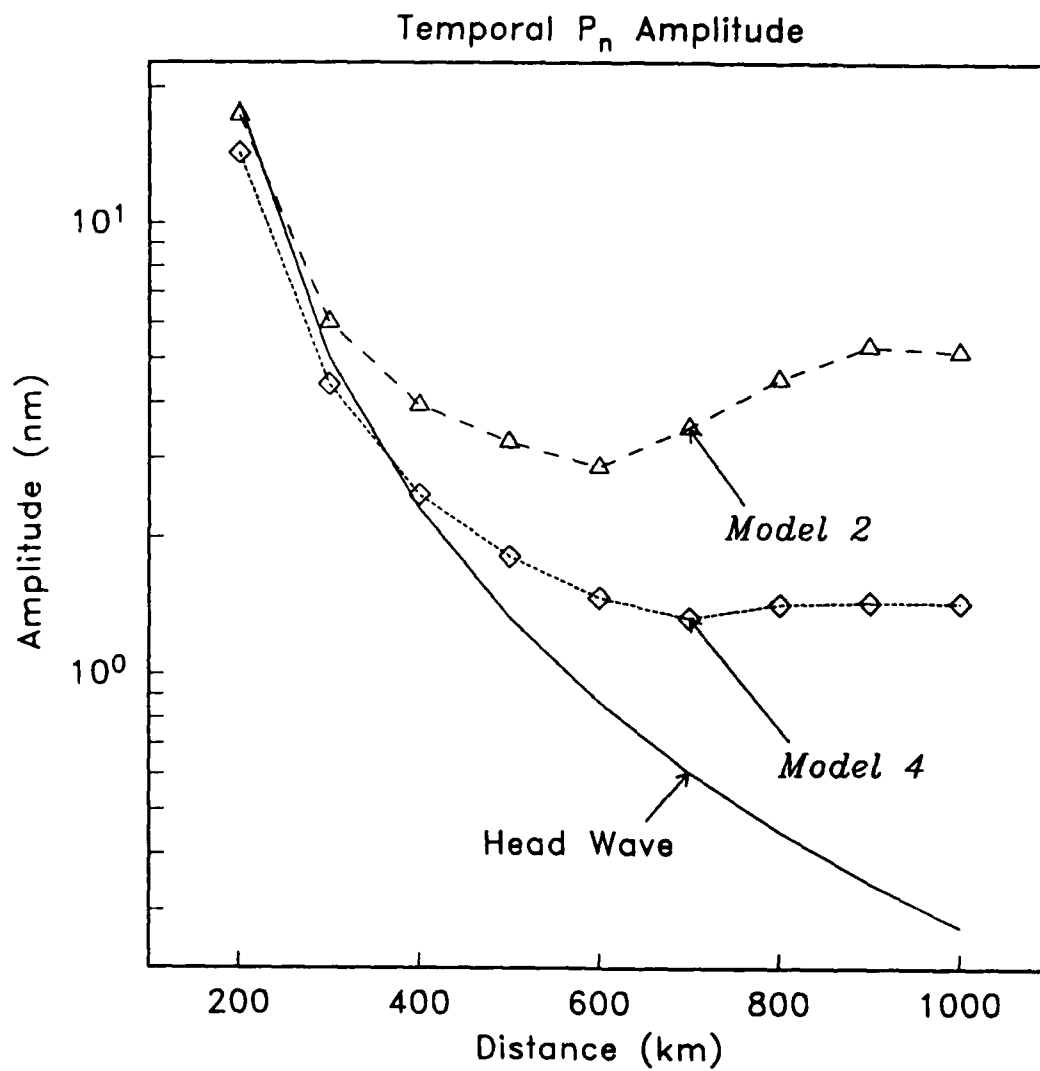


Figure 2.6. Temporal P_n amplitude (1–15 Hz) for Models 2 and 4. The solid curve is the analytic attenuation of a canonical head wave.

Model 4: $\delta\alpha/\delta z = 0.0013 \text{ s}^{-1} (Q)$

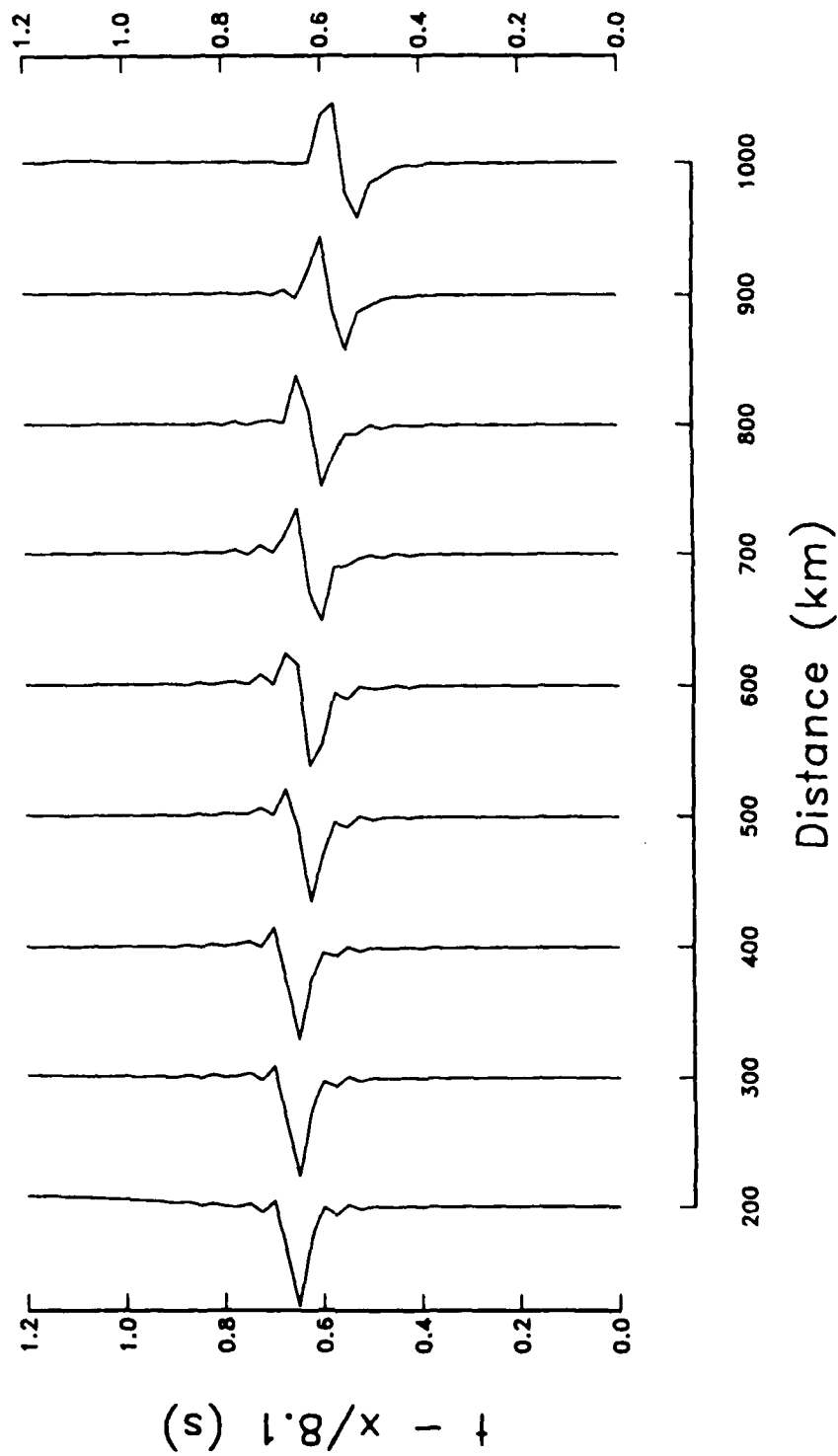


Figure 2.7. Record section plot of P_n particle velocity for Model 4. Travel times are reduced at 8.1 km/s. The amplitudes of each trace are scaled independently.

Pn Displacement Spectra

Model 4: $\delta\alpha / \delta z = 0.0013 \text{ S}^{-1}(\text{Q})$

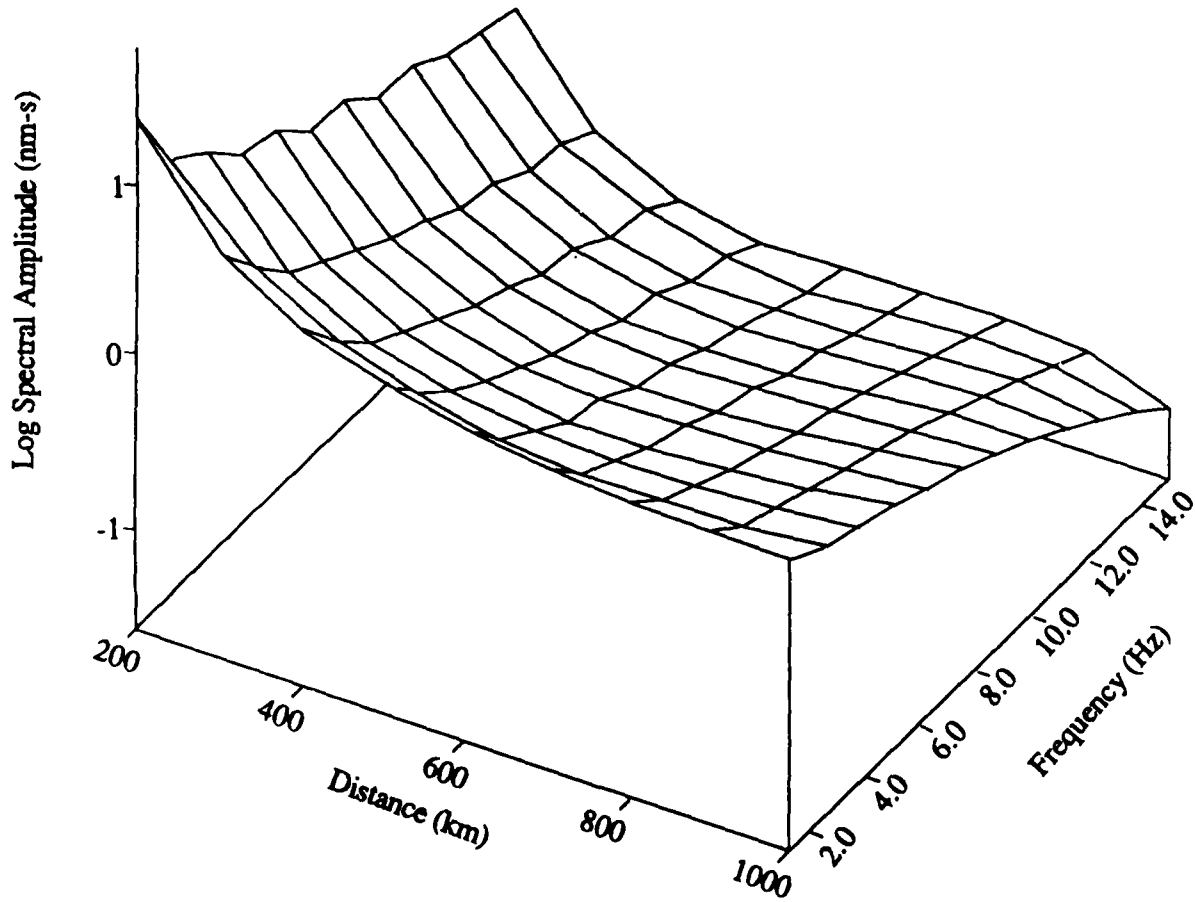


Figure 2.8. Perspective plot of P_n displacement spectra as a function of epicentral distance computed for Model 4.

ratio methods will be biased high. This is because the spectral ratio method assumes that the change in the P_n spectrum with distance is due to anelasticity. However, the differentiation of the P_n waveform several hundred kilometers beyond the critical distance enhances the high frequencies relative to low frequencies. Thus, the apparent Q includes both the geometric effect (which increases the amount of high frequencies) and the anelastic effect (which reduces the amount of high frequencies). The bias in Q is larger for spectral ratios calculated over distances including the transition zone from head wave to turning wave (e.g., 400 to 700 km) than for ratios calculated over a smaller interval outside the transition region (e.g., 800 to 1000 km).

Spectral ratios were computed from the synthetic P_n phases to quantify the Q bias. The logarithm of the ratio of the displacement spectra, $A(f,r)$, at two ranges is expressed as

$$\log \left[\frac{A(f,r_1)}{A(f,r_2)} \right] = \log \left[\frac{G(r_1)}{G(r_2)} \right] - \frac{\pi \log e (t_1 - t_2) f}{Q} \quad (2.1)$$

where $G(r)$ is geometric spreading, t is travel time, and f is frequency. If geometric spreading and Q are assumed to be independent of frequency, then (2.1) is the equation of a straight line with slope proportional to Q^{-1} and intercept equal to the logarithm of the geometric spreading ratio at the two ranges. If we further assume that the geometric spreading has a power law range dependence, r^{-n} , then the intercept of the spectral ratio is given by

$$\log \left[\frac{G(r_1)}{G(r_2)} \right] = -n \log \left[\frac{r_1}{r_2} \right] \quad (2.2)$$

Table 2.2a lists Q values and geometric spreading exponents, $-n$, derived from spectral ratios of the synthetic P_n phases computed for Model 1. Table 2.2b lists the analytic values for these parameters. In this case geometric spreading is independent of frequency and the spectral ratio method accurately recovered the P_n spreading rate and very high Q values. Table 2.3a lists Q values and geometric spreading exponents derived from spectral ratios of the synthetic P_n phases computed for Model 2. Negative Q values are obtained because of the increasing contribution of the turning ray and the differentiation of the P_n waveform. The spreading rates are similar to those of a head wave between 200 and 400 km but increase rapidly at larger distances and become positive between 700 and 1000 km. Table 2.3b lists Q values and geometric spreading exponents for Model 4. In general the estimated Q values are negative. The lower Q values associated with the spectrum at 1000 km are due to the spectral hole at that distance near 15 Hz which is caused by interference with the first whispering gallery phase. Aside from this anomaly, the effect of assuming a frequency-independent P_n geometric spreading function is to greatly overestimate upper mantle Q using the spectral ratio method.

	200	300	400	500	600	700	800	900	1000
200		9217	16052	18231	21250	23518	25299	17601	24660
300	-3.13		62097	35677	37623	38421	38860	20746	32420
400	-2.95	-2.69		25029	31430	34089	35535	18308	30028
500	-2.83	-2.58	-2.45		42231	41624	41317	17156	31278
600	-2.75	-2.52	-2.40	-2.35		41033	40875	14322	29373
700	-2.69	-2.48	-2.38	-2.33	-2.30		40718	10805	26831
800	-2.65	-2.45	-2.35	-2.31	-2.28	-2.26		6229	22923
900	-2.59	-2.39	-2.29	-2.23	-2.17	-2.10	-1.91		-13644
1000	-2.58	-2.40	-2.30	-2.26	-2.22	-2.19	-2.15	-2.41	

Table 2.2a. Q estimates and the exponent of a power law geometric spreading function determined using spectral ratios for synthetic P_n phases computed for Model 1 (layer over a halfspace). The Q estimates are in the upper right diagonal and the spreading exponents are in the lower left diagonal. Entries are given for each pair of epicentral distances. For example, the Q estimated from the spectral ratio between 500 and 900 km is 17156 and the spreading exponent is -2.23.

	200	300	400	500	600	700	800	900	1000
200		50000	50000	50000	50000	50000	50000	50000	50000
300	-3.21		50000	50000	50000	50000	50000	50000	50000
400	-2.99	-2.68		50000	50000	50000	50000	50000	50000
500	-2.87	-2.59	-2.48		50000	50000	50000	50000	50000
600	-2.78	-2.53	-2.43	-2.37		50000	50000	50000	50000
700	-2.72	-2.49	-2.39	-2.34	-2.30		50000	50000	50000
800	-2.68	-2.46	-2.37	-2.31	-2.28	-2.25		50000	50000
900	-2.64	-2.43	-2.34	-2.29	-2.26	-2.24	-2.22		50000
1000	-2.61	-2.41	-2.33	-2.28	-2.25	-2.22	-2.21	-2.19	

Table 2.2b. Q values and exponents of a power law geometric spreading function determined analytically for a head wave propagating in a medium with $Q = 50000$ (compare to Table 2.2a).

	200	300	400	500	600	700	800	900	1000
200		-1605	-1567	-1469	-1399	-1369	-1390	-1502	-1826
300	-3.17		-1531	-1410	-1342	-1320	-1354	-1487	-1863
400	-2.82	-2.32		-1306	-1263	-1262	-1316	-1478	-1932
500	-2.59	-2.13	-1.89		-1223	-1241	-1319	-1528	-2137
600	-2.40	-1.96	-1.70	-1.46		-1260	-1373	-1667	-2628
700	-2.23	-1.78	-1.50	-1.25	-0.99		-1508	-1988	-4117
800	-2.05	-1.59	-1.28	-1.00	-0.70	-0.36		-2915	-30453
900	-1.84	-1.35	-1.01	-0.67	-0.32	0.10	0.62		3606
1000	-1.58	-1.04	-0.64	-0.23	0.20	0.72	1.37	2.21	

Table 2.3a. Q estimates and the exponent of a power law geometric spreading function determined using spectral ratios for synthetic P_n phases computed for Model 2. Entries are in the same format as those in Table 2.2a.

	200	300	400	500	600	700	800	900	1000
200		8603	-80941	-10492	-6181	-5648	-6146	-9675	36524
300	-2.80		-7095	-4973	-3930	-3994	-4577	-7145	68096
400	-2.53	-2.15		-3828	-3213	-3486	-4204	-7155	24616
500	-2.33	-1.95	-1.68		-2768	-3337	-4346	-9142	9902
600	-2.16	-1.78	-1.52	-1.31		-4200	-6076	-39297	4618
700	-1.96	-1.56	-1.25	-0.97	-0.56		-10977	12368	2717
800	-1.75	-1.32	-0.97	-0.64	-0.21	0.20		3956	1673
900	-1.51	-1.03	-0.63	-0.23	0.25	0.75	1.36		1061
1000	-1.19	-0.65	-0.17	0.31	0.89	1.52	2.31	3.37	

Table 2.3b. Q estimates and the exponent of a power law geometric spreading function determined using spectral ratios for synthetic P_n phases computed for Model 4. Entries are in the same format as those in Table 2.2a.

2.6 Discussion

The amplitude of P_n is extremely sensitive to the velocity gradient in the upper mantle. For example, the synthetic P_n amplitude at 1000 km is 20 times greater for a model with a weak upper mantle gradient (0.0013 s^{-1}) than the canonical head wave amplitude for a layer over a halfspace. This gradient corresponds to the earth-flattening transformation of a homogeneous upper mantle. Thus, earth sphericity is sufficient to cause significant departure of P_n attenuation from that of a canonical head wave.

The geometric spreading of a canonical head wave is independent of frequency. The geometric spreading of P_n for a model with increasing velocity with depth is strongly dependent on frequency. The P_n waveform for a model with a weak velocity gradient (like that introduced by sphericity alone) is similar to a head wave at distances within a few hundred kilometers of the critical distance, but has the time dependence of a turning wave at longer ranges. Thus, the P_n waveform at long ranges is the derivative of the P_n waveform near the critical distance. The distance over which the transition occurs depends on the crustal thickness and the upper mantle velocity gradient. For the models considered here, the transition occurs between about 400 and 700 km. *Burdick, et al.* [1988] show that P_n waveforms from explosions at the Nevada Test Site are consistent with a turning ray representation which suggests that there is a positive velocity gradient in the upper mantle in that region.

Many methods for estimating anelastic attenuation assume that geometric spreading is independent of frequency. This can lead to an overestimate of $P_n Q$ if the velocity in the upper 50–100 km of the mantle increases with depth. For example, it is shown in this report that Q cannot be recovered from synthetic P_n phases computed for a very simple model of the upper mantle (a linear gradient) using a spectral ratio method. Therefore, accurate estimates of the velocity gradient of the upper mantle are required before meaningful estimates of upper mantle anelasticity can be made from P_n observations.

(THIS PAGE INTENTIONALLY LEFT BLANK)

3. ATTENUATION OF P_n AND L_g PHASES RECORDED IN EASTERN KAZAKHSTAN

3.1 Introduction

Sereno and Bratt [1989] use attenuation models and ambient noise spectra derived from data recorded by the NORESS array in Norway to estimate the detection capability of a network of seismic arrays in and around the Soviet Union. These estimates have a large uncertainty since it is not known how well NORESS represents stations inside the Soviet Union. Data recently obtained from three stations inside the Soviet Union provide an excellent opportunity to check how well NORESS represents conditions at these sites. The three seismic stations were operated in eastern Kazakhstan, USSR, as part of a joint experiment involving the National Resources Defense Council (NRDC) in the United States and the Academy of Sciences of the Union of Soviet Socialist Republics.

Spectra of P_n and L_g phases from 21 regional events recorded by one or more of these NRDC seismic stations are inverted for source and attenuation parameters using the method of *Sereno et al.* [1988]. The average ambient noise spectrum for the NRDC stations is computed from time windows preceding P_n . This noise spectrum and the parameterization of regional wave attenuation are compared with results determined previously for Scandinavia using NORESS data [*Sereno et al.*, 1988]. This report summarizes the major conclusions from the comparison. The data from the NRDC stations are too few to normalize estimates of the detection threshold in the Soviet Union, but the comparison with our NORESS results allows an assessment of the validity of using NORESS performance to normalize estimates of the detection threshold.

3.2 Event and Station Locations

Three seismic stations were installed in 1987 within 200 km of the principal underground nuclear explosion test site in eastern Kazakhstan [*Berger et al.*, 1988]. Each station is equipped with two 3-component surface seismometers and a 3-component borehole seismometer. The station locations and sensor depths of the borehole seismometers are listed in Table 3.1. *Berger et al.* [1988] give a complete description of the NRDC sites and instrumentation.

The data used in this study consist of P_n and L_g phases recorded by one or more of the three NRDC stations from 21 regional events at distances between 200 and 1300 km. Event magnitudes are approximately 2.3 to 4.6. Table 3.2 lists the location, origin time, and magnitude of each event used in this study. The station locations and event epicenters are plotted on a map in Figure 3.1. Events 1, 2, 3, 5 and 9 are earthquakes listed in the Preliminary Determination of Epicenters (PDE), a bulletin produced by the United States Geological Survey (USGS). The location of Event 9 is from *Thurber et al.* [1989] who used travel times and azimuths determined from data recorded at the three NRDC stations to obtain a location 40 km east of the PDE

Table 3.1 NRDC Station Location

Name	Latitude	Longitude	Elevation (m)	Senor Depth (m) (Borehole Sensor)
Karkaralinsk (KKL)	49.333	75.383	1000	66
Karasu (KSU)	49.950	81.083	420	101
Bayanaul (BAY)	50.817	75.550	600	99

Table 3.2 Event Parameters

Event	Julian Day	Origin Time	Latitude	Longitude	Depth (km)	m_b	Event Type
1	136	18:21:13.7	39.339	73.812	33.0	4.3	EQ
2	120	6:54:57.0	39.733	74.594	10.0	4.3	EQ
3	122	21:38:33.2	39.569	74.541	33.0	4.6	EQ
4	123	8:52:08.0	51.512	89.874			
5	146	13:44:19.9	42.923	78.063	20.0	4.6	EQ
6	164	2:19:13.2	47.300	79.473			
7	162	18:30:04.0	42.842	80.968			EQ
8	232	8:57:32.5	50.374	68.615			
9	234	0:21:50.7	44.129	85.363	58.0	4.4	EQ
10	239	7:52:21.5	44.148	83.133			EQ
11	239	8:05:26.2	49.982	80.832			EX
12	239	8:51:21.2	54.665	86.488			
13	239	9:38:34.8	46.900	77.389			EX
14	239	11:04:40.5	50.905	83.464			EX
15	242	4:57:11.3	47.808	81.658			
16	243	7:57:42.9	55.739	81.080			EX
17	244	3:44:38.8	43.808	85.948			EQ
18	244	11:58:21.6	54.316	85.648			EX
19	245	7:00:00.0	50.281	72.172	0.0		EX
20	246	7:00:00.0	50.281	72.172	0.0		EX
21	149	9:28:17.0	46.855	78.057			EX

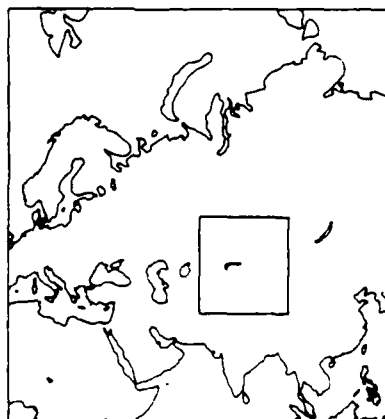
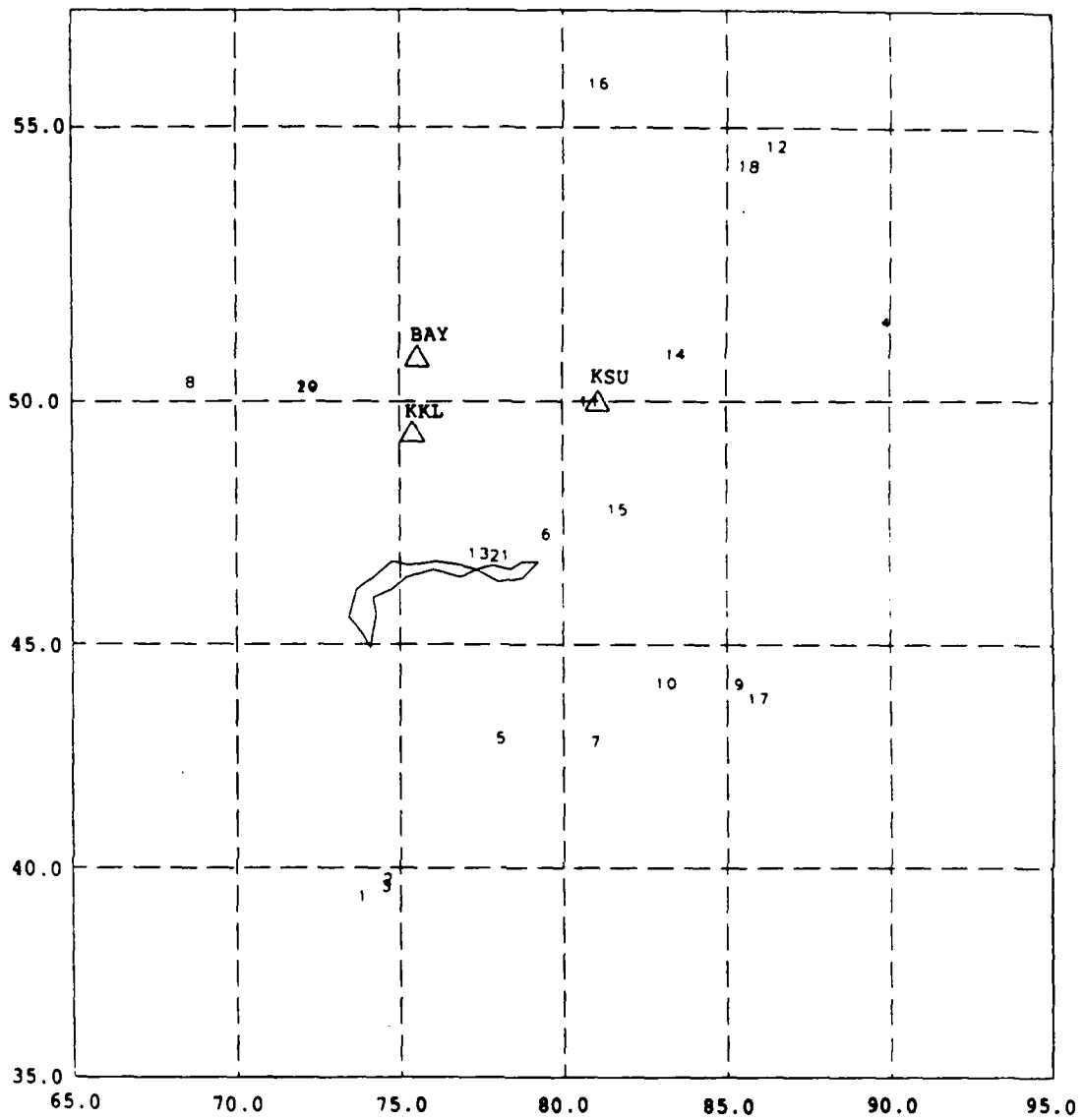


Figure 3.1. Map showing the station locations (triangles) and event locations (numbers) for the NRDC data set. The numbers correspond to the event numbers in Table 3.2.

location. Event 17 is a smaller earthquake that occurred in the same region as Event 9 (Tien Shan), but was not reported in the PDE [Thurber *et al.*, 1989]. Event 13 is a mining explosion near Lake Balkash [Thurber *et al.*, 1989]. Events 19 and 20 are 10-ton calibration shots detonated west of the city of Karaganda [Given *et al.*, 1989]. The locations of the remaining events in Table 3.2 were determined by seismologists at the Center for Seismic Studies (CSS) based on travel time picks from the NRDC data. Event 21 is close to the mining explosion in the Lake Balkash area reported by Thurber *et al.* [1989] and occurred at a similar time of day. Also, the data recorded at Bayanaul display a strong R_g phase which is indicative of shallow depth. Thus, Event 21 is probably a mining explosion in the Lake Balkash area. Events 7 and 10 are probably earthquakes. Their locations are between the PDE locations for Events 5 and 9. The remainder of the events are of unknown origin, though it is likely that many are near-surface explosions.

3.3 Data Processing

The results to be described were obtained by analysis of data from the vertical component borehole sensor. All available short-period data were processed with the procedures described below, but the borehole data are emphasized because the surface seismometers are typically characterized by higher noise levels (particularly at KSU) [Berger *et al.*, 1988]. Also, the vertical component data provide direct comparison to our previous results for NORESS. Appendix A displays the recorded waveforms for all of the events used in this study.

The waveforms for each event-station pair are filtered over four frequency bands, 1–3, 3–5, 4–8, and 8–16 Hz. The broadband and filtered traces are displayed with theoretical arrival times (based on the locations in Table 3.2) for interactive picking of regional phases. Fourier spectra are computed for each phase. A symmetric 10% cosine taper is applied to a time window starting 0.3 s before the picked arrival time. The duration of the analyzed segment depends on the phase identification. For P_n the duration was set to 10 s, and a fixed group velocity window of 3.6 to 3.0 km/s was used to determine the duration for the L_g spectral estimate. Noise spectra for each phase are calculated for a 5-s window starting 5.5 s before the picked arrival time. The noise spectra are normalized to the signal window length using

$$N(f) = \sqrt{\frac{T_s}{T_n}} n(f) \quad (3.1)$$

where $N(f)$ is the normalized noise spectrum, T_s is the window length used to calculate the signal spectrum, T_n is the window length used to calculate the noise spectrum (5 s), and $n(f)$ is the noise spectrum computed using a window length of T_n .

The spectra were corrected for the instrument response and converted to units of displacement. The NRDC borehole instrument response is flat to velocity between 0.2 and 100 Hz [Berger *et al.*, 1988]. The calibration values were obtained for each waveform from the Center for Seismic Studies (CSS) in units of nanometers per digital

count at 1 s. These calibrations were verified for a subset of the data by H. Given at the Institute of Geophysics and Planetary Physics [personal communication]. The displacement spectrum is related to the uncorrected spectrum by

$$A(f) = \frac{X(f)}{2 \pi f I_0} \quad (3.2)$$

where $A(f)$ is the displacement spectrum in nm-s, $X(f)$ is the spectrum of the uncorrected data in count-s, f is frequency in Hz, and I_0 is the instrument response to velocity in counts/(nm/s). The calibration values reported by CSS are expressed in terms of I_0 as

$$\text{calib} = \frac{T_c}{2 \pi I_0} \quad (3.3)$$

where T_c is the calibration period ($T_c = 1$ s). Therefore, the signal and noise spectra were corrected for the instrument response by multiplying by the calibration value and dividing by frequency.

3.4 Attenuation and Source Parameters for Regional Phases

The method of *Sereno et al.* [1988] is used to estimate attenuation and source parameters from the P_n and L_g spectra recorded by the NRDC stations. The instrument-corrected amplitude spectra are parameterized as

$$A(f,r) = S(f) G(r,r_0) \exp\left[\frac{-\pi f t}{Q(f)}\right] \quad (3.4)$$

where $S(f)$ is the source spectrum, $G(r,r_0)$ is the geometric spreading function, and the last term is the apparent attenuation for travel time t . The spectra, $A(f,r)$, are corrected for an assumed geometric spreading function and inverted using damped least squares for two parameters describing the source spectrum and two parameters characterizing a power law frequency dependence of $Q(f)$.

The source spectrum is assumed to falloff as f^{-2} beyond a corner frequency that scales inversely with the cube root of the long-period level, S_0 . The source parameters estimated by the inversion are the long-period source level for each event (which is proportional to seismic moment) and a single parameter that relates corner frequency and long-period level for all events. The relationship between source moment and L_g S_0 for earthquakes is

$$S_0^{\text{eq}}(L_g) = \frac{M_0^{\text{eq}}}{4\pi\rho_c\beta_c^3} \quad (3.5)$$

where M_0^{eq} is the earthquake moment, ρ_c is the average crustal density, and β_c is the average shear-wave velocity of the crust. The relationship between $Pn S_0$ and earthquake moment depends on the source radiation pattern. Since the focal mechanisms for the events studied are unknown, it is not possible to obtain accurate estimates of source moment from the derived Pn source levels. However, explosion moments can be estimated from $Pn S_0$ using

$$S_0^{exp}(Pn) = \frac{M_0^{exp}}{4\pi\rho_s\alpha_s^3} \quad (3.6)$$

where ρ_s and α_s are the near-surface density and compressional-wave velocity, respectively. Since the excitation function for Lg is unknown for near-surface explosions it is not possible to estimate explosion moments from $Lg S_0$.

In this report the geometric spreading function is assumed to be independent of frequency and is characterized by a power law range dependence

$$\begin{aligned} G(r,r_0) &= (1/r) && \text{for } r \leq r_0 \\ G(r,r_0) &= r_0^{-1} (r_0/r)^m && \text{for } r \geq r_0 \end{aligned} \quad (3.7)$$

where r is epicentral distance and r_0 is a transition distance from spherical spreading to spreading rate m . The Lg phase consists of higher-mode surface waves which are accurately described at long ranges by cylindrical spreading ($m = 1/2$), provided the window length is sufficient to encompass the entire dispersed wave train. By comparing the long-period amplitude spectrum of Lg to moments calculated from long-period surface waves, *Street et al.* [1975] empirically determined $r_0 \approx 100$ km, or roughly twice the crustal thickness. Measuring the decay rate of synthetic Lg phases computed for an elastic medium, *Herrmann and Kijko* [1983] verified that Lg frequency domain spreading was accurately described as cylindrical and substantiated the empirical result of *Street et al.* [1975] for r_0 . Therefore Lg geometric spreading is approximated by (3.7) with $r_0 = 100$ km and $m = 1/2$.

As discussed at length in Section 1 of this report, the geometric spreading of Pn is a complicated function of the velocity gradient in the upper mantle, and it is probably frequency dependent. Therefore a simple parameterization such as (3.7) is not likely to be applicable to Pn over a broad frequency and distance range. However, over limited distance ranges and at long periods a power law range dependence may be adequate to approximate the spreading of Pn . For example, Figure 3.2 plots synthetic Pn attenuation at 1.25 Hz for an elastic earth model consisting of a 40-km-thick homogeneous crust over a mantle with a compressional-wave velocity gradient of 0.0013 s^{-1} (Model 2, Section 1). This gradient corresponds to the earth-flattening transformation of a homogeneous upper mantle. The dashed curve is the best-fitting power law model determined by least squares. The spreading rate for this model is $r^{-1.25}$. Note that the difference between these two curves is considerably less than the standard deviation of typical $\log M_0$ versus magnitude relations (≈ 0.3) [e.g., *Veith and Clawson*, 1972; *Dwyer et al.*, 1983; *Hasegawa*, 1983; *Sereno et al.*, 1988]. *Sereno et al.* [1988]

Pn Geometric Spreading

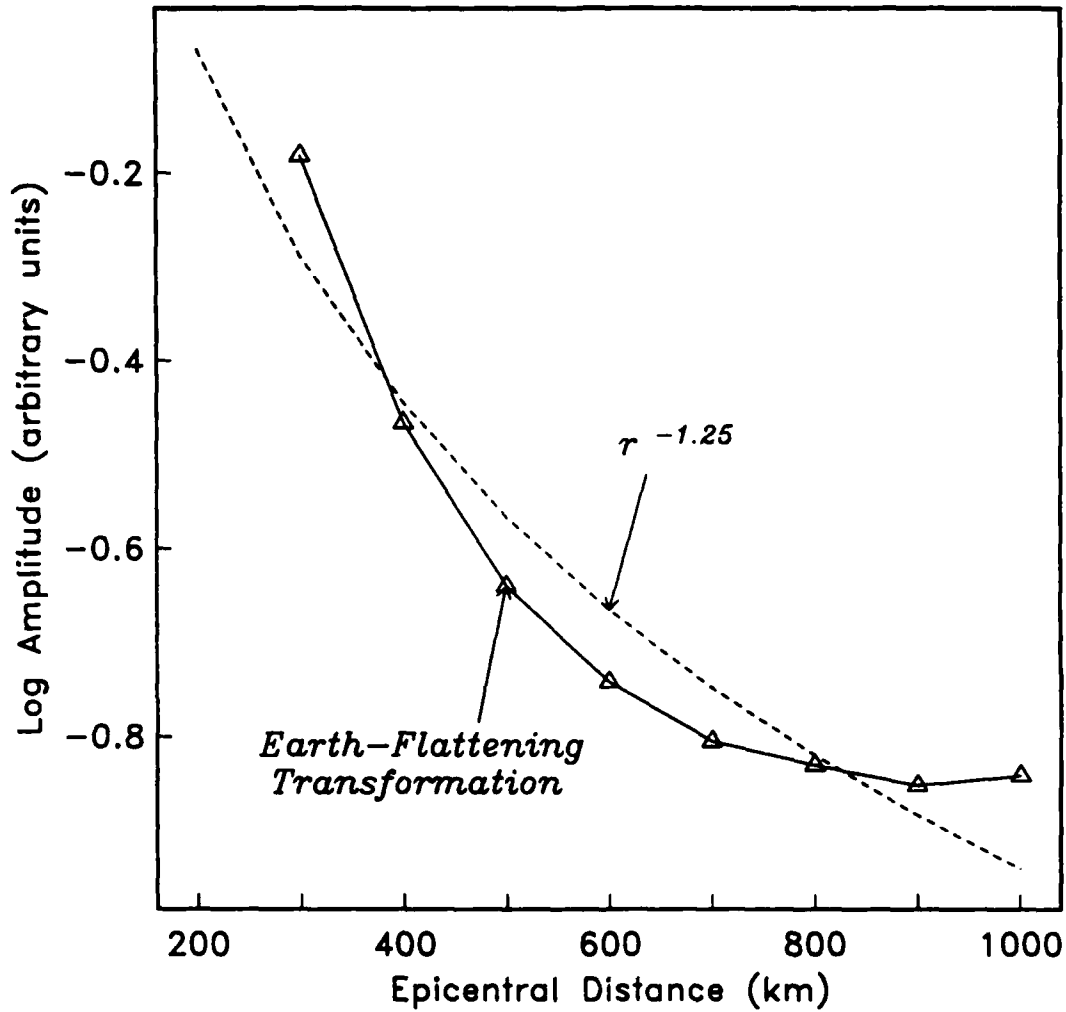


Figure 3.2. *Pn* geometric spreading. The solid curve is the *Pn* attenuation with distance at 1.25 Hz calculated for an elastic earth model with upper mantle velocity gradient equivalent to the earth-flattening transformation of a homogeneous medium (Model 2, Section 2). The dashed curve plots a power law distance dependence $r^{-1.25}$ determined by a least squares fit to the synthetic *Pn* attenuation.

estimate $P_n Q(f)$ from data recorded at NORESS by assuming frequency-independent geometric spreading functions with range dependencies of r^{-1} , $r^{-1.3}$, and $r^{-1.5}$. For each of these they found $Q(f)$ models consistent with the observed spectra. However, $r^{-1.3}$ was found to give moments that were consistent with the moments derived from the separate L_g inversion. Thus, the P_n spreading model near 1 Hz derived by *Sereno et al.* [1988] is generally consistent with an upper mantle model with a slight positive velocity gradient. However, the $P_n Q(f)$ determined by *Sereno et al.* [1988] includes any frequency dependence occurring in the geometric spreading function, and so it probably does not represent upper mantle anelasticity.

3.4.1 L_g Inversion Results

The L_g inversion includes 37 spectra from 21 events recorded by up to three stations. The spectra were inverted between 0.5 and 2.5 Hz. This frequency range is based on a comparison of the L_g spectra to the pre- L_g noise spectra normalized to the signal window length (see Appendix B). The result of the inversion is a range of attenuation and source models corresponding to a broad minimum in the data residuals. For example, Figure 3.3 plots the value of $L_g Q$ at 1 Hz (Q_0) against the exponent of a power law frequency dependence (η) for models that produce data variances that differ by less than 1%. This range of models was determined by fixing η and inverting for Q_0 , S_0 for each event, and the corner frequency scaling parameter. In general, models with low Q_0 are associated with higher source levels than models with high Q_0 since the combination these parameters is constrained to fit the same 1-Hz amplitude. Models with low Q_0 are also associated with high values of η since these parameters are constrained by spectral shape. Since most of the events have corner frequencies greater than the upper limit of the frequency band inverted, the attenuation results are insensitive to the source assumptions.

A simple constraint that can be applied to reduce the trade-off among model parameters is to require consistency in the source levels derived for each event from data recorded at different stations. For example, Figure 3.4 plots $L_g S_0$ for two of the $Q(f)$ models in Figure 3.3. The model with higher Q_0 produces more consistent source levels from data recorded at different stations than the model with lower Q_0 . For example, the source levels for Events 9 and 17 derived from three stations are nearly the same for $L_g Q(f) = 650$ but differ by over 50% for $L_g Q(f) = 345f^{0.4}$. The difference in epicentral distance between the furthest and closest station for these events is over 300 km. Events 1, 5, 11, and 14 also have more consistent source levels for the higher Q_0 model. In general, there is a distance dependence in the derived source levels for events recorded at multiple stations for models with Q_0 less than about 500. This implies that $L_g Q_0$ is greater than or equal to 500. Appendix B plots the L_g spectra and theoretical spectra based on the model with $L_g Q(f) = 650$.

Given et al. [1989] estimated $L_g Q$ by applying a spectral ratio method to data recorded from one of the 10-ton calibration shots (Event 20). They concluded that the average value of Q at 1 Hz is 500 and increases with frequency although the frequency

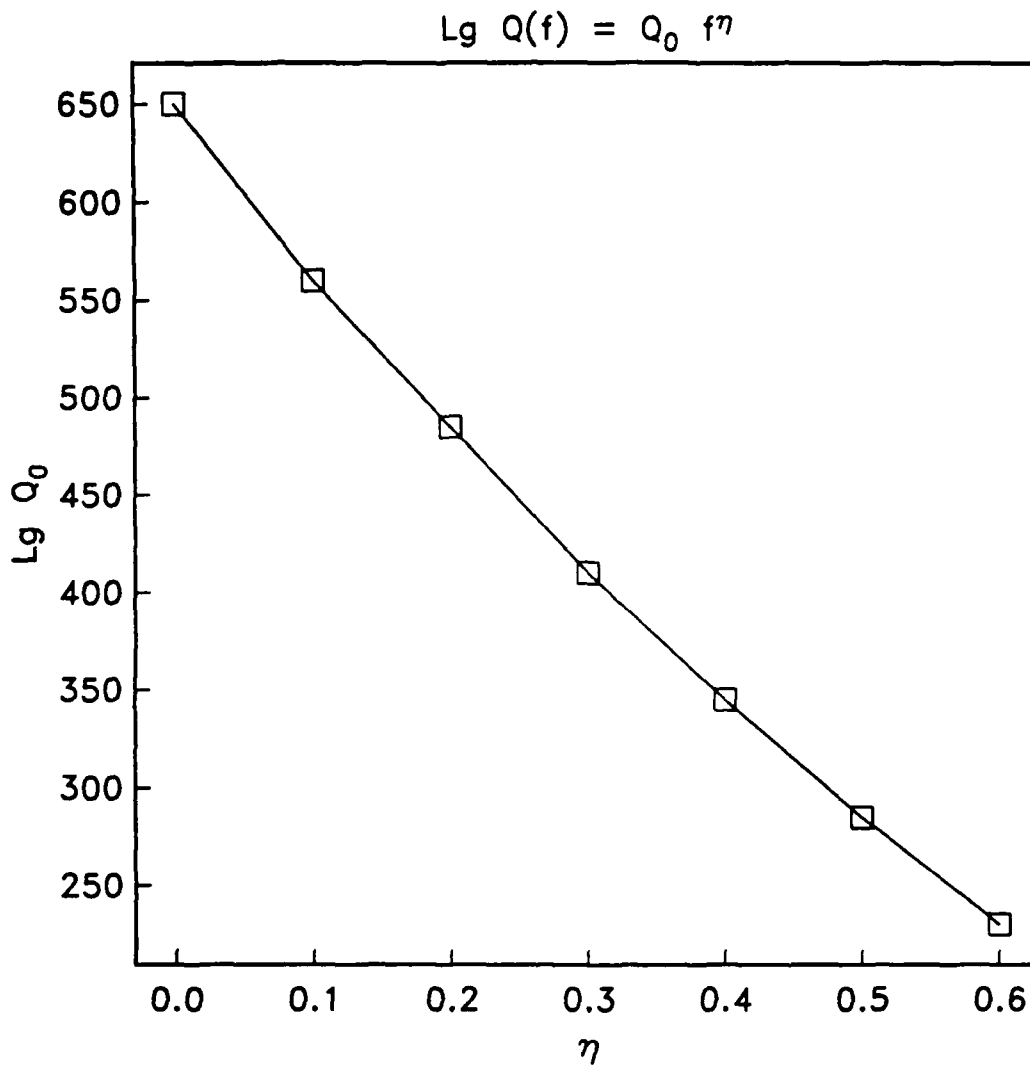


Figure 3.3. $\text{Lg } Q(f)$ models consistent with the NRDC observations. The value of $\text{Lg } Q$ at 1 Hz (Q_0) is plotted against the exponent of a power law frequency dependence (η). These models combine with different source levels to produce data variances that differ by less than 1%.

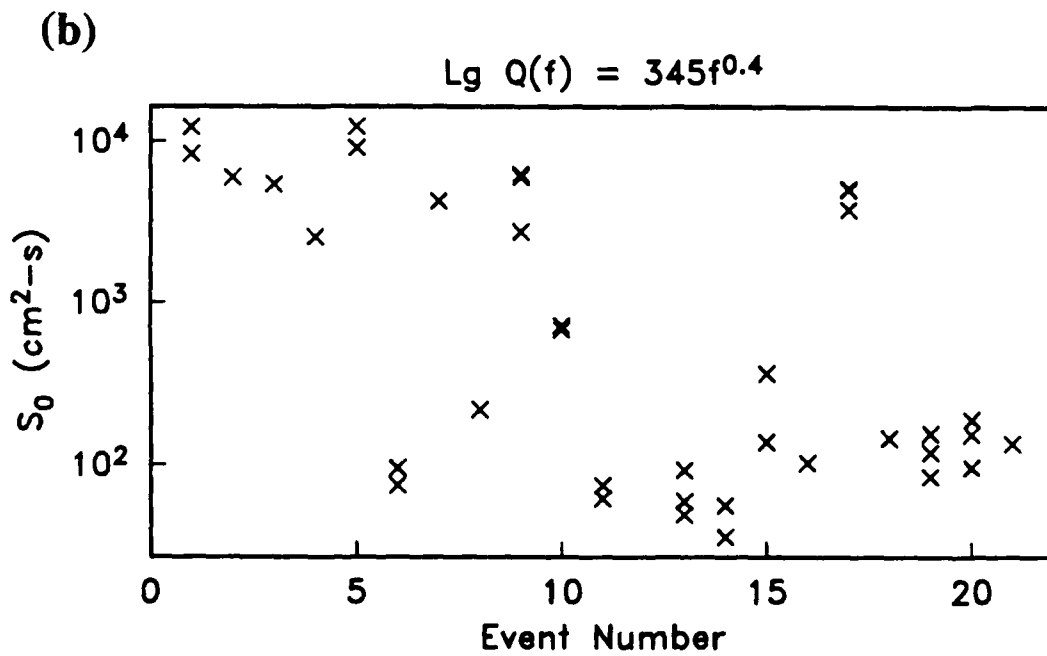
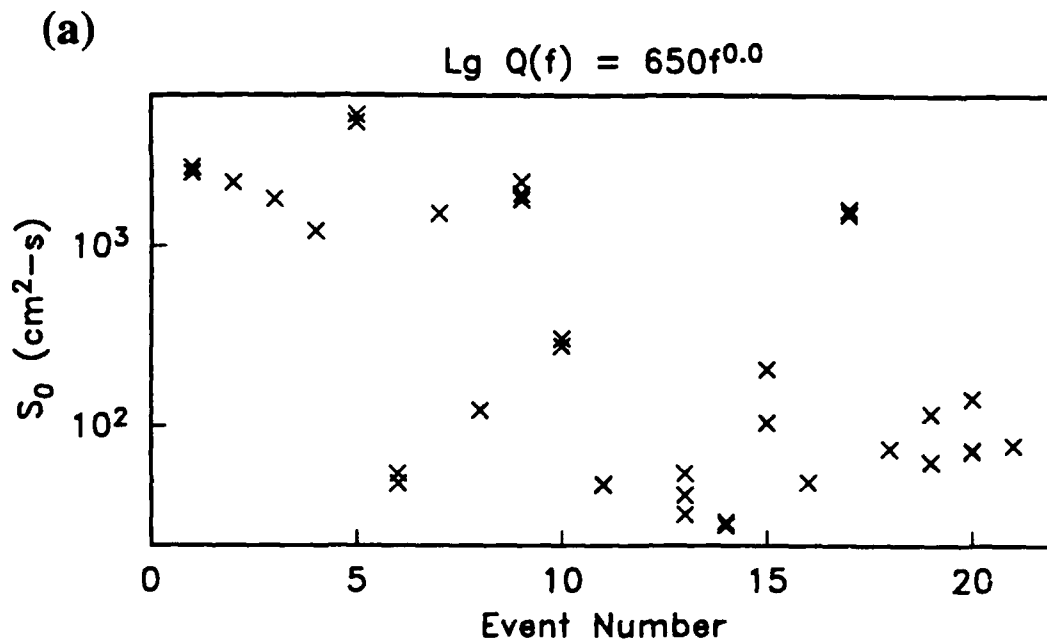


Figure 3.4. Derived source levels (S_0) for (a) $Lg Q(f) = 650$ and (b) $Lg Q(f) = 345f^{0.4}$. The event numbers are from Table 3.2. Events recorded at multiple stations have an S_0 estimate from each station. Note that the higher Q_0 model reduces the variance in the derived source levels from multiple station observations.

exponent is poorly constrained. They approximate the frequency dependence as $f^{0.4}$ to about 5 Hz with a possible increased dependency at higher frequency. Their $Lg Q$ at 1 Hz is consistent with the value obtained here, but the frequency exponent is somewhat higher. For example, the model in Figure 3.3 with Q_0 equal to 500 has a frequency exponent close to 0.2. This model is constrained by data at frequencies less than 2.5 Hz. A comparison of the pre- Lg noise spectrum with the Lg signal spectrum for this event suggests that Sn coda may contaminate the Lg spectrum at KSU beyond 4–5 Hz (Figure A2.20). Thus the higher frequency exponent for $Lg Q$ determined by *Given et al.* [1989] may reflect an increased contribution of Sn coda at high frequencies.

The earthquake moments are estimated from $Lg S_0$ using (3.5) with $\rho_c = 2.5 \text{ gm/cm}^3$ and $\beta_c = 3.5 \text{ km/s}$. The S_0 are approximately equal to the logarithmic mean of the source level below the corner frequency. *Herrmann and Kijko* [1983] use synthetic Lg spectra to demonstrate that the logarithmic mean plus one standard deviation (close to the peak rather than the mean spectral amplitude) should be used for the S_0^{est} in (3.5). Since the standard deviation of $\log S_0$ is approximately 0.3, the S_0 are multiplied by two before estimating earthquake moment using (3.5). Figure 3.5 plots earthquake moment versus m_b for the Lg model with $Q(f) = 650$. The symbols indicate the moments of the five events in Table 3.2 with PDE magnitudes and the solid lines are the moment-magnitude relations listed in Table 3.3. Note that the moments derived in this study are generally consistent with the moment versus magnitude relations determined for eastern North America and Scandinavia. The dashed lines in Figure 3.5 indicate the moments of earthquakes that are not listed in the PDE Bulletin (Events 7, 10, and 17). Comparing these to the moment versus magnitude relations indicates that the magnitudes of Events 7 and 17 are between 4.1 and 4.4 and that the magnitude of Event 10 is between 3.2 and 3.4.

The relationship between corner frequency (f_c) and moment for the $Lg Q = 650$ model is

$$f_c = 6.26 \times 10^7 M_0^{-1/3} \quad (3.8)$$

which implies a corner frequency of 2.6 Hz for the largest event in the data set (Event 5, Table 3.2). Since this is greater than the maximum frequency used in the Lg inversion, the corner frequency scaling parameter cannot be resolved with much confidence. However, *Somerville et al.* [1987] determined a similar relation for events in eastern North America. They determined source moment and duration of 13 events with m_{blg} between 4.7 and 6.6 by modeling waveforms of seismic body phases. They found that the relationship between source duration and moment is consistent with constant stress drop scaling and that the median stress drop is approximately 100 bars. Their relationship between corner frequency and moment is

$$f_c = 8.58 \times 10^7 M_0^{-1/3} \quad (3.9)$$

Note that both (3.9) and (3.8) give corner frequencies greater than 2.5 Hz for all of the events studied.

Earthquake Moment-Magnitude Relations

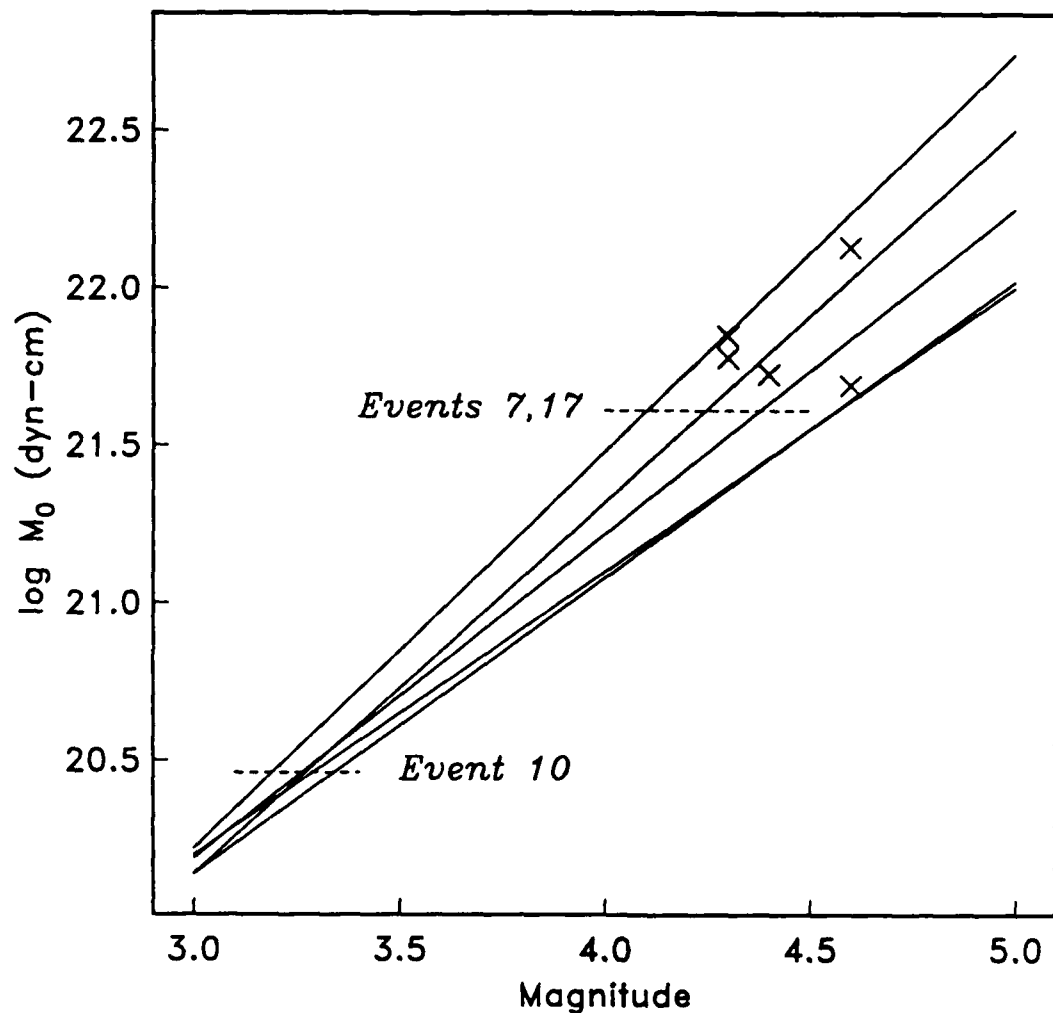


Figure 3.5. Moment versus magnitude for presumed earthquakes in the NRDC data set. The moments are calculated from the L_g source levels using (3.5) and are plotted against the m_b reported in the PDE Bulletin (Events 1, 2, 3, 5, and 9 in Table 3.2). The solid lines are moment versus magnitude relations determined in previous studies (Table 3.3). The dashed horizontal lines are moments of earthquakes not reported in the PDE Bulletin.

Table 3.3 Moment Versus Magnitude Relations

M_L	$\log M_0$	Region	Reference
-0.4-2.2	$0.90M_L + 17.50$	Scandinavia	<i>Bungum et al.</i> [1982]
1.8-4.9	$1.26M_L + 16.44$	Central United States	<i>Dwyer et al.</i> [1983]
1.0-4.2	$0.94M_L + 17.32$	E. North America	<i>Hasegawa</i> [1983]
2.1-4.3	$1.18M_L + 16.60^\dagger$	E. North America	<i>Shin and Herrmann</i> [1987]
1.1-3.8	$1.03M_L + 17.10$	Scandinavia	<i>Sereno et al.</i> [1988]

† The regression coefficients were estimated from tabulated moments and magnitudes.

3.4.2 *Pn* Inversion Results

The *Pn* inversion includes 26 spectra from 21 events recorded by up to three stations. The spectra were inverted between 1 and 10 Hz based on signal-to-noise ratio. As was the case for *Lg*, a range of attenuation and source models produce similar data variances. Figure 3.6 plots *Pn* Q_0 against η for models that produce data variances that differ by less than 1%. This range of models was determined by fixing η and inverting for S_0 for each event, Q_0 , and the corner frequency scaling parameter.

The wide range of *Pn* $Q(f)$ models in Figure 3.6 cannot be distinguished on the basis of source levels derived from data at different stations. For example, Figure 3.7 plots *Pn* S_0 for two very different $Q(f)$ models that fit the data equally well. The source levels inferred from different stations are no more consistent for one of these models than for the other. Part of the problem is that there are only a few events with *Pn* data from multiple stations. Other factors that may contribute to the difficulty are (1) an invalid geometric spreading assumption, (2) radiation pattern, (3) local site effects and (4) propagation path differences. Whatever the cause, the consistency of derived source levels cannot be used to resolve trade-offs among source and path parameters as was done for *Lg*. For this reason, Appendix B plots the *Pn* spectra and theoretical spectra based on derived attenuation models that represent the extremes ($Q(f) = 1175$ and $Q(f) = 300f^{0.5}$).

The explosion moments are calculated from *Pn* S_0 using (3.6) with $\rho_s = 2.5 \text{ gm/cm}^3$ and $\alpha_s = 5.0 \text{ km/s}$. Events 13, 19, and 20 are known to be explosions [Thurber *et al.*, 1989]. Event 21 is also probably an explosion in the Lake Balkash area (see Section 3.2). Other likely explosions are Events 11, 14, 16, and 18, based on low *Lg/Pn* ratios, origin time (morning to mid-afternoon), location and general aseismicity of the region near the eastern Kazakhstan explosion test site [Thurber *et al.*, 1989], and the presence of *Rg*. The *Lg* magnitudes of these events are calculated using the correction table applied at NORESS (it will be shown in Section 3.6 that *Lg* attenuation in eastern Kazakhstan is similar to that observed at NORESS, so application of the NORESS correction table is reasonable). Figure 3.8 plots explosion moment versus *Lg* magnitude for the two $Q(f)$ models. The moments are averaged for events recorded at multiple stations. The solid line is the moment-magnitude relation determined by Sereno *et al.* [1988] for mining explosions recorded at NORESS:

$$\log M_0^{\text{exp}} = 1.08 M_L + 17.6 \quad (3.10)$$

The model with *Pn* $Q(f) = 1175$ gives explosion moments consistent with (3.10), while the $Q(f) = 300f^{0.5}$ model fits the line about as well when the intercept is about 0.3 higher. Without independent estimates of source moment it is not possible to determine which of these models more accurately separates source and path contributions to the observed amplitudes.

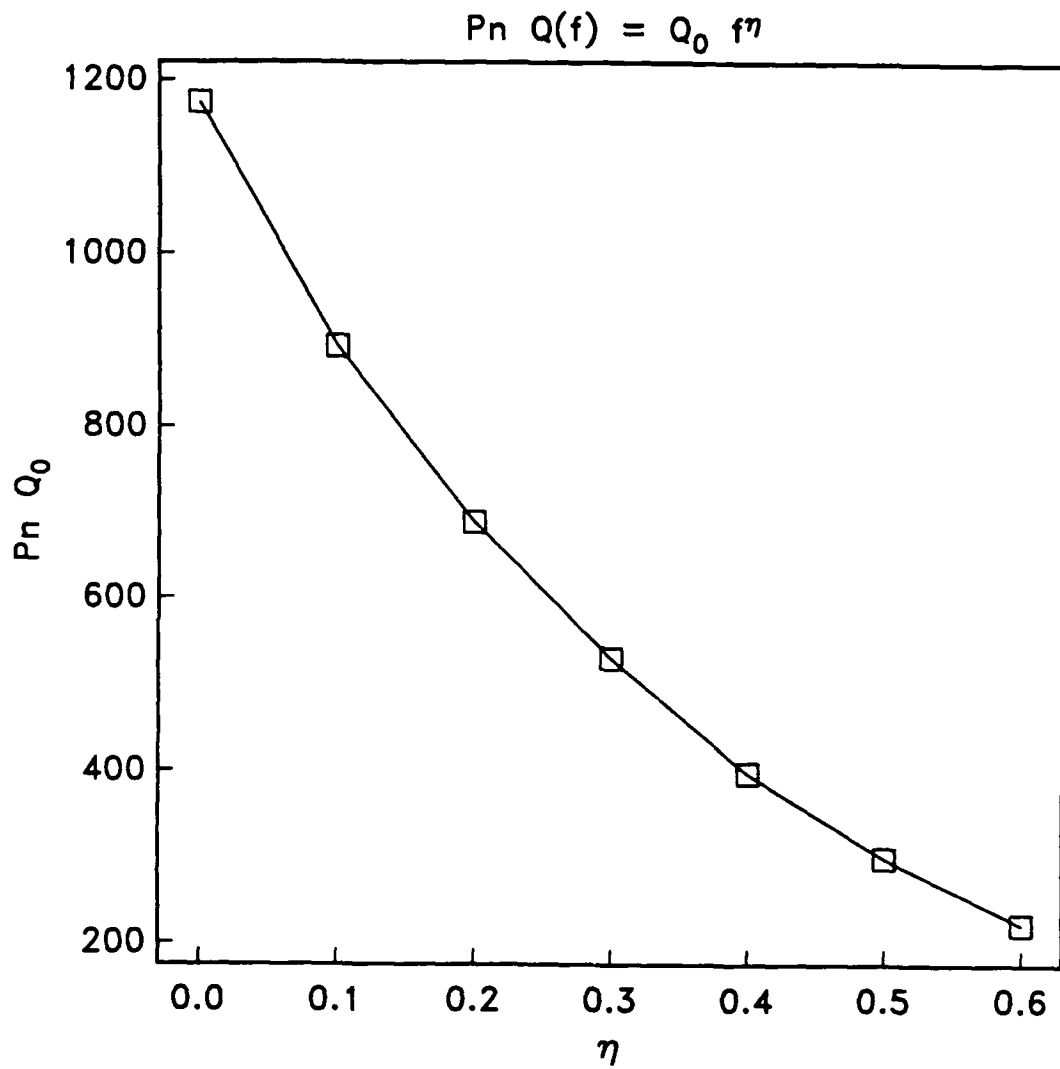
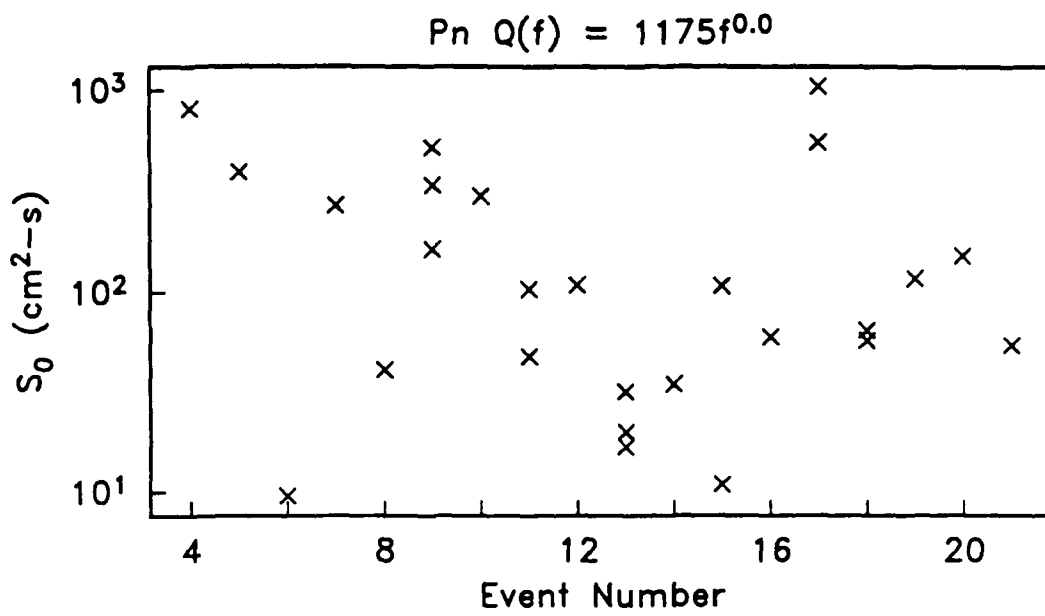


Figure 3.6. $P_n Q(f)$ models consistent with the NRDC observations. The value of $P_n Q$ at 1 Hz (Q_0) is plotted against the exponent of a power law frequency dependence (η). These models combine with different source levels to produce data variances that differ by less than 1%.

(a)



(b)

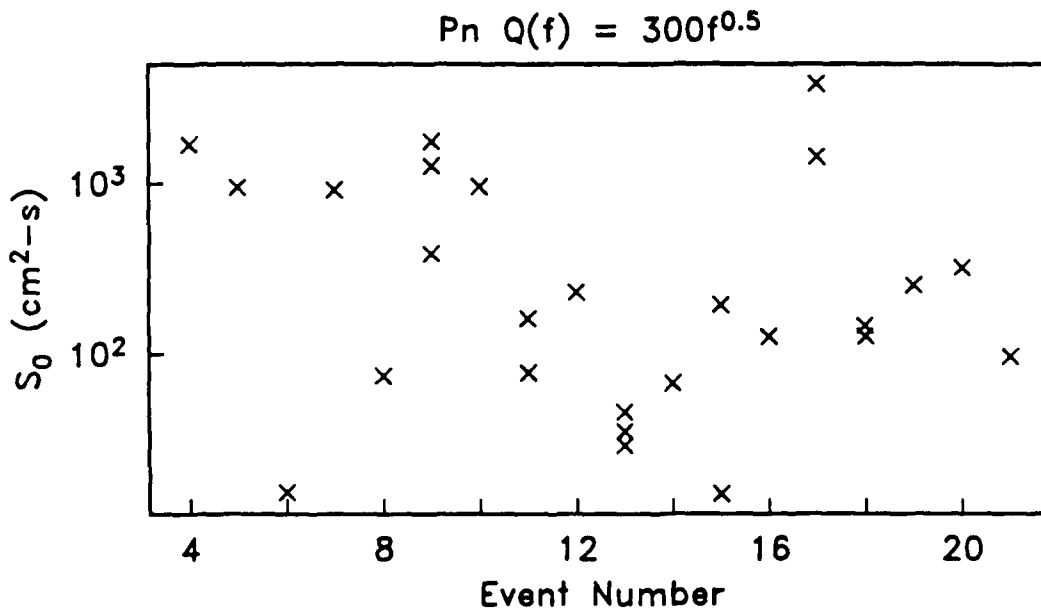


Figure 3.7. Derived source levels (S_0) for (a) $P_n Q(f) = 1175$ and (b) $P_n Q(f) = 300f^{0.5}$. The event numbers are from Table 3.2. Events recorded at multiple stations have an S_0 estimate from each station.

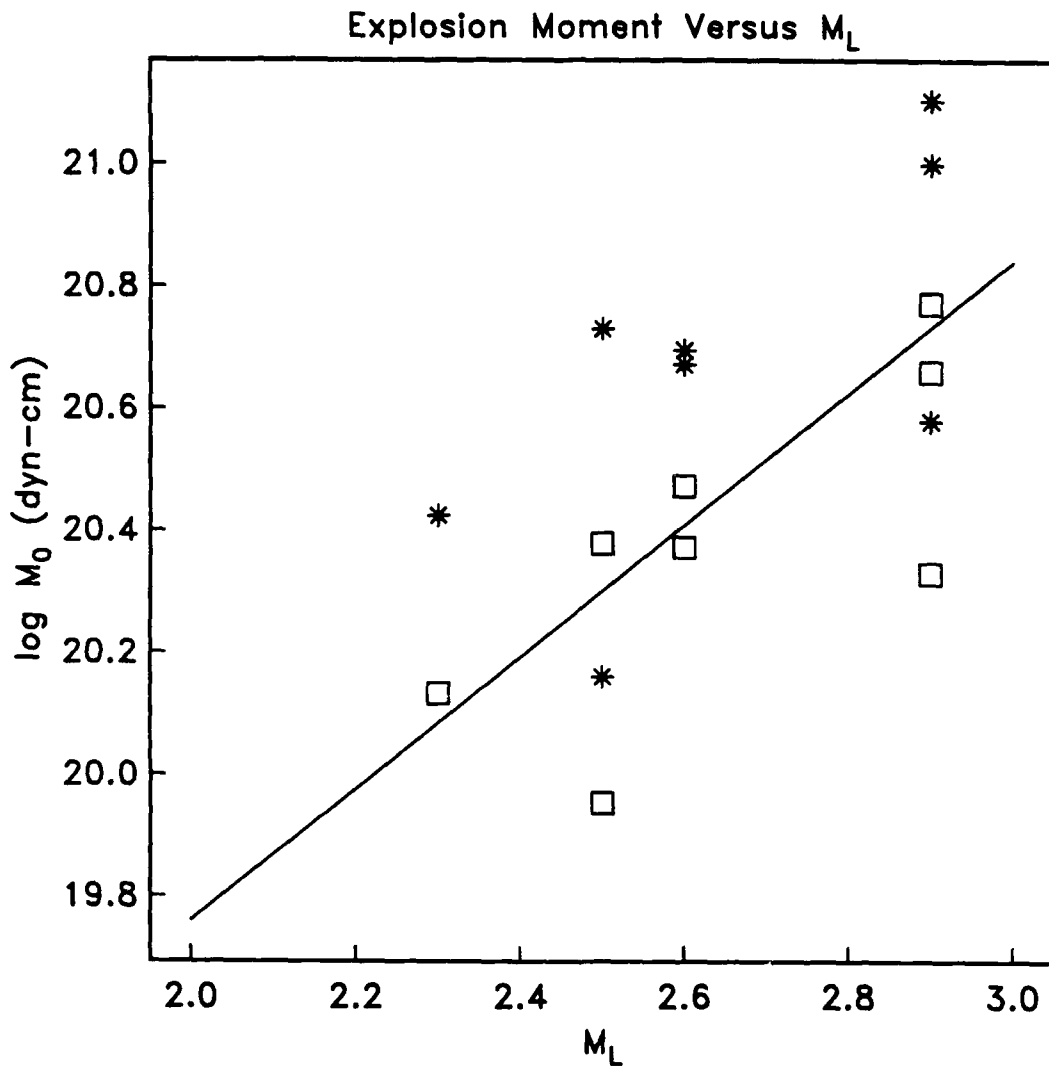


Figure 3.8. Moment versus magnitude for presumed explosions in the NRDC data set. The moments are calculated from the P_n source levels using (3.6) and are plotted against Lg magnitude (Events 11, 13, 14, 16, 18, 19–21 in Table 3.2). The asterisks are moments calculated for the $P_n Q(f) = 300f^{0.5}$ model and the squares are for the $P_n Q(f) = 1175$ model. Note that the moments for the lower Q_0 model are about a factor of 2 higher than the moments associated the higher Q_0 model. The solid line is the explosion moment versus magnitude relation determined by Sereno *et al.* [1988] from NORESS observations.

The relationship between corner frequency and explosion moment for the model with $P_n Q(f) = 1175$ is

$$f_c = 4.65 \times 10^7 M_0^{-1/3} \quad (3.11)$$

This relationship for the $Q(f) = 300f^{0.5}$ model is

$$f_c = 6.31 \times 10^7 M_0^{-1/3} \quad (3.12)$$

These give similar corner frequencies since the M_0 are a factor of two higher for the lower Q_0 model. Both give the corner frequency of an M_L 3.0 explosion to be between 5.0 and 6.0 Hz. Note that *Given et al.* [1989] used a curve-fitting algorithm to determine the corner frequency of Event 20 ($M_L = 2.9$) to be 5–6 Hz from L_g spectra and 7 Hz from P_g spectra.

3.5 Noise Spectra

It is shown in this section that ambient noise spectra recorded at NORESS are similar to noise spectra recorded by the borehole seismometer at the NRDC stations. *Berger et al.* [1988] provide a detailed description of the noise at the NRDC stations, including plots of ambient noise spectra from 1 to 100 Hz for windy and calm conditions for the borehole and surface instruments at each of the three NRDC stations. This section provides a direct comparison of the NORESS noise spectra and the NRDC station noise spectra computed in exactly the same way between 1 and 20 Hz.

The NORESS single-channel noise spectrum is calculated from 43 samples with 5-s windows [*Henson and Bache*, 1988]. Each of these "samples" is the average spectrum for all elements of the NORESS array. The NRDC station noise spectra are estimated from samples taken prior to P_n detections. They include 26 samples with 5-s windows, and data from the three NRDC stations have been averaged together. Figure 3.9 plots the average NRDC ambient noise spectrum computed (solid curve) bounded by one standard deviation (dashed curves). The dotted curve is the average ambient noise spectrum at NORESS taken from *Henson and Bache* [1988]. The NORESS noise spectrum is within one standard deviation of the average noise spectrum for the NRDC stations.

3.6 Comparison to NORESS Data

This section compares the parameterization of L_g and P_n signal spectra derived in Section 3.4 for the NRDC stations to the parameterization of these spectra for events recorded at NORESS determined by *Sereno et al.* [1988]. Figure 3.10 plots theoretical L_g spectra at 800 km for an M_L 3.0 event based on the NORESS and NRDC $Q(f)$ models. The solid curve is the L_g spectrum for one of the models ($Q(f) = 650$) that fits the NRDC station data, and the dashed curve is the L_g spectrum for a model ($Q(f) = 560f^{0.26}$) that fits the NORESS data. The same source spectrum was used for both curves. The spectra are very similar between 0.5 and 2.5 Hz (the frequency band used

Ambient Noise Spectra

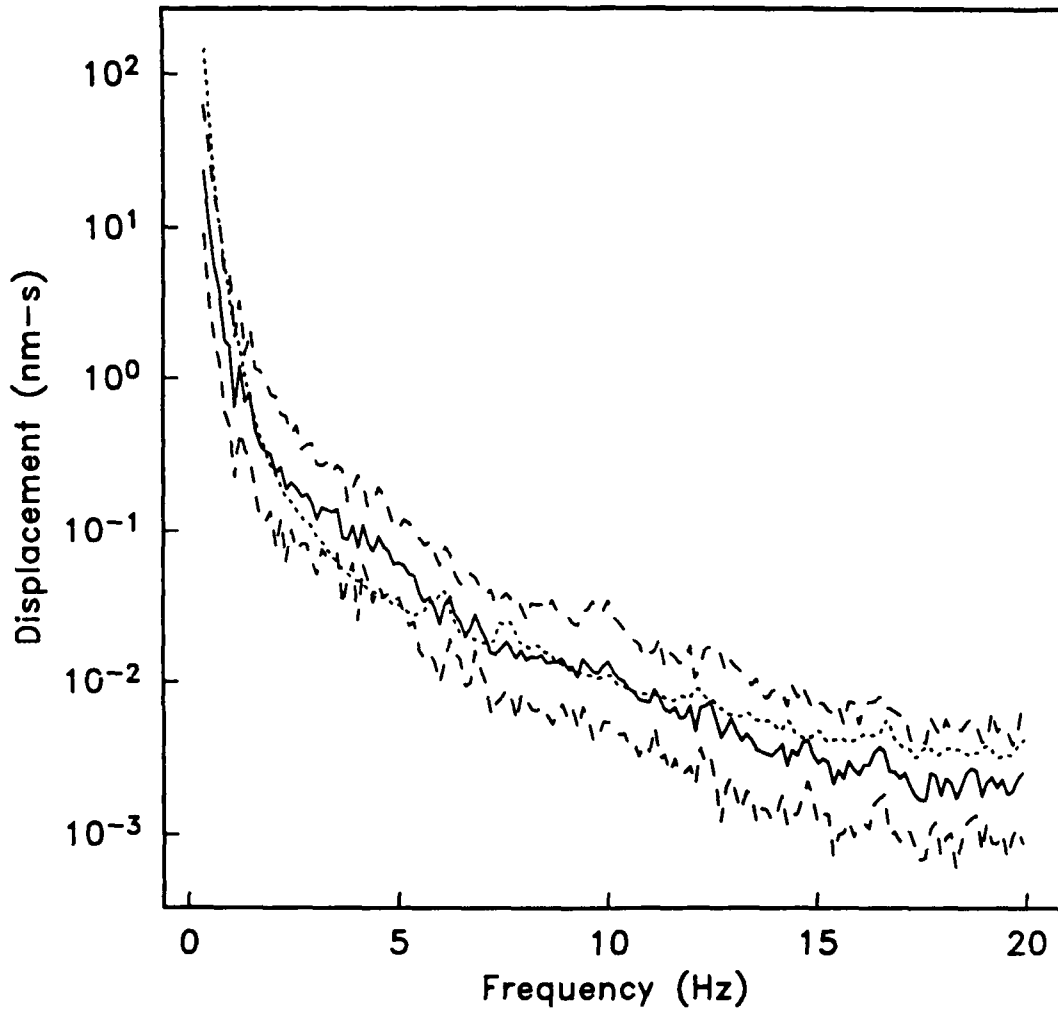


Figure 3.9. Ambient noise displacement spectra for a 5-s window. The solid curve is the average noise spectrum at the three NRDC stations calculated from 26 samples taken prior to P_n . The dashed curves indicate one standard deviation. The dotted curve is the average ambient noise spectrum at NORESS based on 43 samples taken prior to P_n [Henson and Bache, 1988].

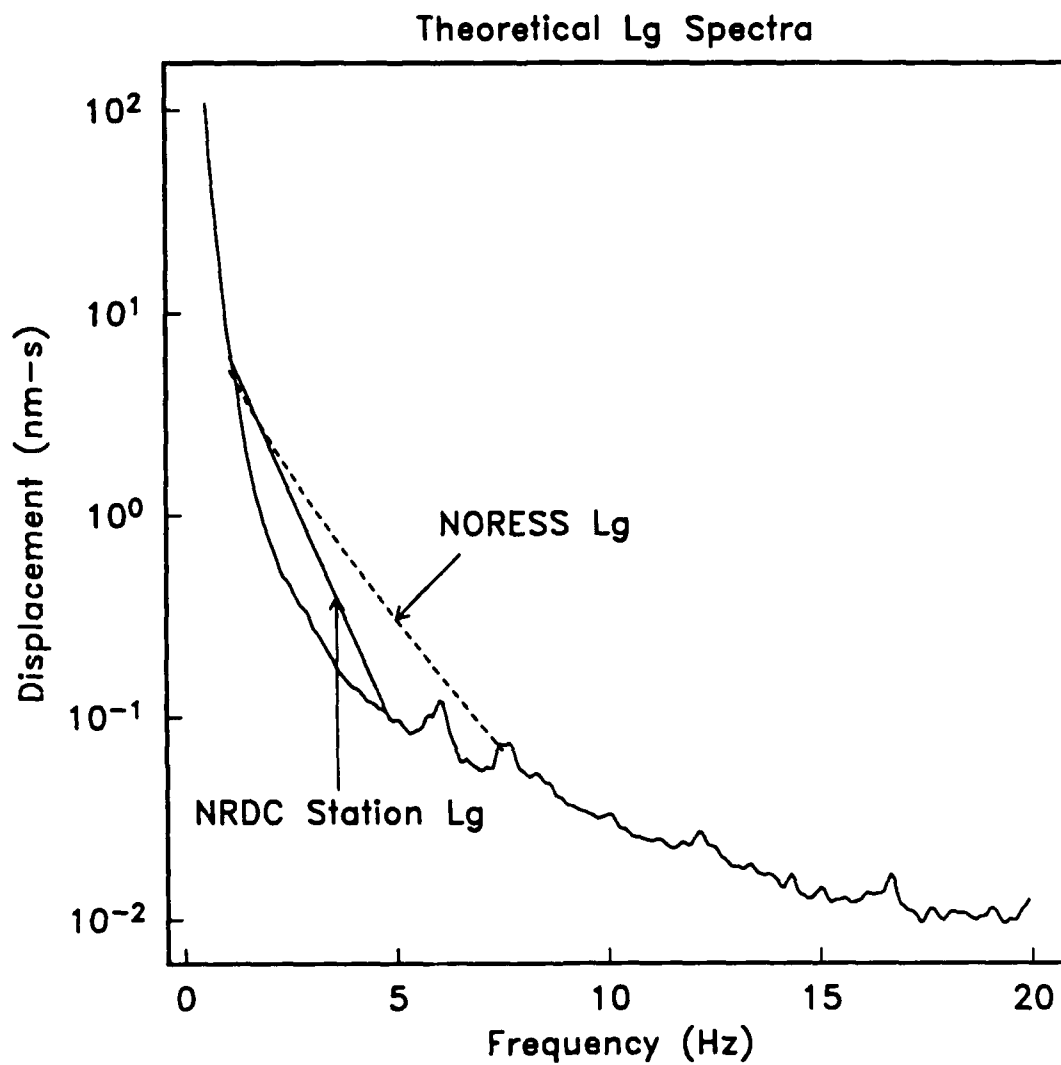


Figure 3.10. Theoretical L_g spectra at 800 km for a magnitude 3.0 event based on the inversion results using the NRDC (solid) and NORESS data (dashed). The bottom curve is the average NORESS ambient noise scaled to the L_g signal window length at 800 km. This curve is plotted only for reference. The actual L_g spectrum is contaminated by the coda of previous arrivals which is larger than the ambient noise.

in the inversion of the NRDC data) but differ at higher frequencies. The NORESS model was estimated from 1 to 7 Hz using events at distances greater than 1000 km. At these ranges the higher-frequency S_n coda influences the spectra above 3 Hz, and thus raises the frequency exponent in the Q model. For example, *Sereno and Bratt* [1988] show that NORESS $L_g Q(f) = 582f^{0.18}$ for frequencies between 1 and 3 Hz. Thus, the difference between the two L_g spectra above 3 Hz in Figure 3.10 may be due to the effect of S_n coda included in the NORESS spectra, but not seen in the lower frequency NRDC station spectra.

A range of P_n attenuation and source models was determined in Section 3.4, and it is not possible to resolve the parameter trade offs without independent estimates of source moment. Therefore, in Figure 3.11 P_n spectra for two extreme models consistent with the NRDC spectra from 1 to 10 Hz are compared to P_n spectra for the NORESS model determined by *Sereno et al.* [1988]. These model P_n spectra are computed at 800 km for an M_L 3.0 explosion. Table 3.4 lists the parameters for the calculation. The two solid curves representing the NRDC data are very similar for the 1–10 Hz frequency band used in the inversion. The NORESS spectrum has a similar shape between 1 and 10 Hz, but its amplitude is lower by about a factor of two. The differences beyond 10 Hz are caused by differences in the source parameters. The corner frequency of the NORESS model for an M_L 3.0 explosion is 10 Hz, while for the NRDC models it is between 5 and 6 Hz. However, the attenuation model at NORESS is included in the range of attenuation models found to fit the NRDC data between 1 and 10 Hz (compare the first and last rows in Table 3.4). The main difference is that the P_n amplitude is smaller at NORESS for fixed source moment.

3.7 Summary

Regional P_n and L_g spectra recorded by three seismic stations near the eastern Kazakhstan nuclear explosion test site are inverted for source and attenuation parameters. These results are compared to results obtained with the same methods using P_n and L_g spectra recorded by the NORESS array in Scandinavia. The main conclusions are:

1. The attenuation of L_g spectra between 0.5 and 2.5 Hz in eastern Kazakhstan is consistent with cylindrical geometric spreading and a constant Q equal to 650. Frequency-dependent models are also consistent with the L_g spectra. However, these models produce a greater variance in the moments estimated for the same event recorded at multiple stations.
2. The P_n spectra between 1 and 10 Hz in eastern Kazakhstan are consistent with $r^{-1.3}$ geometric spreading and a wide range of $Q(f)$ models varying from a constant Q of 1175 to a $Q(f) = 220f^{0.6}$. Each of these models provides a different set of source moment estimates, but an independent estimate of source moment is necessary to favor one and resolve the parameter trade offs. It should be emphasized that the $P_n Q$ models include the frequency dependence of geometric spreading, and therefore they are not a direct estimate for upper mantle anelasticity.

Theoretical P_n Spectra

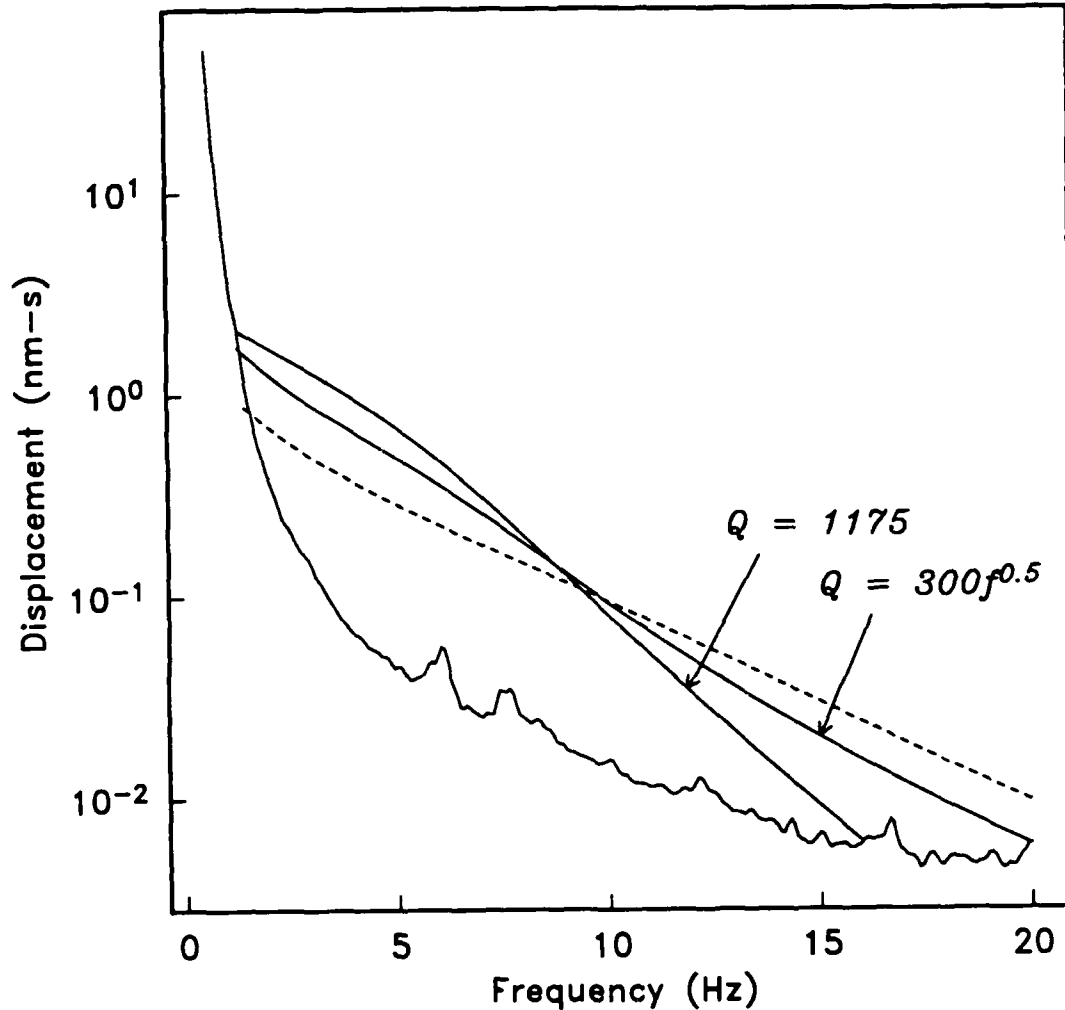


Figure 3.11. Theoretical P_n spectra at 800 km for a magnitude 3.0 explosion based on the inversion results using the NRDC (solid curves) and NORESS data (dashed). The results for two NRDC P_n models are plotted since parameter trade-offs cannot be resolved on the basis of source moment. Model parameters are listed in Table 3.4. The bottom curve is the average NORESS ambient noise scaled to a 10-s window length.

Table 3.4 P_n Attenuation and Source Parameters

Database	Q_0	η	$\log M_0$	$c = f_c M_0^{1/3}$
NORESS	325	0.48	$1.08M_L + 17.6$	8.77×10^7
NRDC	1175	0.00	$1.08M_L + 17.6$	4.65×10^7
NRDC	300	0.50	$1.08M_L + 17.9$	6.31×10^7

3. The average ambient noise spectrum at NORESS falls within one standard deviation of the average noise spectrum observed at the three NRDC stations prior to the 26 P_n recordings used in this study.

4. L_g attenuation near the nuclear explosion test site in eastern Kazakhstan is very similar to the L_g attenuation observed at NORESS in the 0.5 to 2.5 Hz band. Extrapolation of the NRDC station model to higher frequency indicates differences in propagation characteristics but this difference may simply reflect different contributions from S_n coda because of the different frequency bands used to determine the different Q models.

5. The P_n spectral shape in eastern Kazakhstan is similar to that observed at NORESS between 1 and 10 Hz. The attenuation model derived by *Sereno et al.* [1988] for NORESS ($Q(f) = 325f^{0.48}$) fits the NRDC station data as well as any of the other models. However, the the P_n amplitudes between 1 and 5 Hz are about a factor of two higher at the NRDC stations than at NORESS for the same source moment. Since the noise levels in the two regions are nearly the same, this implies that the single-station magnitude thresholds for detecting P_n appear to be as much as 0.3 lower in eastern Kazakhstan than they are at NORESS.

(THIS PAGE INTENTIONALLY LEFT BLANK)

4. CONCLUSIONS

The overall goal of this work is to estimate the detection and location capability of actual and hypothetical networks of stations and arrays in and around the Soviet Union. These estimates require the simulation of the detection and location capability of the networks. This report summarizes two studies of important issues involved in the normalization of the simulations. The first is a theoretical study of the dependence of P_n geometric spreading on the velocity gradient in the upper mantle. This is important because most methods for estimating P_n attenuation require assumptions regarding geometric spreading. The second study is an empirical parameterization of regional wave spectra recorded near the eastern Kazakhstan nuclear explosion test site. The results are compared to results from a similar parameterization of data recorded by the NORESS array in Norway. Data recorded by the NORESS and ARCESS arrays are plentiful and provide an excellent basis for normalizing the simulations. Data recorded in eastern Kazakhstan are relatively few at this time, but can be used to see if the NORESS/ARCESS data can be used as a reasonable representation of conditions in this area.

The main conclusions of the first study are:

- P_n geometric spreading is extremely sensitive to the velocity gradient in the upper mantle. For example, the P_n amplitude at 1000 km for a model with the weak velocity gradient corresponding to the earth-flattening transformation of a homogeneous upper mantle is a factor of 20 larger than the P_n amplitude for a layer over a halfspace.
- P_n geometric spreading for an upper mantle model with a linear velocity gradient is frequency-dependent. The P_n waveform for a model with a weak velocity gradient is similar to an head wave at distances within a few hundred kilometers of the critical distance, but has the time dependence of a turning wave at longer ranges (the derivative of the head wave).
- Methods that assume frequency-independent P_n geometric spreading (e.g., spectral ratio methods) can lead to overestimates of upper mantle Q if the velocity in the upper mantle increases with depth.

These results have important implications for the interpretation of P_n amplitudes in terms of elastic and anelastic upper mantle structure and for practical issues related to regional seismic monitoring of nuclear explosion testing.

The parameterization of regional wave spectra used in the second study requires assumption of the geometric spreading. The P_n spectra recorded in eastern Kazakhstan are parameterized by a frequency-independent geometric spreading function with $r^{-1.3}$ distance dependence. This is the approximate distance dependence at 1 Hz between 300 and 1000 km for a homogeneous upper mantle (i.e., the gradient of the earth-

flattening transformation). Since the spreading is assumed to be independent of frequency, the $P_n Q(f)$ models include frequency-dependent effects associated with the velocity structure of the upper mantle and do not have a direct interpretation in terms of upper mantle anelasticity. However, a distinction between anelastic and geometric effects is not required to represent the distance dependence of spectra.

The main conclusions of the second study are:

- The attenuation of L_g spectra between 0.5 and 2.5 Hz in eastern Kazakhstan is nearly identical to the L_g attenuation in Scandinavia.
- The P_n spectra between 1 and 10 Hz in eastern Kazakhstan are similar in shape to the P_n spectra in Scandinavia at similar distances. However, the absolute levels appear to be as much as a factor of two higher in eastern Kazakhstan for fixed source moment (given that source moment is related to L_g magnitude).
- The average ambient noise spectrum at NORESS falls within one standard deviation of the average noise spectrum at the three NRDC stations.

It follows from the above conclusions that the magnitude thresholds for detecting P_n appear to be as much as 0.3 higher in Scandinavia than in eastern Kazakhstan. Since L_g propagation is nearly the same, the magnitude thresholds for detecting either P_n or L_g are less than 0.3 higher in Scandinavia than in eastern Kazakhstan. It is uncertain which of these P_n models more accurately describes the average attenuation in the Soviet Union, but the comparison gives a measure of the amount of regional variability that may be expected.

ACKNOWLEDGMENTS

Jeff Given provided much useful insight that improved the analysis of *Pn* geometric spreading and seismogram synthesis. I thank Thomas Bache for his careful review of the manuscript. I also thank Holly Given for her help in assembling the NRDC data set and for verifying the calibration data. Much of the data processing was done by Donna Williams at SAIC, and her contribution to the project is gratefully acknowledged. This research was funded by the Defense Advanced Research Projects Agency under Contract F08606-88-C-0033 and monitored by Air Force Technical Applications Center.

(THIS PAGE INTENTIONALLY LEFT BLANK)

REFERENCES

- Aki, K., and P. Richards, *Quantitative Seismology: Theory and Methods*, W. H. Freeman, San Francisco, Calif., 1980.
- Apsel, R., Dynamic Green's functions for layered media and applications to boundary-value problems, Ph.D. thesis, 349 pp., Univ. of Calif., San Diego, La Jolla, 1979.
- Bratt, S., T. Sereno, and T. Bache, Seismic monitoring of a low threshold Test Ban Treaty in the USSR, *EOS*, 68, 1364, 1987.
- Bungum, H., S. Vaage, and E. Husebye, The Meløy earthquake sequence, northern Norway; Source parameters and their moment scaling relations, *Bull. Seismol. Soc. Am.*, 72, 197-206, 1982.
- Burdick, L., and J. Orcutt, A comparison of the generalized ray and reflectivity methods of waveform synthesis, *Geophys. J. R. Astron. Soc.*, 58, 261-278, 1979.
- Burdick, L., C. Saikia, and N. Smith, P_n from the Nevada Test Site, *Semi-Annu. Tech. Rep. WWCP-R-88-03*, Woodward-Clyde Consultants, Pasadena, Calif., AFGL-TR-89-0034, 1988.
- Berger, J., H. Eissler, F. Vernon, I. Nersesov, M. Gokhberg, O. Stolyrov, and N. Tarasov, Studies of high-frequency seismic noise in Eastern Kazakhstan, *Bull. Seismol. Soc. Am.*, 78, 1744-1758, 1988.
- Chapman, C., and J. Orcutt, The computation of body wave synthetic seismograms in laterally homogeneous media, *Rev. of Geophysics*, 23, 105-163, 1985.
- Chun, K., Kokoski, R., and G. West, High-frequency P_n attenuation in the Canadian Shield, *Bull. Seismol. Soc. Am.*, 79, 1039-1053, 1989.
- Ciervo, A., S. Sanemitsu, D. Snead, R. Suey, and A. Watson, User's manual for SNAP/D: seismic network assessment program for detection, *Pacific-Sierra Research Corporation, Report 1027B*, 1985.
- Dwyer, J., R. Herrmann, and O. Nuttli, Spatial attenuation of the L_g wave in the central United States, *Bull. Seismol. Soc. Am.*, 73, 781-796, 1983.
- Evernden, J., C. Archambeau, and E. Cranswick, An evaluation of seismic decoupling and underground nuclear test monitoring using high-frequency seismic data, *Rev. Geophys.*, 24, 143-215, 1986.

- Given, H., N. Tarasov, V. Zhuravlev, F. Vernon, J. Berger, and I. Nersesov, High-frequency seismic observations in eastern Kazakhstan, USSR, with emphasis on chemical explosion experiments, *J. Geophys. Res.*, [accepted for publication], 1989.
- Hasegawa, H., *Lg* spectra of local earthquakes recorded by the Eastern Canada Telemetered Network and spectral scaling, *Bull. Seismol. Soc. Am.*, 73, 1041-1061, 1983.
- Henson, A., and T. Bache, Spectral characteristics of regional phases recorded at NORESS, *Bull. Seismol. Soc. Am.*, 78, 708-725, 1988.
- Herrmann, R., and A. Kijko, Modeling some empirical vertical component *Lg* relations, *Bull. Seismol. Soc. Am.*, 73, 157-171, 1983.
- Hill, D., Velocity gradients and anelasticity from crustal body wave amplitudes, *J. Geophys. Res.*, 76, 3309-3325, 1972.
- Kennett, B., On regional S, *Bull. Seismol. Soc. Am.*, 75, 1077-1086, 1985.
- King, D., and G. Calcagnile, *P*-wave velocities in the upper mantle beneath Fennoscandia and Western Russia, *Geophys. J. R. Astron. Soc.*, 46, 407-432, 1976.
- Menke, W., and P. Richards, Crust-Mantle whispering gallery phases: a deterministic model of teleseismic *Pn* wave propagation, *J. Geophys. Res.*, 85, 5416-5422, 1980.
- Sereno, T., and S. Bratt, Attenuation and detection capability of regional phases recorded at NORESS, *Semiannu. Tech. Rep. SAIC 88/1598*, Sci. Appl. Int. Corp., San Diego, Calif., 1988.
- Sereno, T., and S. Bratt, Seismic detection capability at NORESS and implications for the detection threshold of a hypothetical network in the Soviet Union, *J. Geophys. Res.*, 94, 10397-10414, 1989.
- Sereno, T., S. Bratt, and T. Bache, Simultaneous inversion of regional wave spectra for attenuation and seismic moment in Scandinavia, *J. Geophys. Res.*, 93, 2019-2035, 1988.
- Shin, T.-C., and R. Herrmann, *Lg* attenuation and source studies using 1982 Miramichi data, *Bull. Seismol. Soc. Am.*, 77, 384-397, 1987.
- Somerville, P., J. McLaren, L. LeFevre, R. Burger, and D. Helmberger, Comparison of source scaling relations of eastern and western North American earthquakes, *Bull.*

Seismol. Soc. Am., 77, 322-346, 1987.

Street, R., R. Herrmann, and O. Nuttli, Spectral characteristics of the *Lg* wave generated by central United States earthquakes, *Geophys. J. R. Astron. Soc.*, 41, 51-63, 1975.

Thurber, C., H. Given, and J. Berger, Regional seismic event location with a sparse network: application to eastern Kazakhstan, USSR, *J. Geophys. Res.*, [submitted], 1989.

Veith, K., and G. Clawson, Magnitude from short-period *P* wave data, *Bull. Seismol. Soc. Am.*, 62, 435-452, 1972.

(THIS PAGE INTENTIONALLY LEFT BLANK)

APPENDIX A: NRDC WAVEFORMS

This appendix plots the waveform data for all events used in the regional wave attenuation study in eastern Kazakhstan described in Section 3 of this report. The station identification and epicentral distance are listed in the upper right corner of each plot. Only vertical-component recordings from the borehole sensor at each station are plotted. The seismograms are filtered between 0.5 and 20 Hz. The amplitudes are converted to nanometers from digital counts using calibration values at 1 Hz obtained from the Center for Seismic Studies (these calibration values are listed in each figure caption). Note that these are only approximate amplitudes since the instrument response (flat to velocity between 0.2 and 100 Hz) has not been deconvolved. *Pn* and *Lg* phases are marked in each figure with a vertical line.

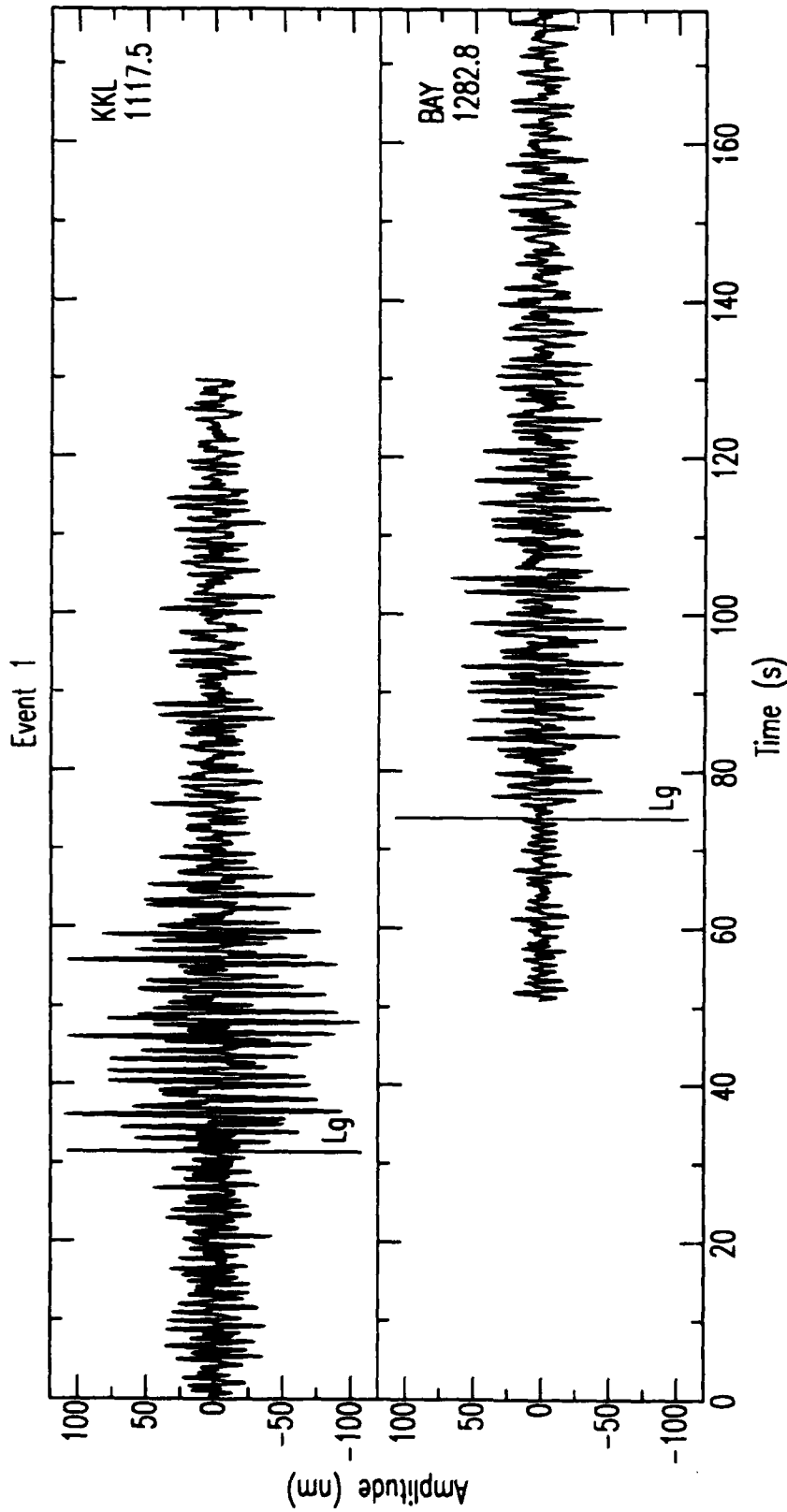


Figure A.1. Waveforms for Event 1 (Table 3.2). This is an m_b 4.3 earthquake reported in the PDE Bulletin. The calibration values are 0.012781 and 0.012929 nanometers per digital count for stations KKL and BAY, respectively.

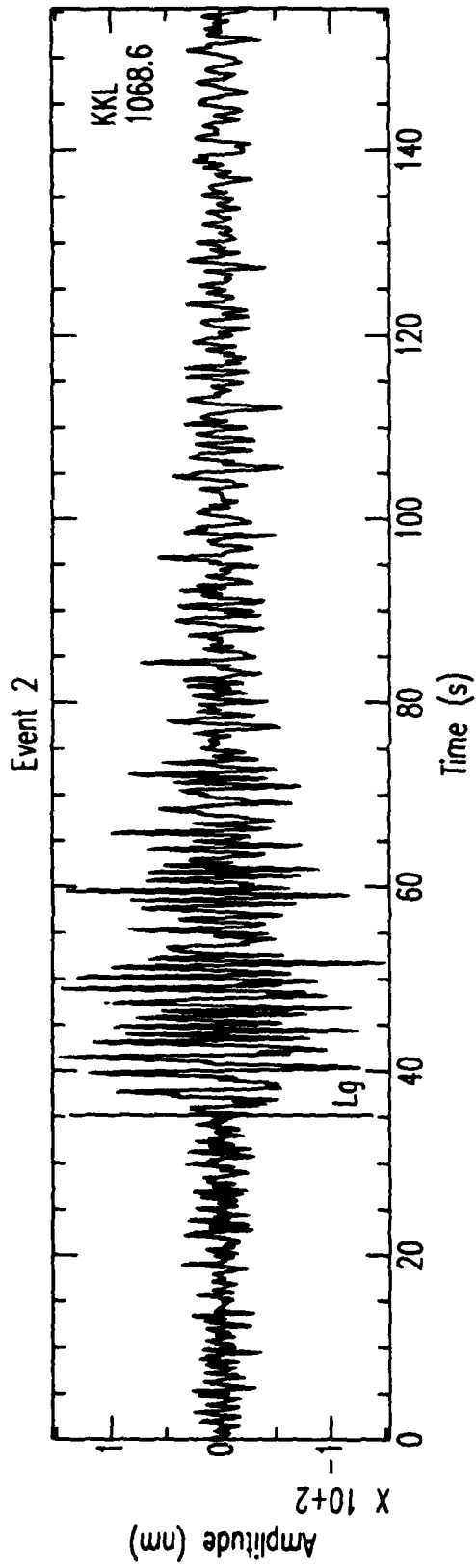


Figure A.2. Waveform for Event 2 (Table 3.2). This is an m_b 4.3 earthquake reported in the PDE Bulletin. The calibration value is 0.012929 nanometers per digital count for station KKL.

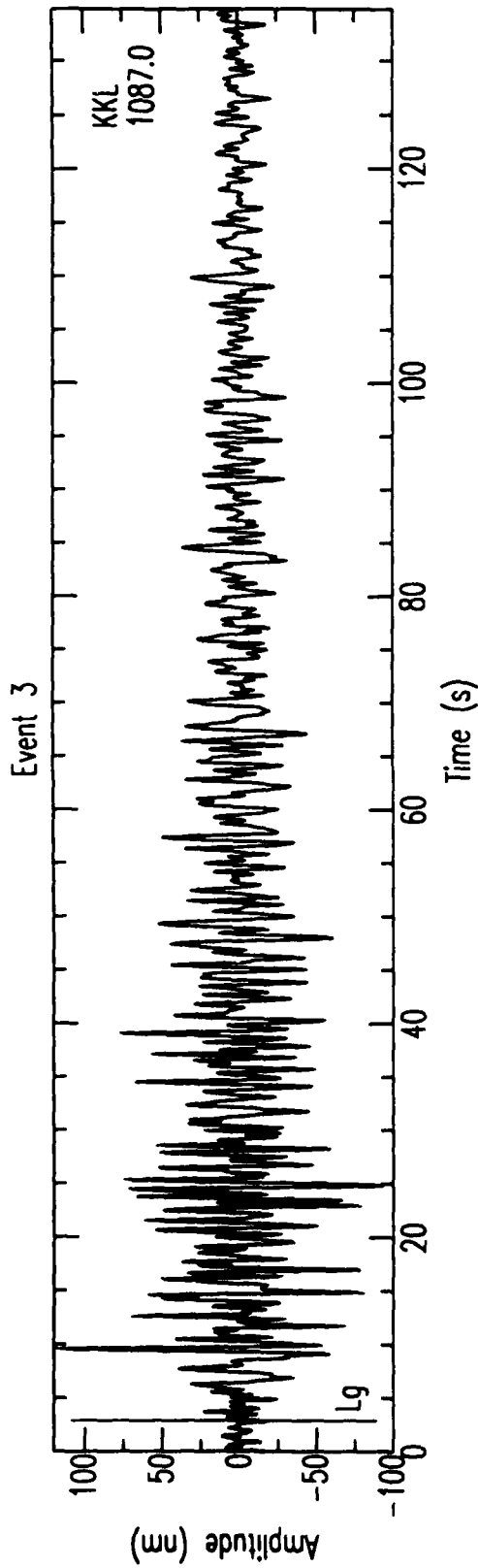


Figure A.3. Waveform for Event 3 (Table 3.2). This is an m_b 4.6 earthquake reported in the PDE Bulletin. The calibration value is 0.012929 nanometers per digital count for station KKL.

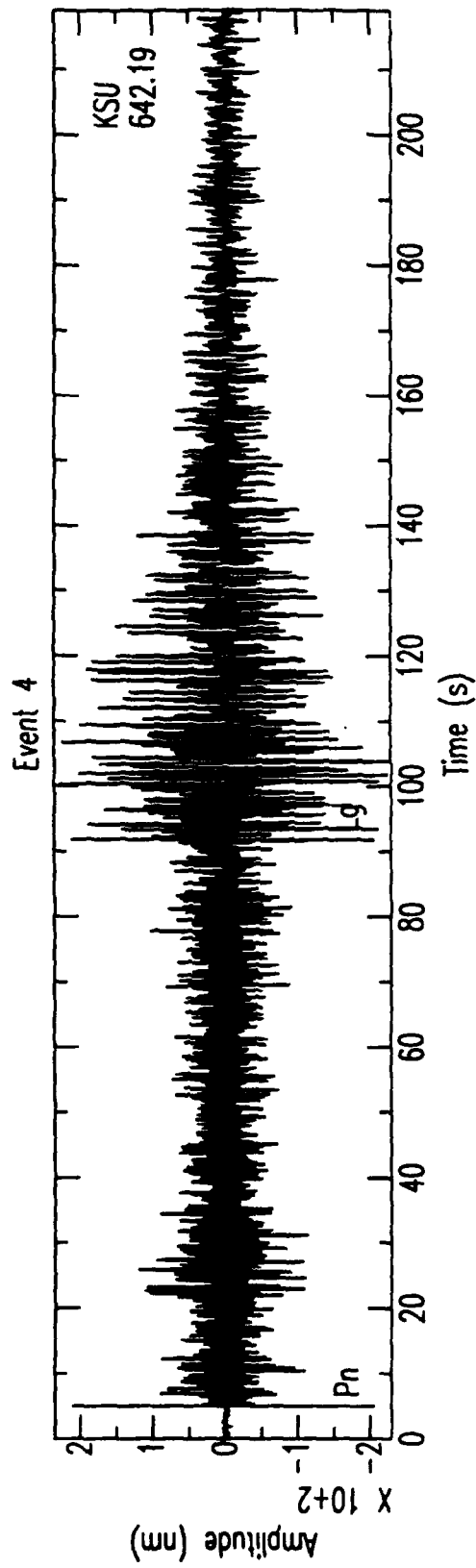


Figure A.4. Waveform for Event 4 (Table 3.2). The event type is unknown. The calibration value is 0.012929 nanometers per digital count for station KSU.

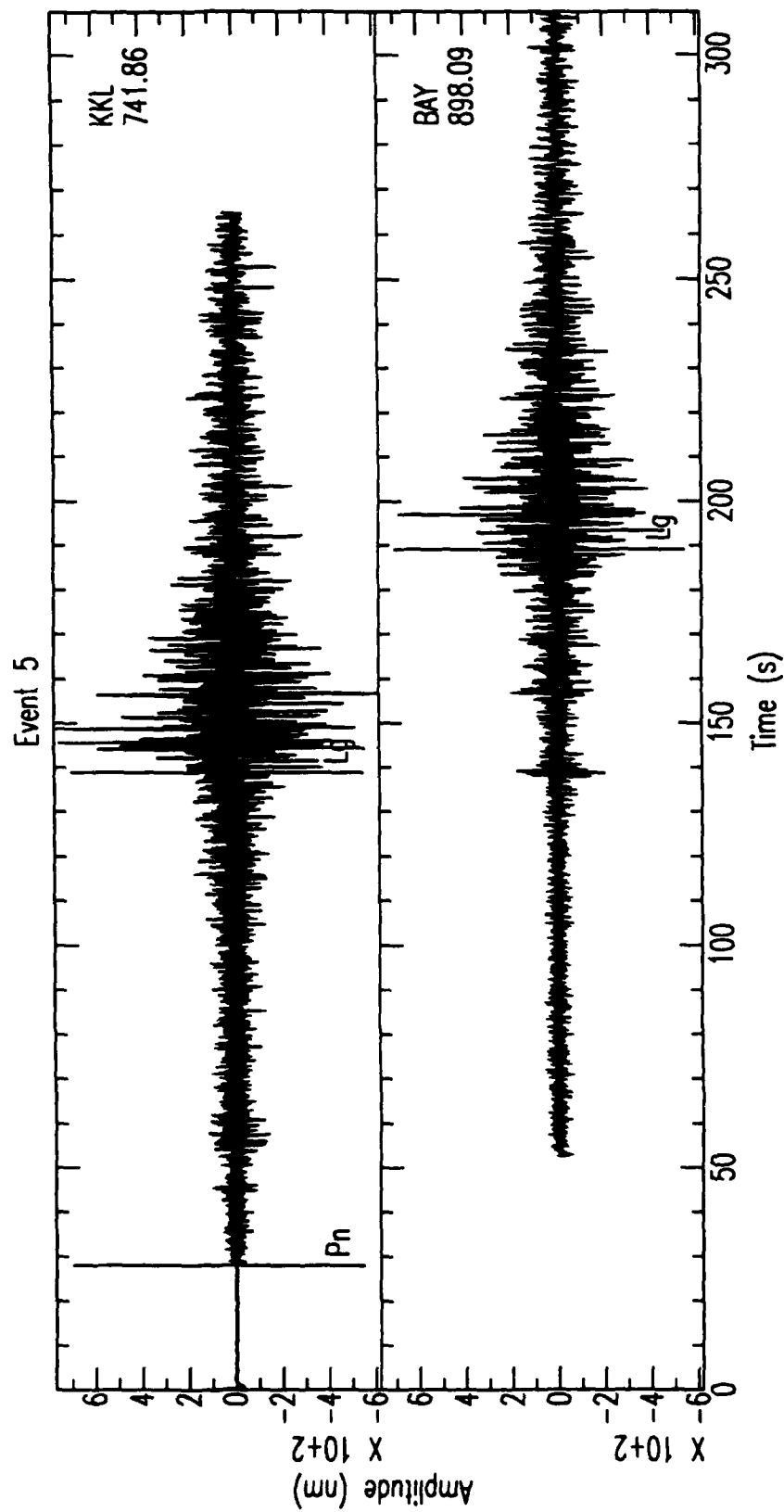


Figure A.5. Waveforms for Event 5 (Table 3.2). This is an m_b 4.6 earthquake reported in the PDE Bulletin. The calibration values are 0.411528 and 1.638321 nanometers per digital count for stations KKL and BAY, respectively.

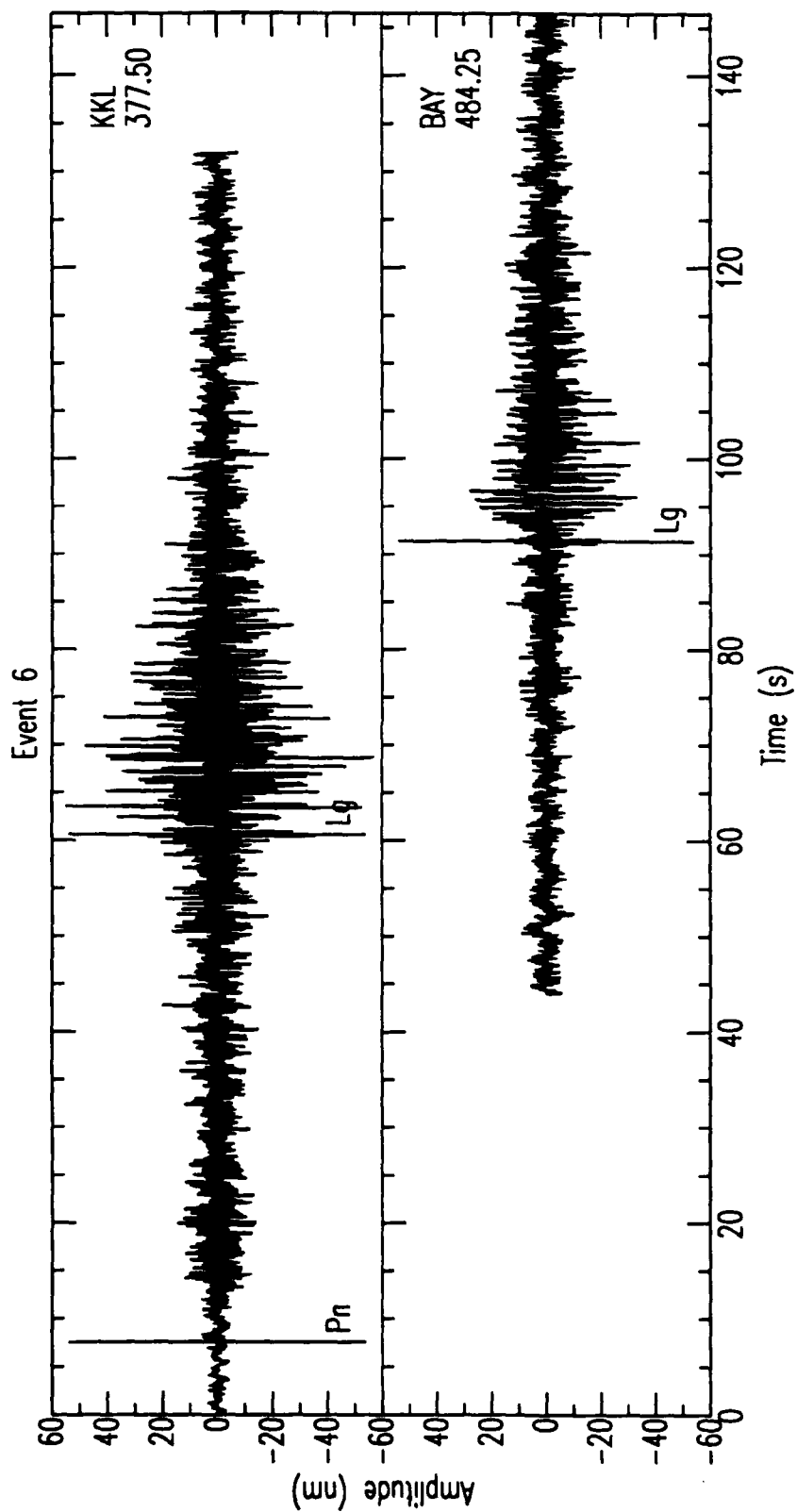


Figure A.6. Waveforms for Event 6 (Table 3.2). The event type is unknown. The calibration values are 0.012781 and 0.012929 nanometers per digital count for stations KKL and BAY, respectively.

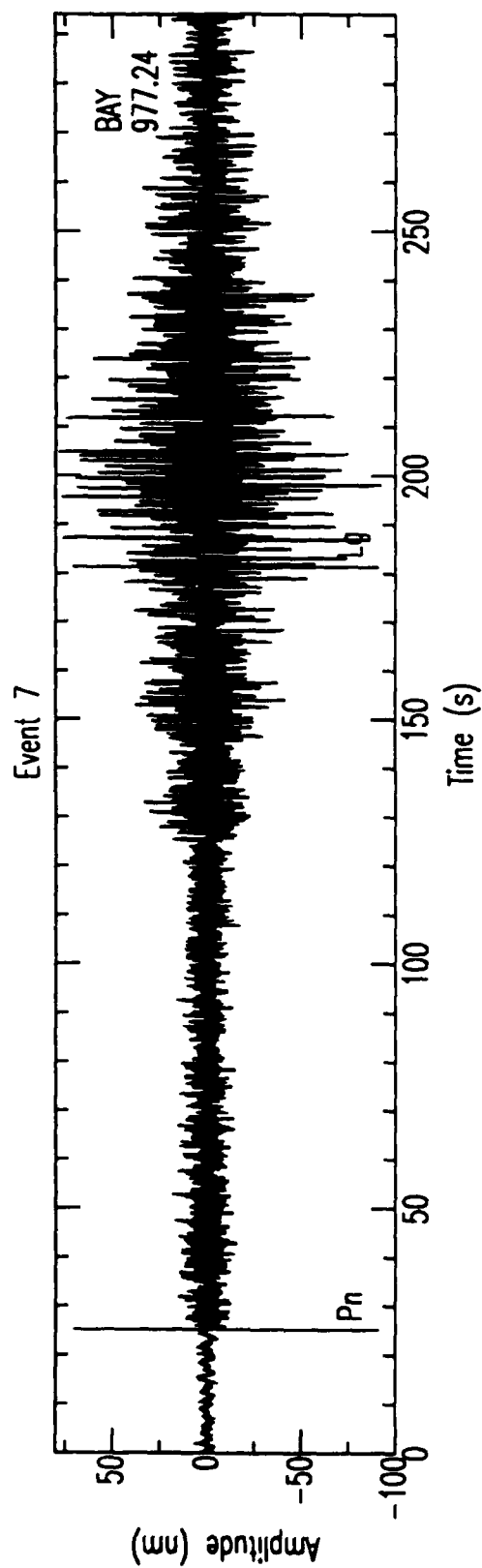


Figure A.7. Waveform for Event 7 (Table 3.2). This is probably an earthquake but was not reported in the PDE Bulletin. The calibration value is 0.012929 nanometers per digital count for station BAY.

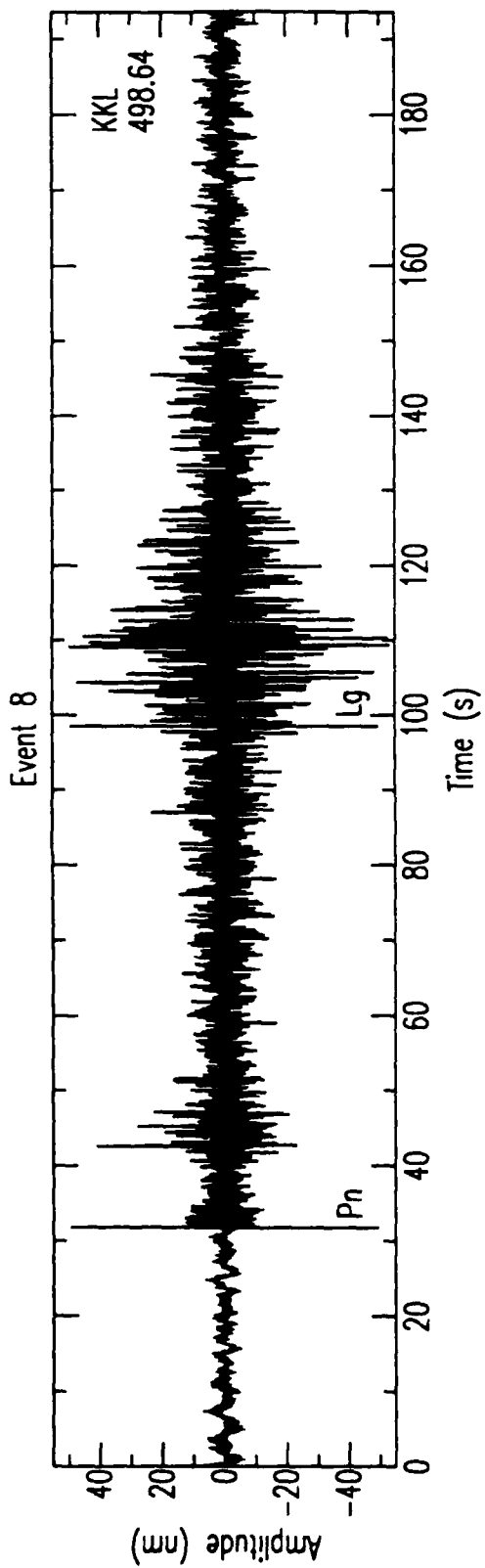


Figure A.8. Waveform for Event 8 (Table 3.2). The event type is unknown. The calibration value is 0.006406 nanometers per digital count for station KKL.

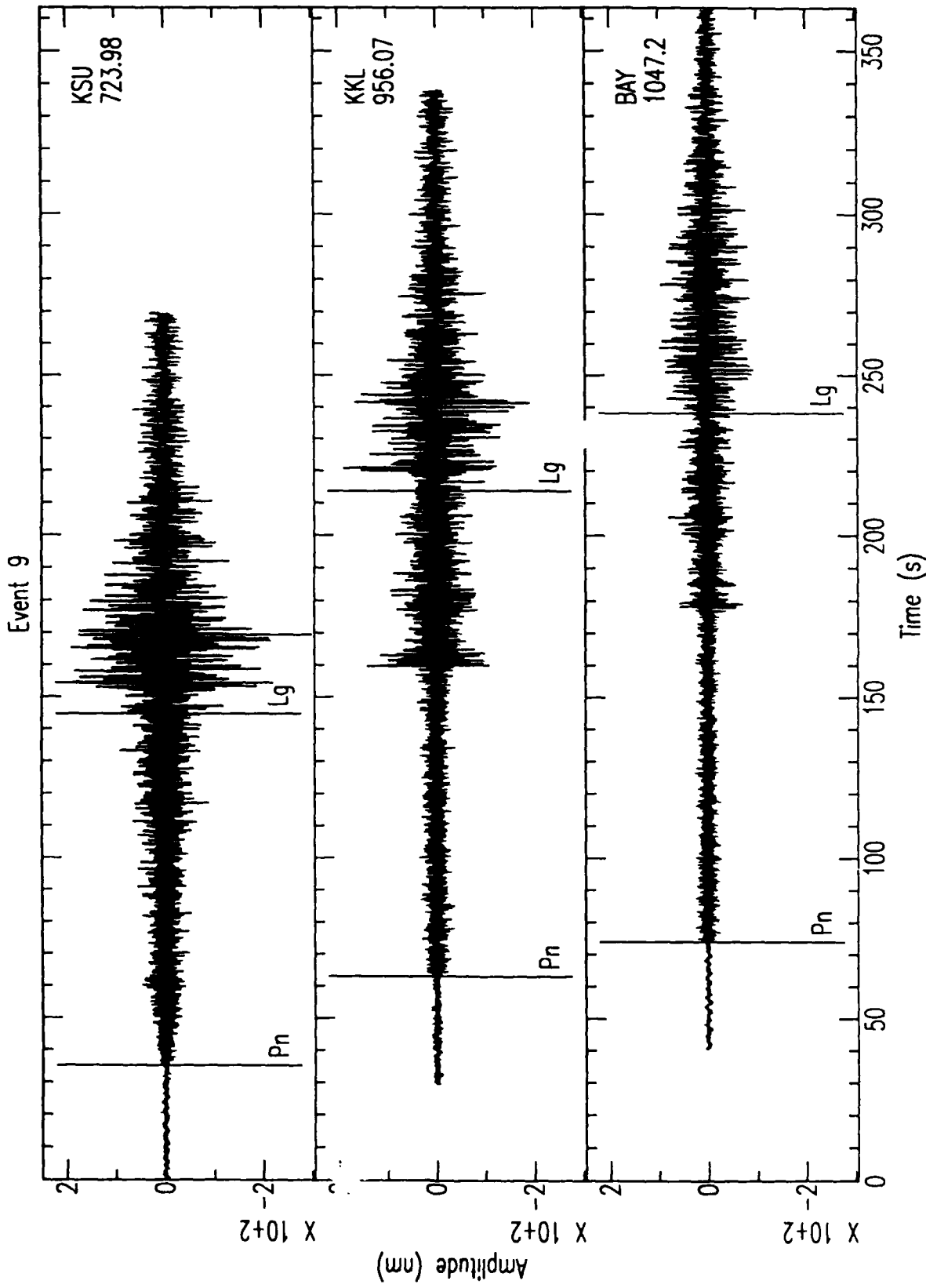


Figure A.9. Waveforms for Event 9 (Table 3.2). This is an m_b 4.4 earthquake reported in the PDE Bulletin. Note the exceptionally strong S_n at KKL and BAY. The calibration value is 0.006406 nanometers per digital count for all three stations.

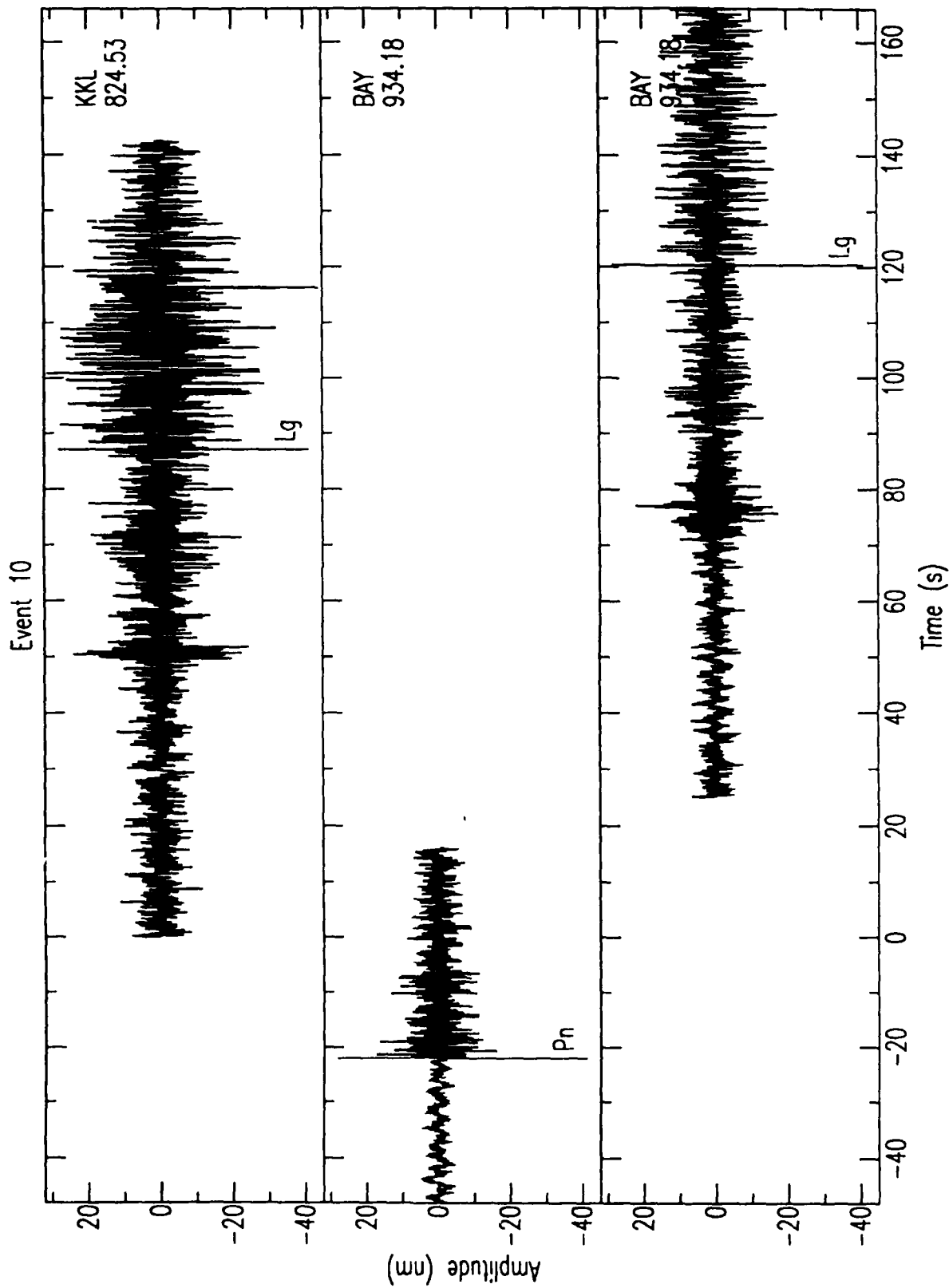


Figure A.10. Waveforms for Event 10 (Table 3.2). This is probably an earthquake but was not reported in the PDE Bulletin. The magnitude of this event is approximately 3.3. The data recorded at Bayanaul are plotted in two panels because there is a data gap near 20 s. Note the strong S_n phase at both stations. The calibration value is 0.006406 nanometers per digital count for both stations.

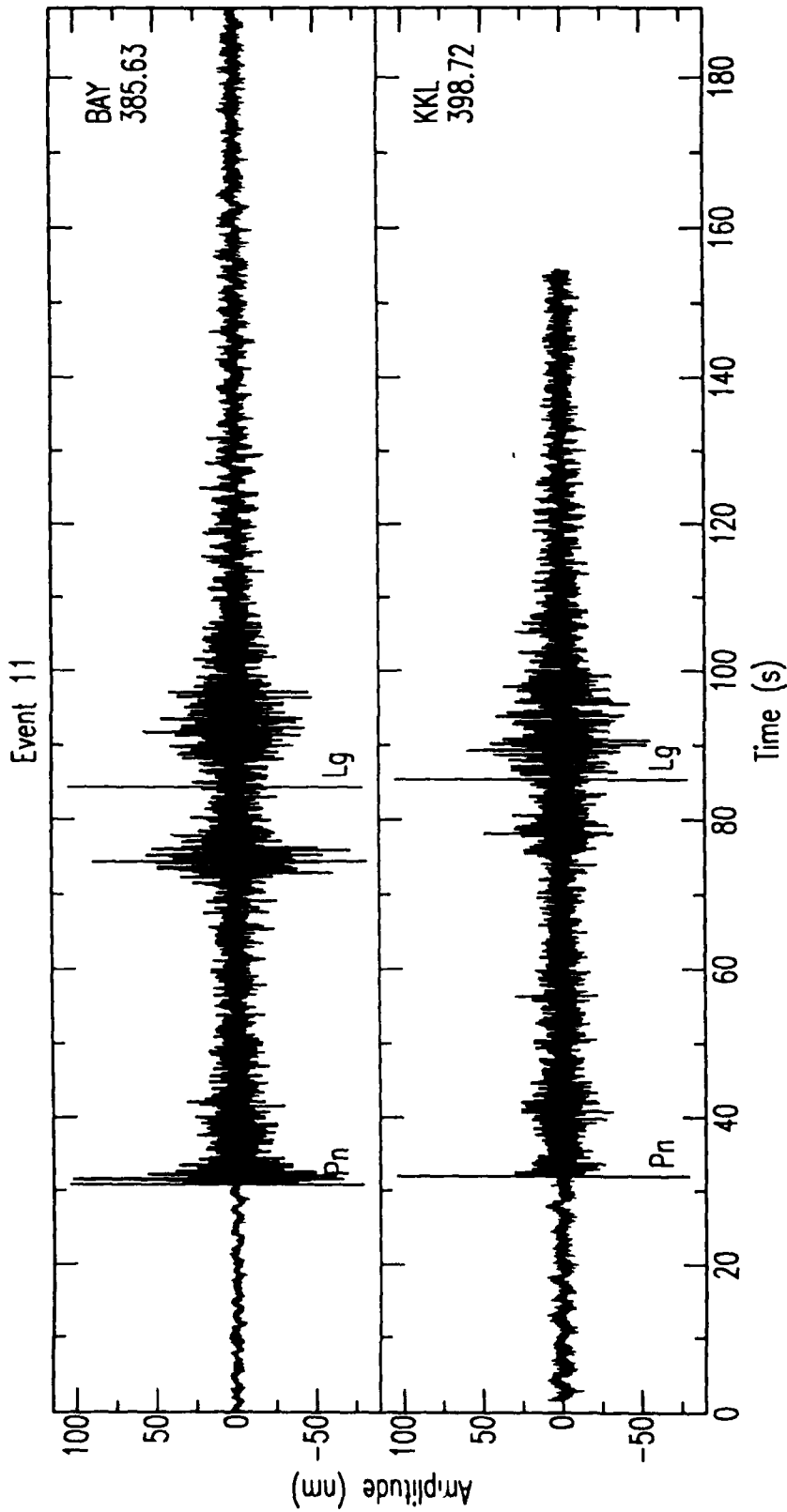


Figure A.11. Waveforms for Event 11 (Table 3.2). This is probably an explosion. The Lg magnitude is approximately 2.6. Note the small Lg/Pn ratio for this event. The calibration value is 0.006406 nanometers per digital count for both stations.

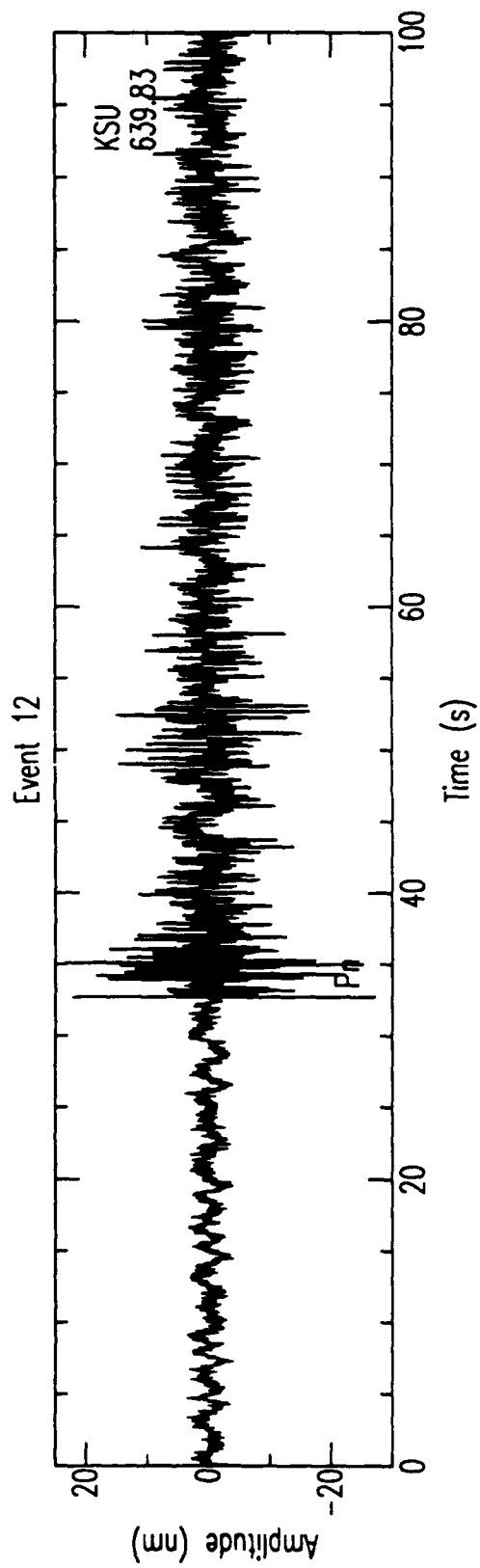


Figure A.12. Waveform for Event 12 (Table 3.2). The event type is unknown. The calibration value is 0.006406 nanometers per digital count for KSU.

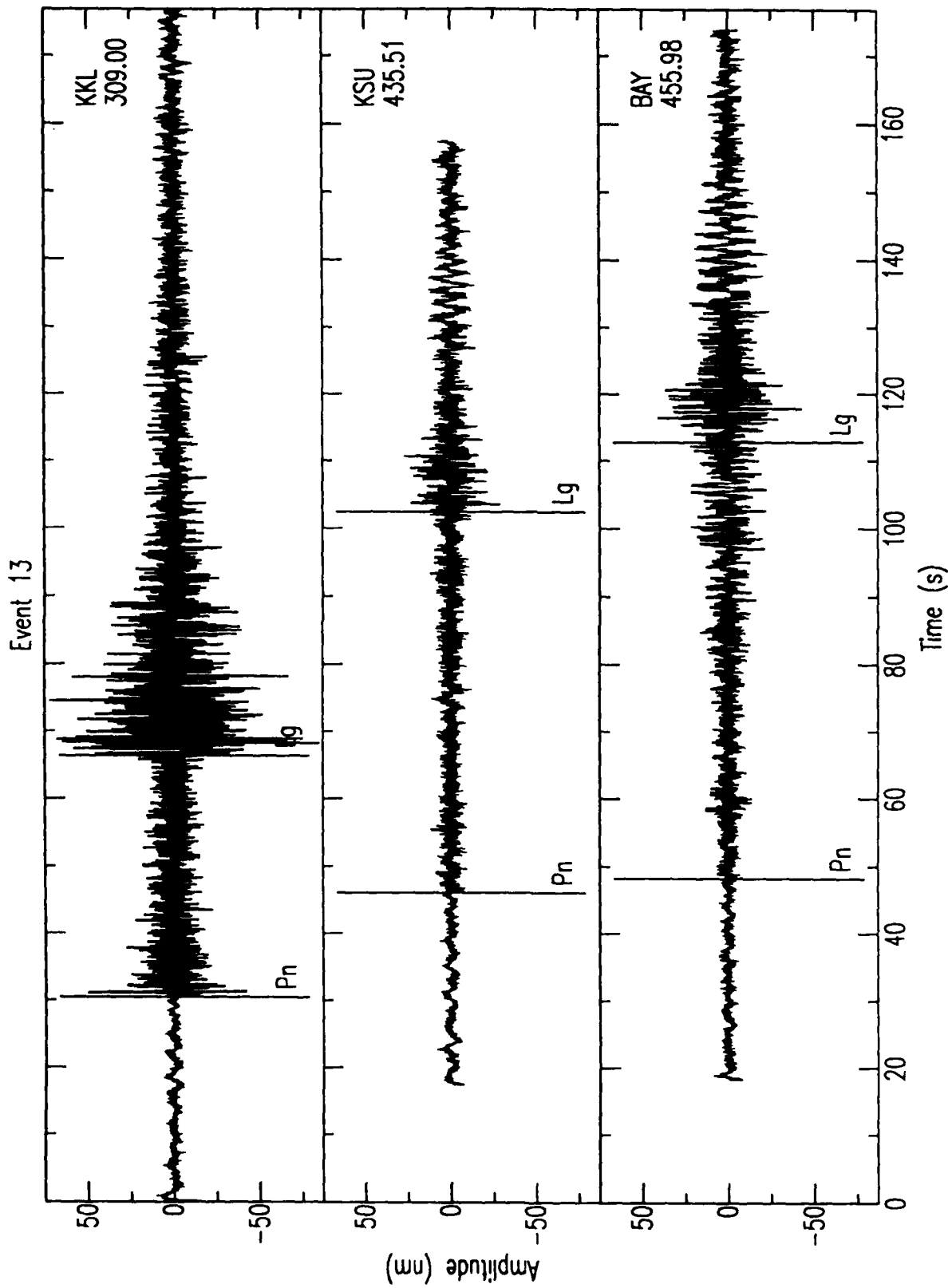


Figure A.13. Waveforms for Event 13 (Table 3.2). This is an explosion in the Lake Balkash area [Thurber *et al.*, 1989]. Note the presence of a strong *Rg* phase at stations KSU and BAY. The *Lg* magnitude of this event is approximately 2.5. The calibration value is 0.006406 nanometers per digital count at all three stations.

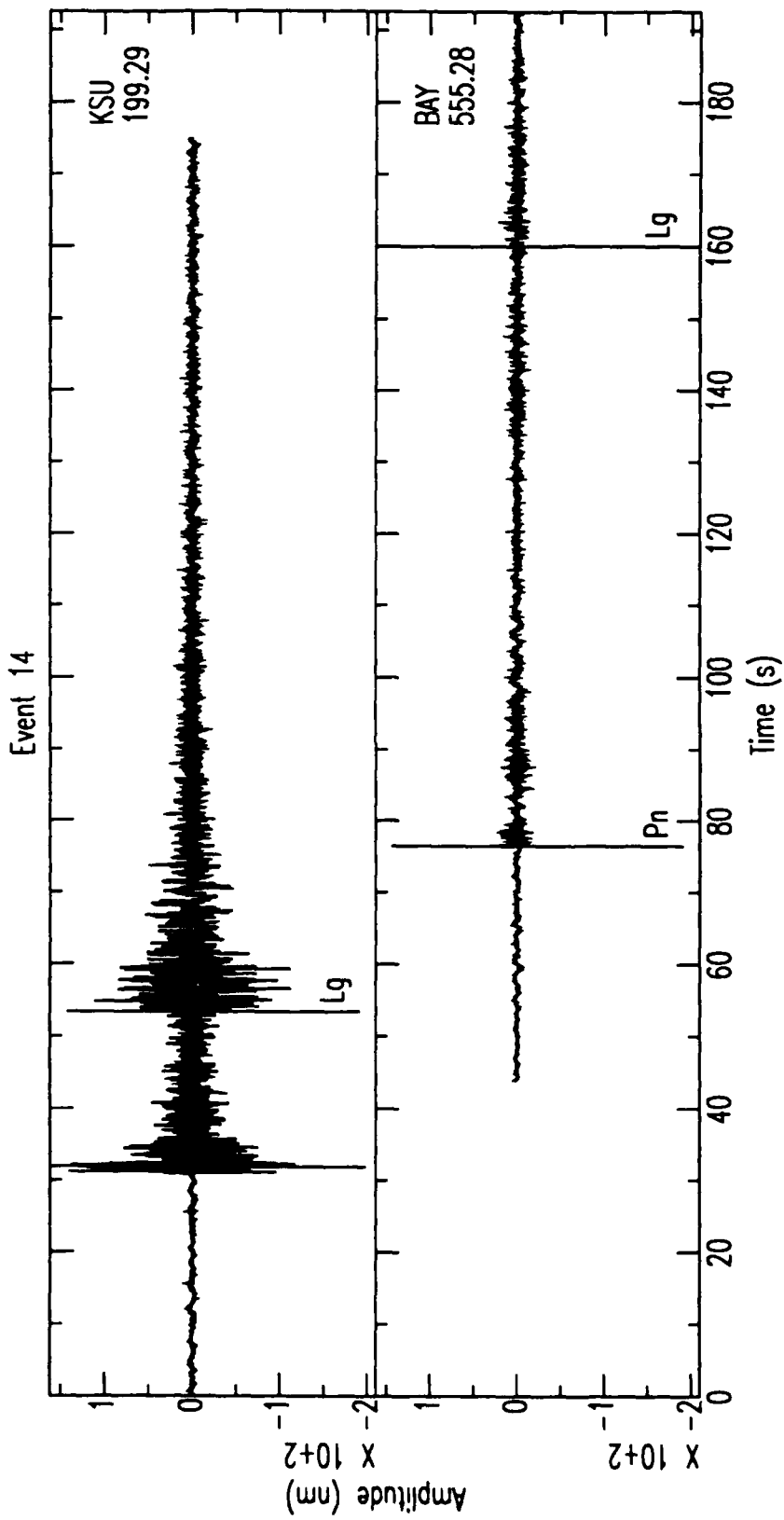


Figure A.14. Waveforms for Event 14 (Table 3.2). This is probably an explosion. The Lg magnitude of this event is approximately 2.3. The calibration value is 0.006406 nanometers per digital count at both stations.

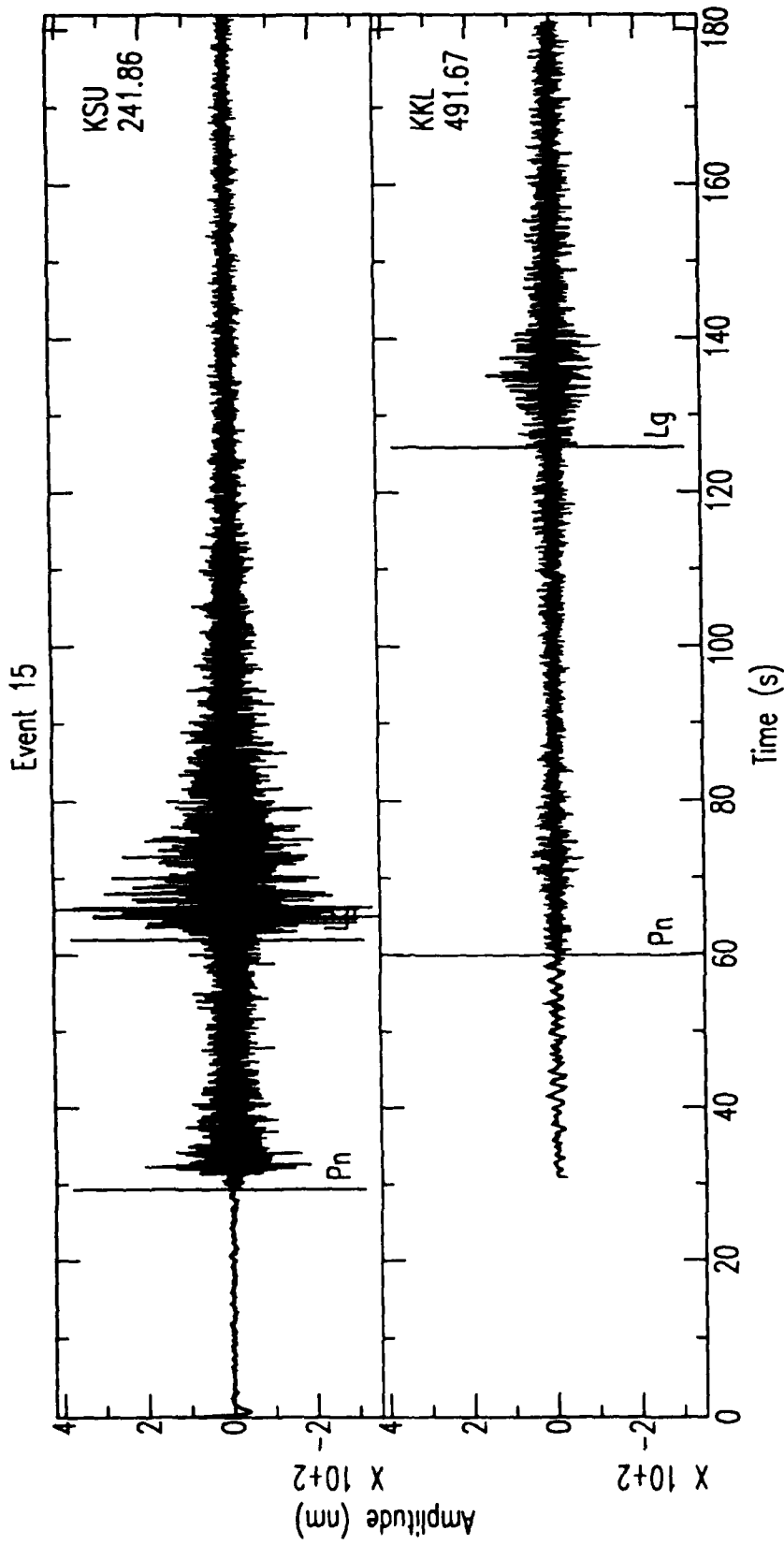


Figure A.15. Waveforms for Event 15 (Table 3.2). The event type is unknown. The calibration values are 1.638321 and 0.006406 nanometers per digital count for stations KSU and KKL, respectively.

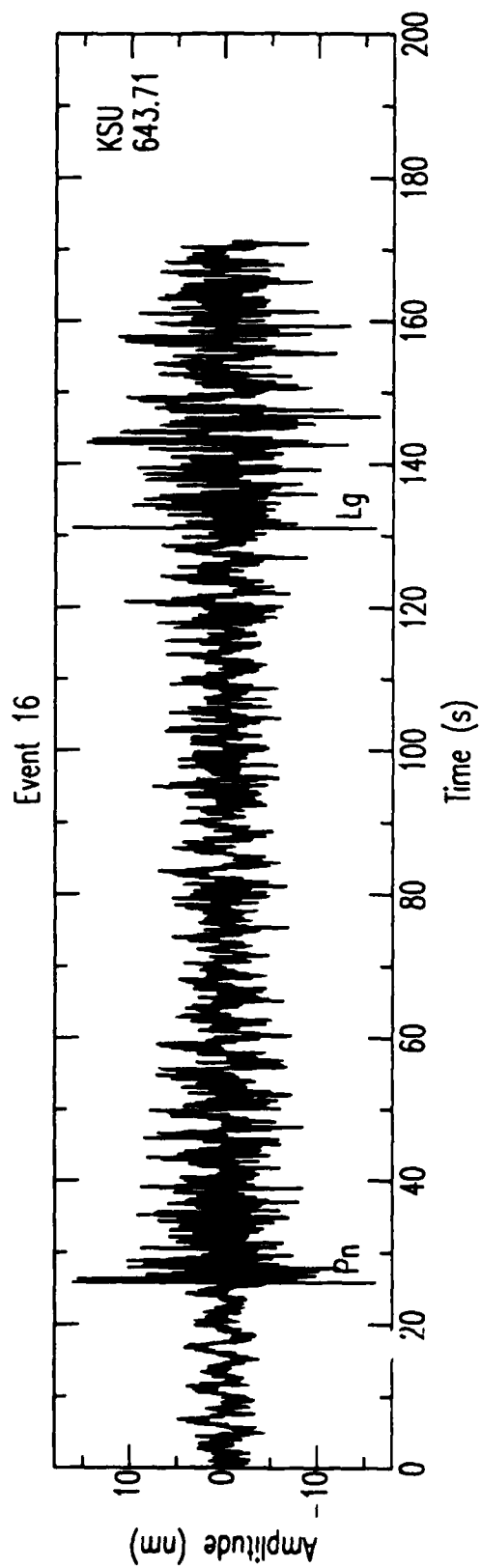


Figure A.16. Waveform for Event 16 (Table 3.2). The event is probably an explosion. The L_g magnitude for this event is approximately 2.6. The calibration value is 0.006406 nanometers per digital count for station KSU.

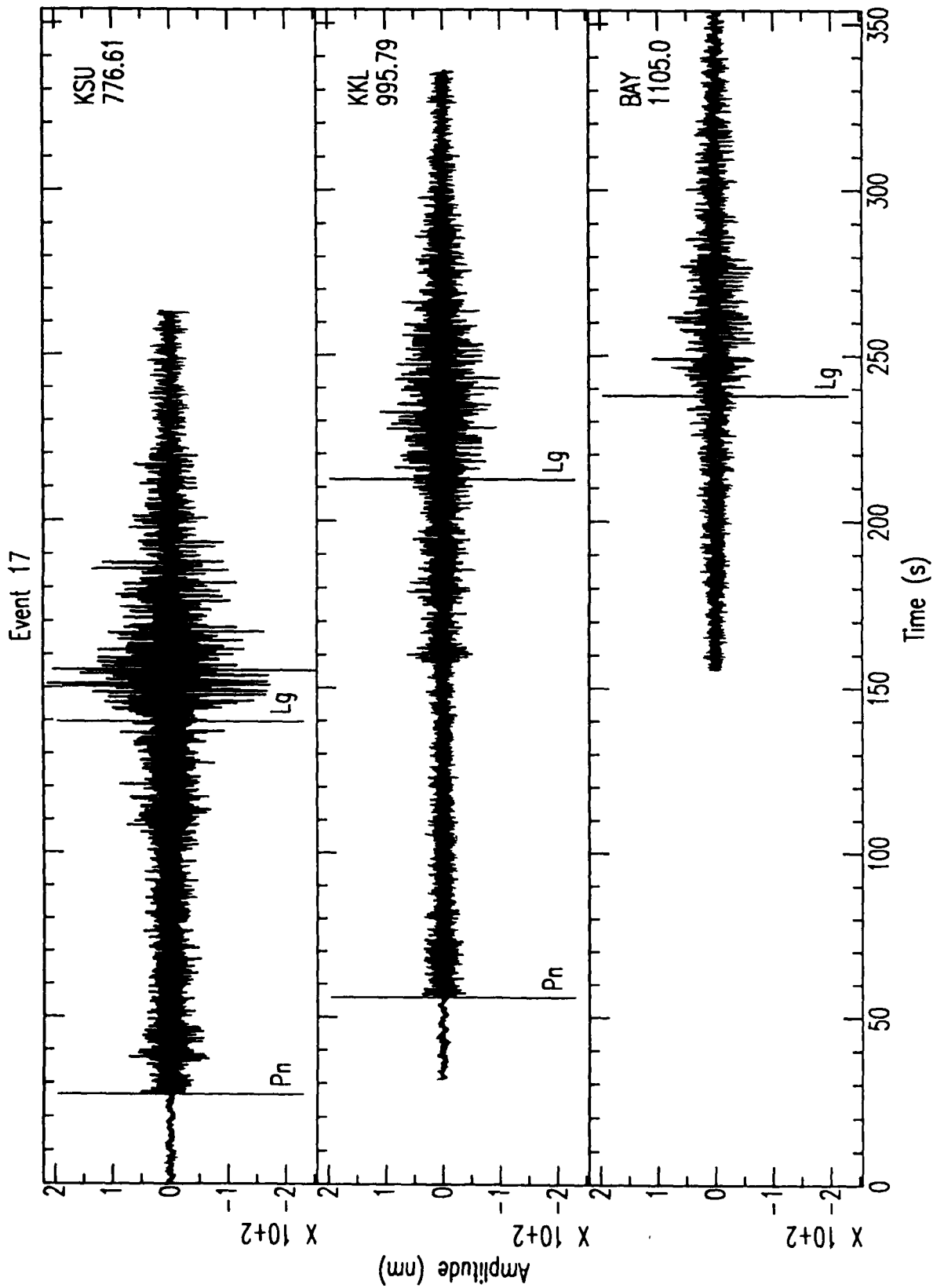


Figure A.17. Waveforms for Event 17 (Table 3.2). This event is an earthquake in the Tien Shan area [Thurber *et al.*, 1989]. The calibration value is 0.006406 nanometers per digital count for all three stations.

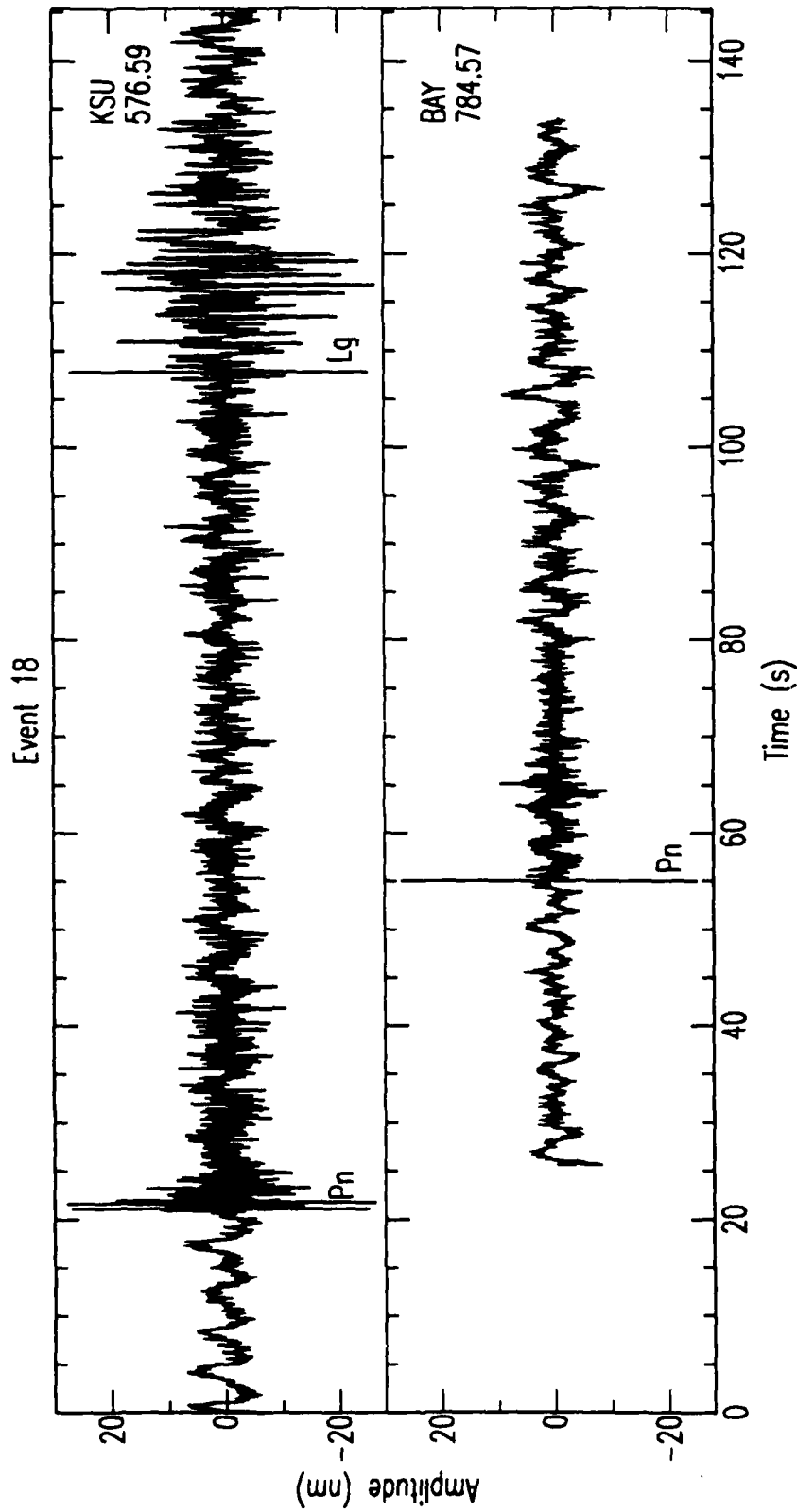


Figure A.18. Waveforms for Event 18 (Table 3.2). This event is probably an explosion. The L_g magnitude is approximately 2.5. The calibration value is 0.006406 nanometers per digital count for both stations.

Event 19

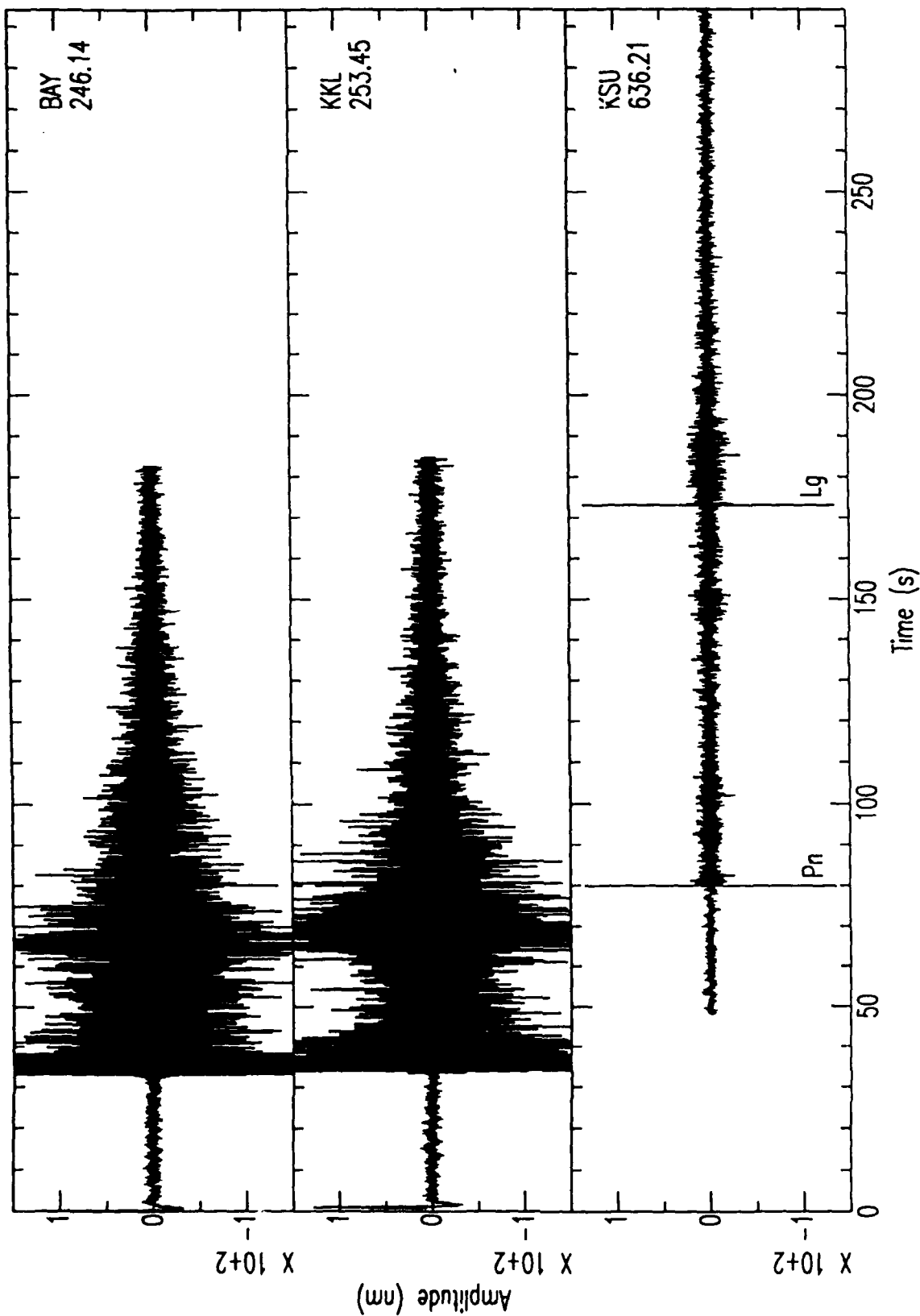


Figure A.19. Waveforms for Event 19 (Table 3.2). This event is a 10-ton calibration explosion [Thurber *et al.*, 1989; Given *et al.*, 1989]. The vertical scale is adjusted for the waveform at KSU (the data at BAY and KKL are not clipped). The L_g magnitude for this event is approximately 2.9. The calibration value for station KSU is 0.006406 nanometers per digital count and it is 1.638321 for stations BAY and KKL.

Event 20

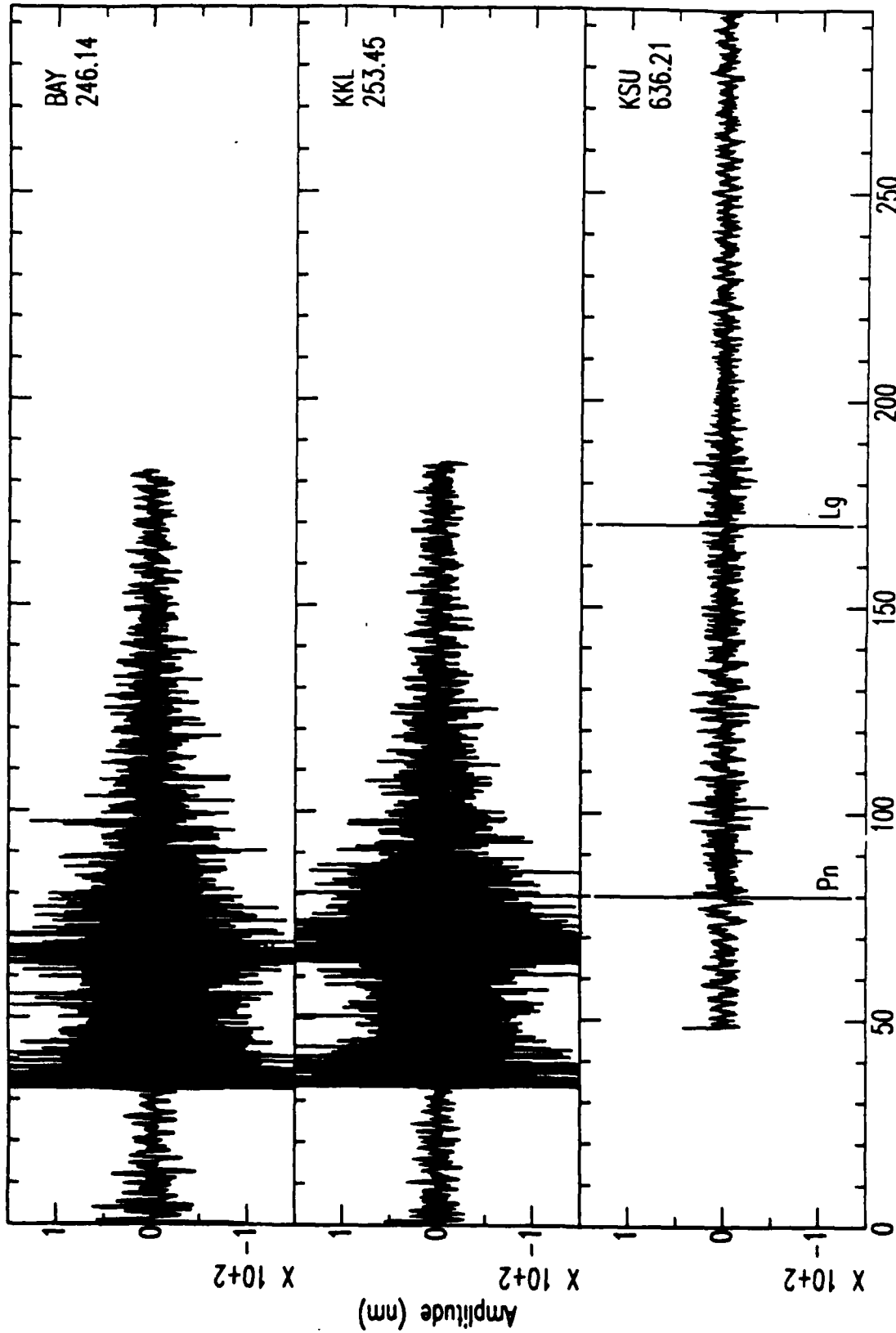


Figure A.20. Waveforms for Event 20 (Table 3.2). This event is a 10-ton calibration explosion [Thurber *et al.*, 1989; Given *et al.*, 1989]. The vertical scale is adjusted for the waveform at KSU (the data at BAY and KKL are not clipped). The L_g magnitude for this event is approximately 2.9. The calibration values are 0.050629, 0.102188, and 1.638321 nanometers per digital count for stations BAY, KKL, and KSU, respec-

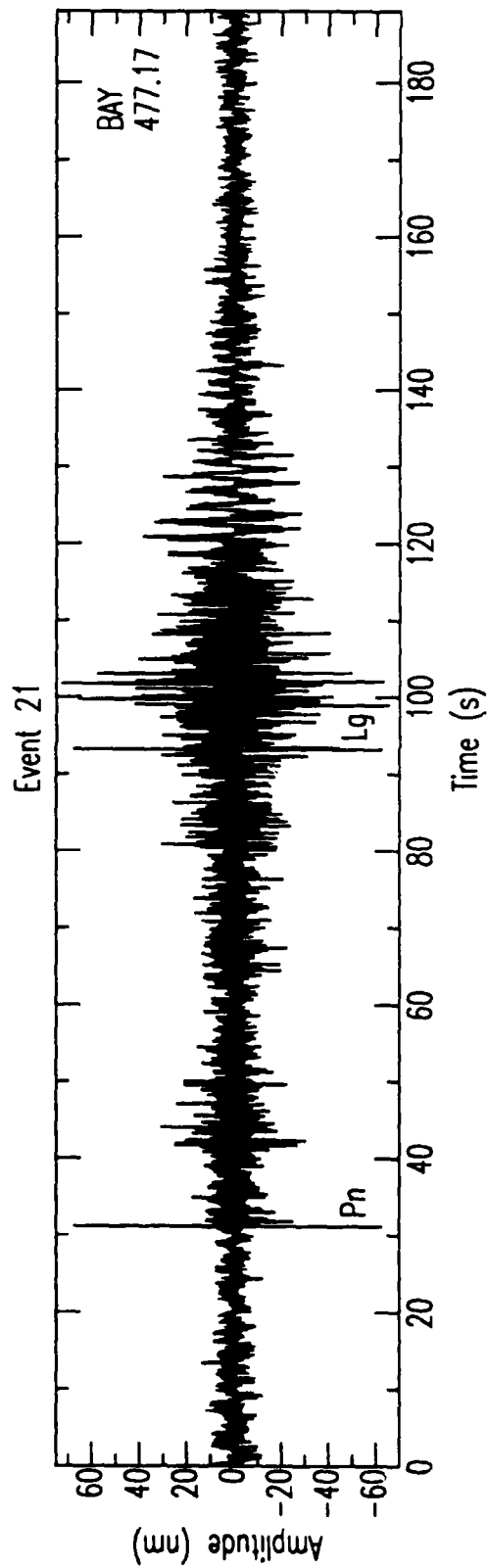


Figure A.21. Waveforms for Event 21 (Table 3.2). This event is an explosion in the Lake Balkash area (compare to Event 13). Note the strong *Rg* phase. The *Lg* magnitude for this event is approximately 2.9. The calibration value is 0.012929 nanometers per digital count for station BAY.

APPENDIX B: NRDC SPECTRA AND INVERSION RESULTS

Regional P_n and L_g spectra from 21 events (Table 3.2) were inverted for $Q(f)$, long-period source level (S_0), and a scaling parameter (c) that relates corner frequency and S_0 for all events in the data set. Earthquake moment is related to $L_g S_0$ by (3.5) and explosion moment is related to $P_n S_0$ by (3.6). The geometric spreading was modeled as (3.7) with $r_0 = 100$ km and $m = 1/2$ for L_g and $r_0 = 1$ km and $m = 1.3$ for P_n . The path result for L_g between 0.5 and 2.5 Hz is $Q(f) = 650$. The P_n inversion between 1 and 10 Hz produced a range of $Q(f)$ and source models that fit the observed data with nearly equal fidelity. The range of attenuation models is approximately $Q(f) = 1175$ to $Q(f) = 300f^{0.5}$.

Table B.1 lists the source parameters for the model with $P_n Q(f) = 1175$. The m_b are from the PDE Bulletin. The M_L were calculated from the L_g amplitude and the NORESS correction table. Table B.2 lists the source parameters for the model with $P_n Q(f) = 300f^{0.5}$. Table B.3 lists the source parameters derived from the L_g inversion. Note that corner frequency is not a parameter of the inversion for each event, but is calculated from the long-period level and the scaling parameter. Since the L_g inversion only included frequencies less than 2.5 Hz, corner frequency is constrained only by a small number of large events.

Figures B.1–B.21 display theoretical and data spectra for all of the events used in the inversion. The theoretical spectra are computed using (3.4) with the inversion results for $Q(f)$ and $S(f)$. Two theoretical spectra are plotted for each P_n observation corresponding to the models in Tables B.1 and B.2. The more coarsely dashed of the two curves corresponds to the model in Table B.2 ($Q(f) = 300f^{0.5}$). The lowest curve in each P_n plot is the ambient noise spectrum calculated from a 5-s window starting 5.5 s before P_n . The theoretical L_g spectra are calculated from the parameters in Table B.3. The lowest curve is the pre- L_g noise spectrum calculated from a 5-s window starting 5.5 s before L_g . The P_n and L_g noise spectra are scaled to the signal window length using (3.1). The P_n spectra are plotted from 0.5 to 20 Hz and the L_g spectra are plotted from 0.5 to 5.0 Hz. The spectra are ordered for each event with data from the closest station plotted at the top of each figure. The P_n spectra are plotted on the left and the L_g spectra are plotted on the right.

Table B.1 P_n Inversion Results ($Q(f) = 1175$)

Event	m_b	M_L	Type	Station	Distance (km)	S_0 ($\text{cm}^2\text{-s}$)	f_c (Hz)
1	4.3		EQ				
2	4.3		EQ				
3	4.6		EQ				
4				KSU	642	810.5	3.2
5	4.6		EQ	KKL	742	391.5	4.0
6				KKL	378	9.6	13.9
7			EQ	BAY	977	268.3	4.6
8				KKL	499	41.0	8.6
9	4.4		EQ	BAY	1047	335.3	4.2
				KKL	956	516.3	3.7
				KSU	724	162.2	5.4
10			EQ	BAY	934	296.4	4.4
11		2.6	EX	BAY	386	103.2	6.3
				KKL	399	47.8	8.1
12				KSU	640	108.0	6.2
13		2.5	EX	BAY	456	19.9	10.9
				KKL	309	31.8	9.3
				KSU	436	16.8	11.5
14		2.3	EX	BAY	555	34.6	9.1
15				KKL	492	107.0	6.2
				KSU	242	10.9	13.3
16		2.6	EX	KSU	644	59.8	7.5
17			EQ	KKL	996	1042.6	2.9
				KSU	777	548.8	3.6
18		2.5	EX	BAY	785	57.3	7.7
				KSU	577	64.4	7.4
19		2.9	EX	KSU	636	116.4	6.0
20		2.9	EX	KSU	636	150.4	5.5
21		2.9	EX	BAY	477	54.3	7.8

Table B.2 Pn Inversion Results ($Q(f) = 300f^{0.5}$)

Event	m_b	M_L	Type	Station	Distance (km)	S_0 ($\text{cm}^2\text{-s}$)	f_c (Hz)
1	4.3		EQ				
2	4.3		EQ				
3	4.6		EQ				
4				KSU	642	1686.0	3.4
5	4.6		EQ	KKL	742	947.5	4.1
6				KKL	378	15.6	16.0
7			EQ	BAY	977	913.3	4.1
8				KKL	499	74.6	9.5
9	4.4		EQ	BAY	1047	1260.4	3.7
				KKL	956	1755.1	3.3
				KSU	724	388.5	5.5
10			EQ	BAY	934	956.1	4.1
11		2.6	EX	BAY	386	161.8	7.3
				KKL	399	77.8	9.4
12				KSU	640	230.7	6.5
13		2.5	EX	BAY	456	35.3	12.2
				KKL	309	45.9	11.2
				KSU	436	29.3	13.0
14		2.3	EX	BAY	555	67.7	9.8
15				KKL	492	193.8	6.9
				KSU	242	15.2	16.2
16		2.6	EX	KSU	644	126.3	8.0
17			EQ	KKL	996	3824.7	2.6
				KSU	777	1426.8	3.6
18		2.5	EX	BAY	785	146.3	7.6
				KSU	577	127.2	8.0
19		2.9	EX	KSU	636	253.4	6.3
20		2.9	EX	KSU	636	321.7	5.8
21		2.9	EX	BAY	477	96.7	8.7

Table B.3 L_g Inversion Results ($Q(f) = 650$)

Event	m_b	M_L	Type	Station	Distance (km)	S_0 ($\text{cm}^2\text{-s}$)	f_c (Hz)
1	4.3		EQ	BAY	1283	2711.2	3.2
				KKL	1118	2530.5	3.3
2	4.3		EQ	KKL	1069	2230.1	3.4
3	4.6		EQ	KKL	1087	1809.6	3.7
4				KSU	642	1205.6	4.2
5	4.6		EQ	BAY	898	5254.0	2.6
				KKL	742	4786.9	2.7
6				BAY	484	54.4	11.9
				KKL	378	48.0	12.4
7			EQ	BAY	977	1491.6	3.9
8				KKL	499	122.4	9.1
9	4.4		EQ	BAY	1047	1908.6	3.6
				KKL	956	2239.6	3.4
				KSU	724	1778.2	3.7
10			EQ	BAY	934	304.5	6.7
				KKL	825	276.9	6.9
11		2.6	EX	BAY	386	47.6	12.4
				KKL	399	47.0	12.5
12							
13		2.5	EX	BAY	456	54.4	11.9
				KKL	309	41.2	13.0
				KSU	436	32.3	14.1
14		2.3	EX	BAY	555	29.2	14.6
				KSU	199	28.0	14.8
15				KKL	492	205.8	7.6
				KSU	242	104.5	9.6
16		2.6	EX	KSU	644	48.6	12.3
17			EQ	BAY	1105	1549.1	3.9
				KKL	996	1575.5	3.9
				KSU	777	1472.3	4.0
18		2.5	EX	KSU	577	74.7	10.7
19		2.9	EX	BAY	246	63.5	11.3
				KKL	253	116.5	9.2
				KSU	636	62.8	11.3
20		2.9	EX	BAY	246	72.1	10.8
				KKL	253	141.4	8.6
				KSU	636	73.6	10.7
21		2.9	EX	BAY	477	77.6	10.6

Event 1

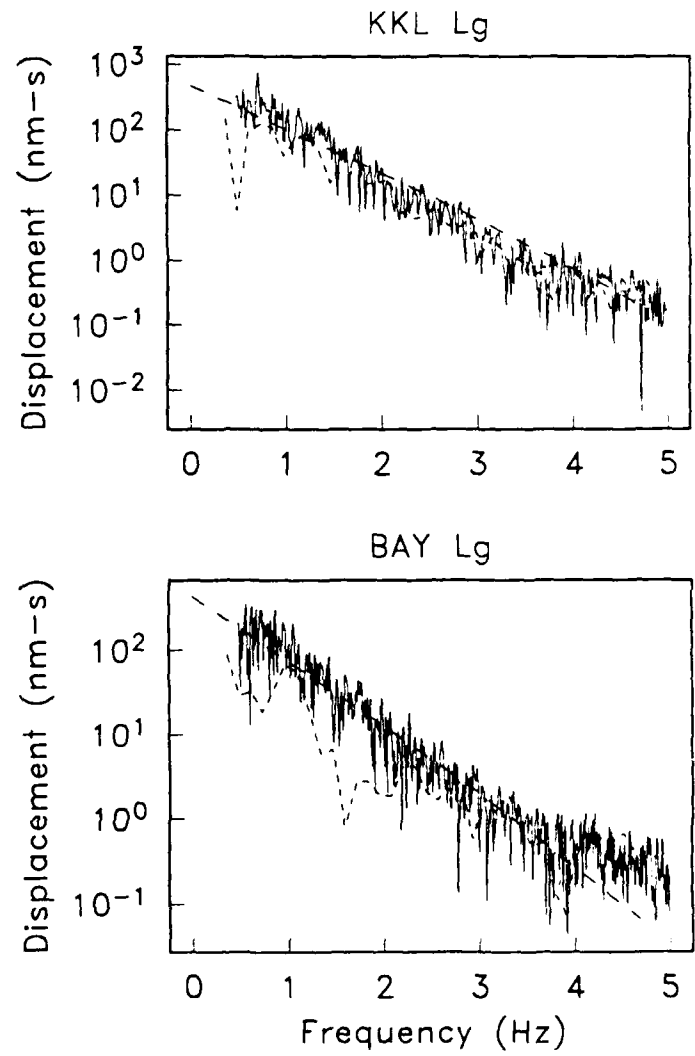


Figure B.1. Spectra for Event 1 (Table 3.2). See text for explanation.

Event 2

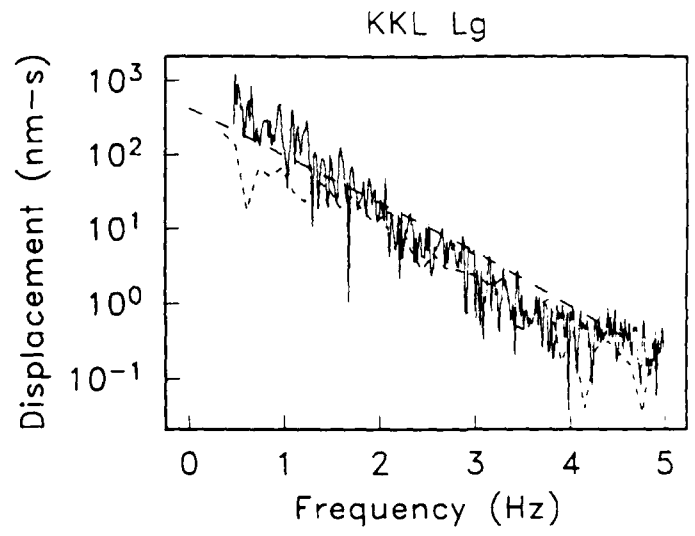


Figure B.2. Spectra for Event 2 (Table 3.2). See text for explanation.

Event 3

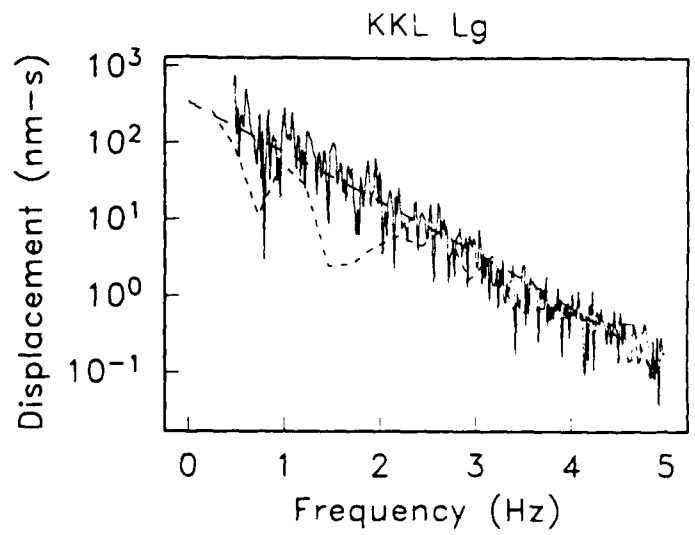


Figure B.3. Spectra for Event 3 (Table 3.2). See text for explanation.

Event 4

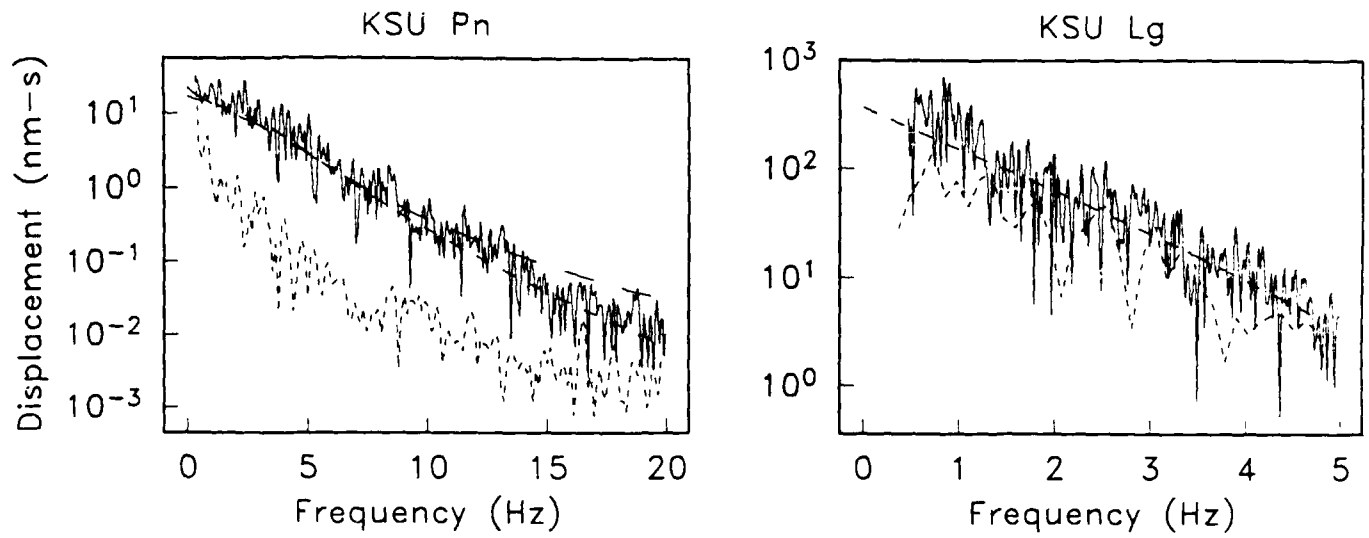


Figure B.4. Spectra for Event 4 (Table 3.2). See text for explanation.

Event 5

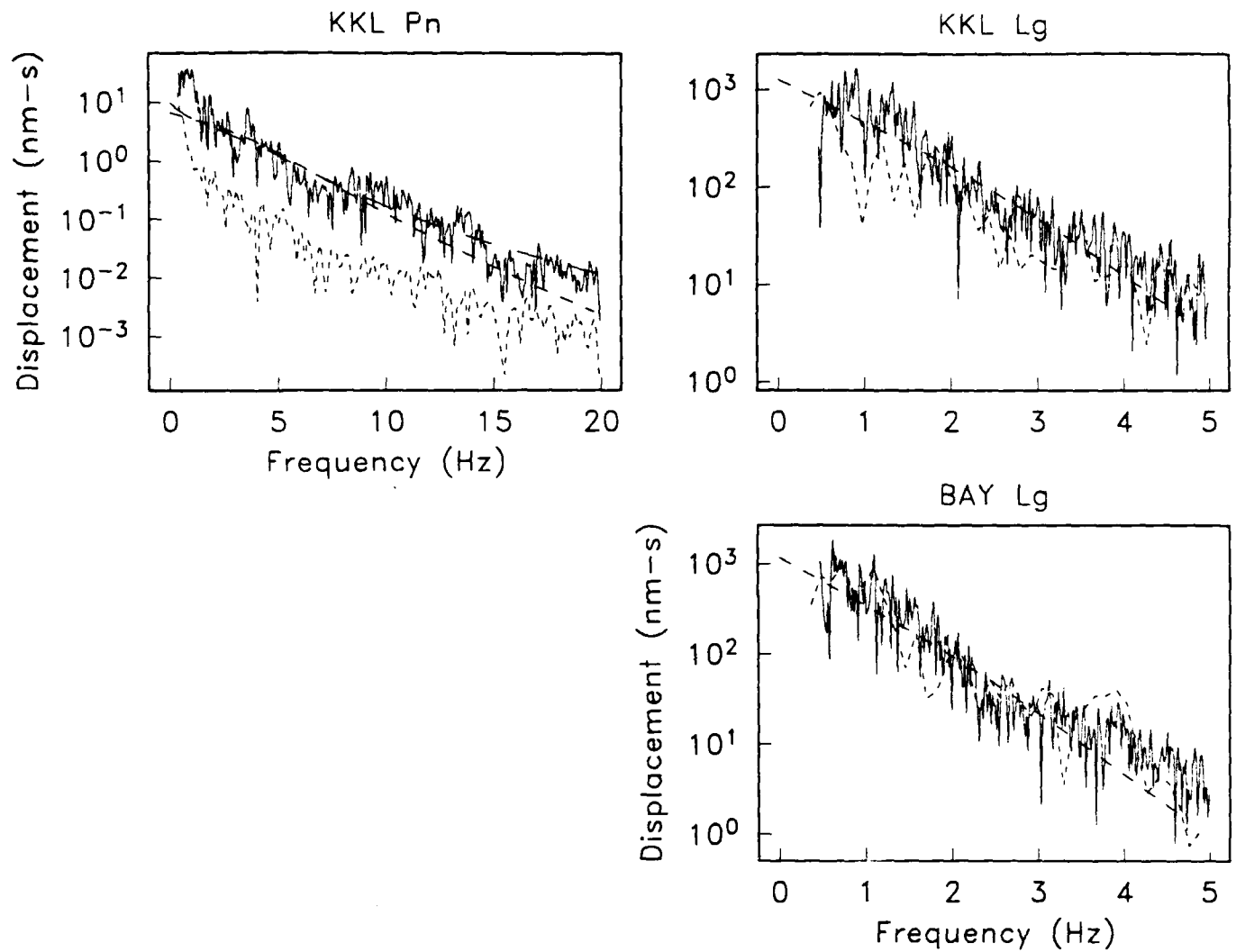


Figure B.5. Spectra for Event 5 (Table 3.2). See text for explanation.

Event 6

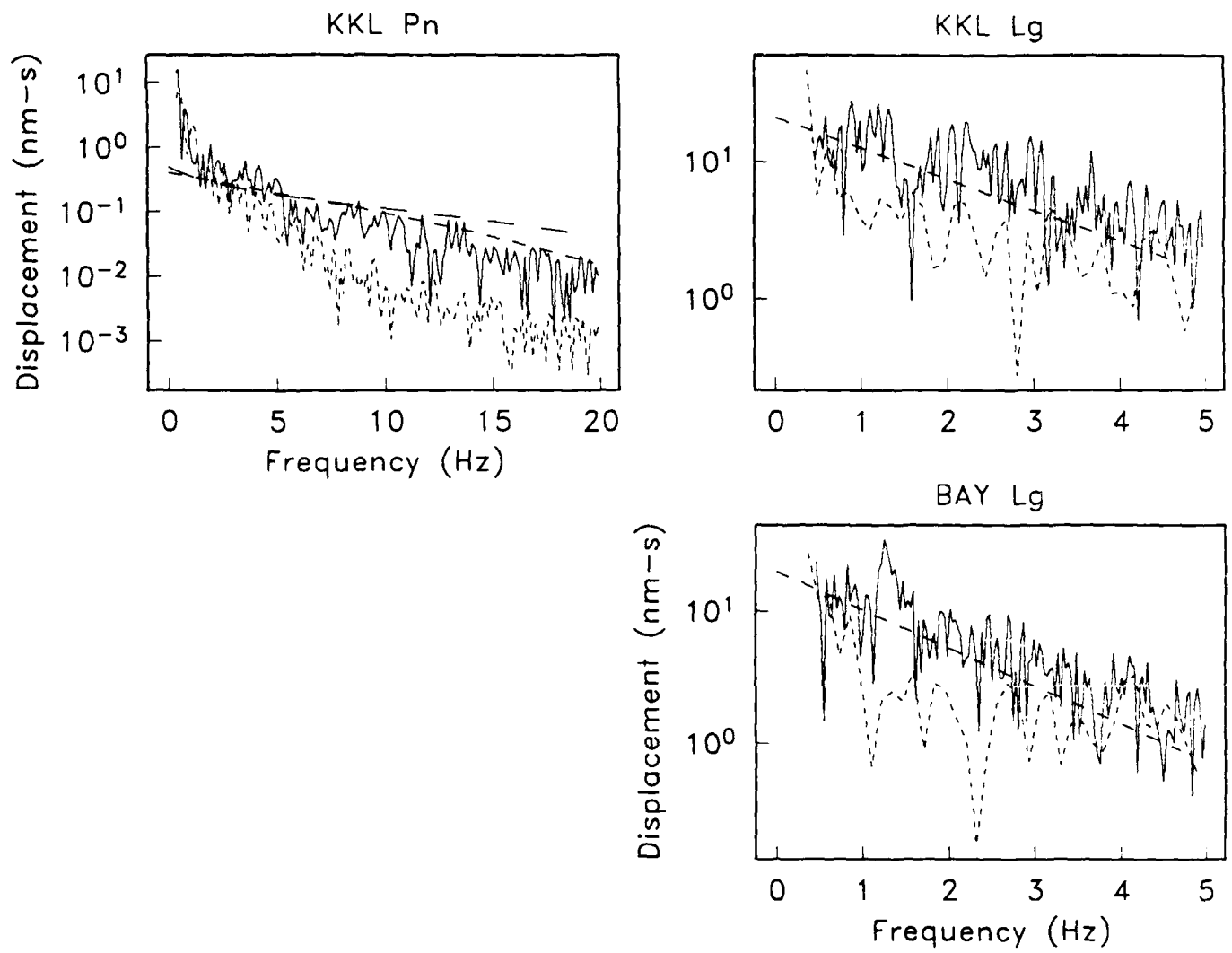


Figure B.6. Spectra for Event 6 (Table 3.2). See text for explanation.

Event 7

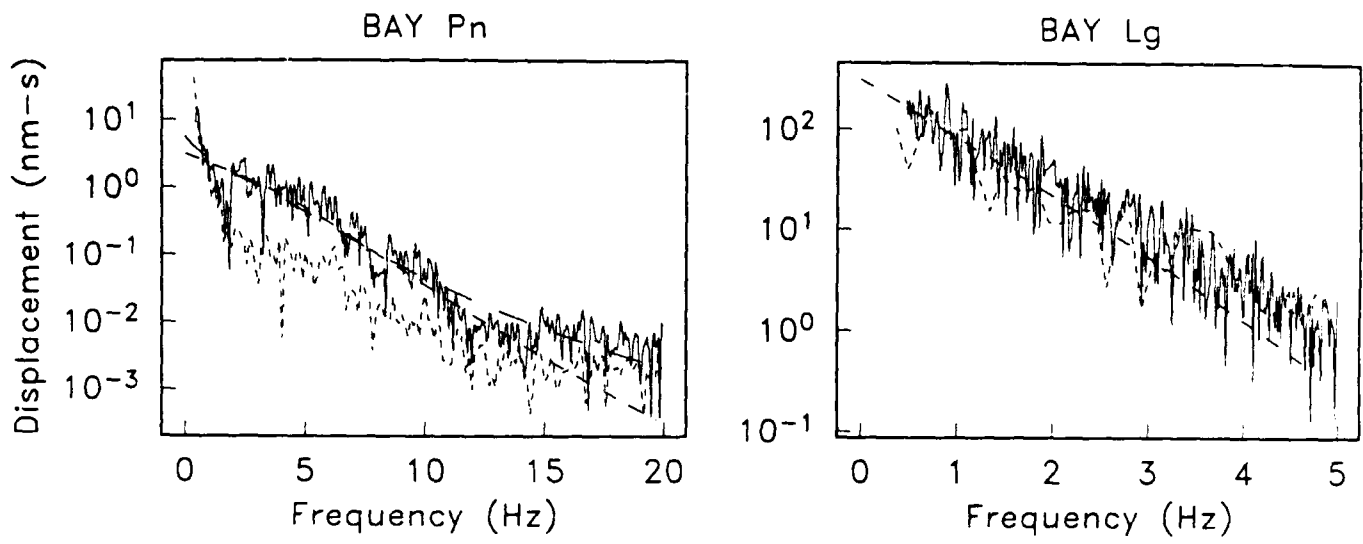


Figure B.7. Spectra for Event 7 (Table 3.2). See text for explanation.

Event 8

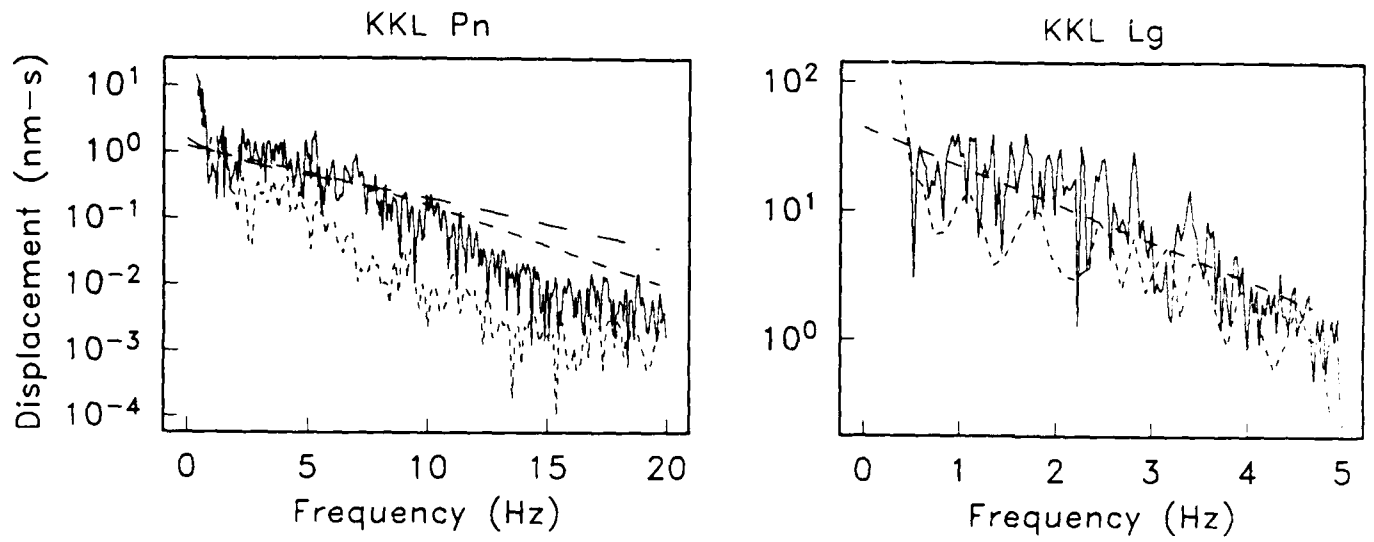


Figure B.8. Spectra for Event 8 (Table 3.2). See text for explanation.

Event 9

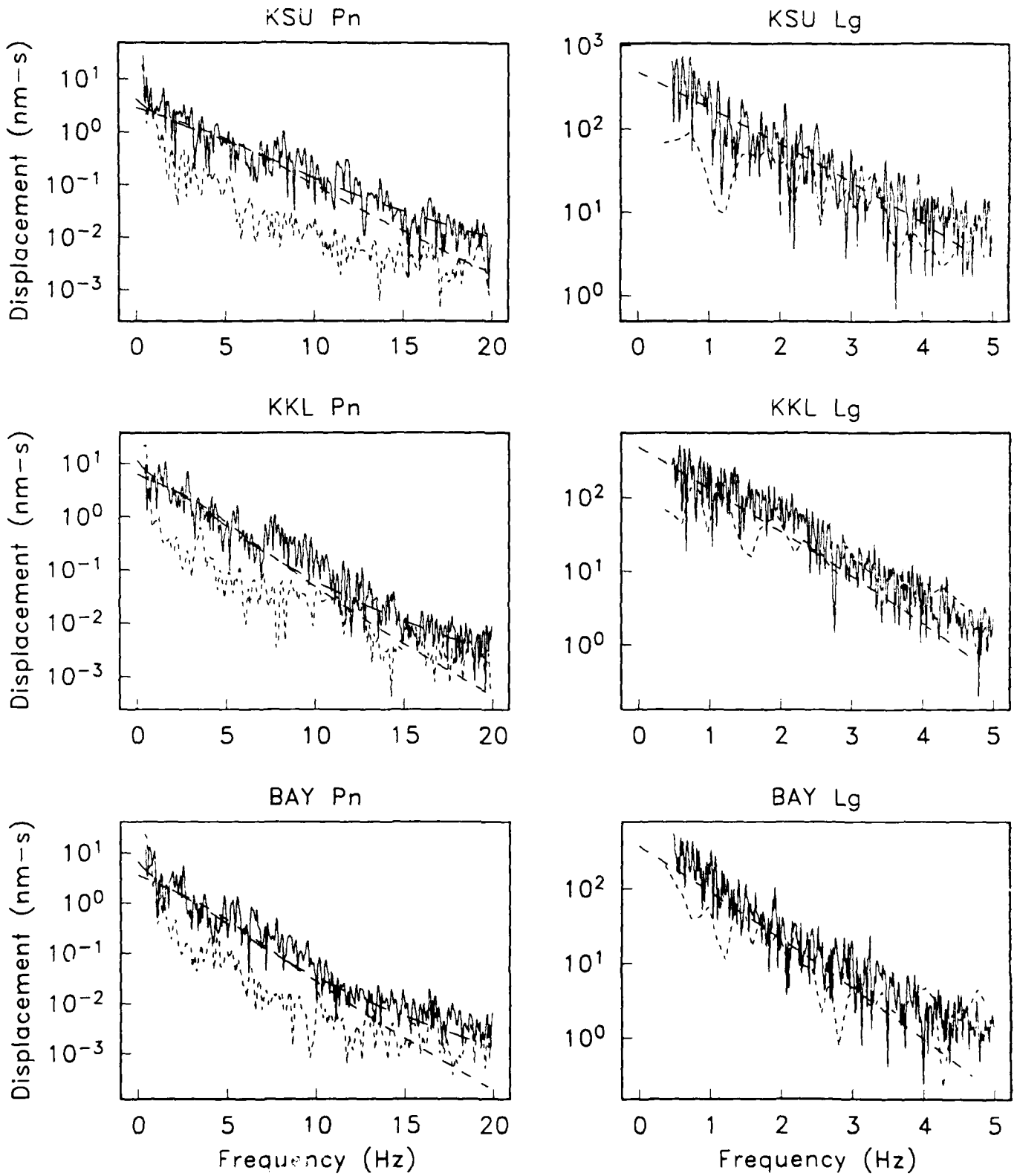


Figure B.9. Spectra for Event 9 (Table 3.2). See text for explanation.

Event 10

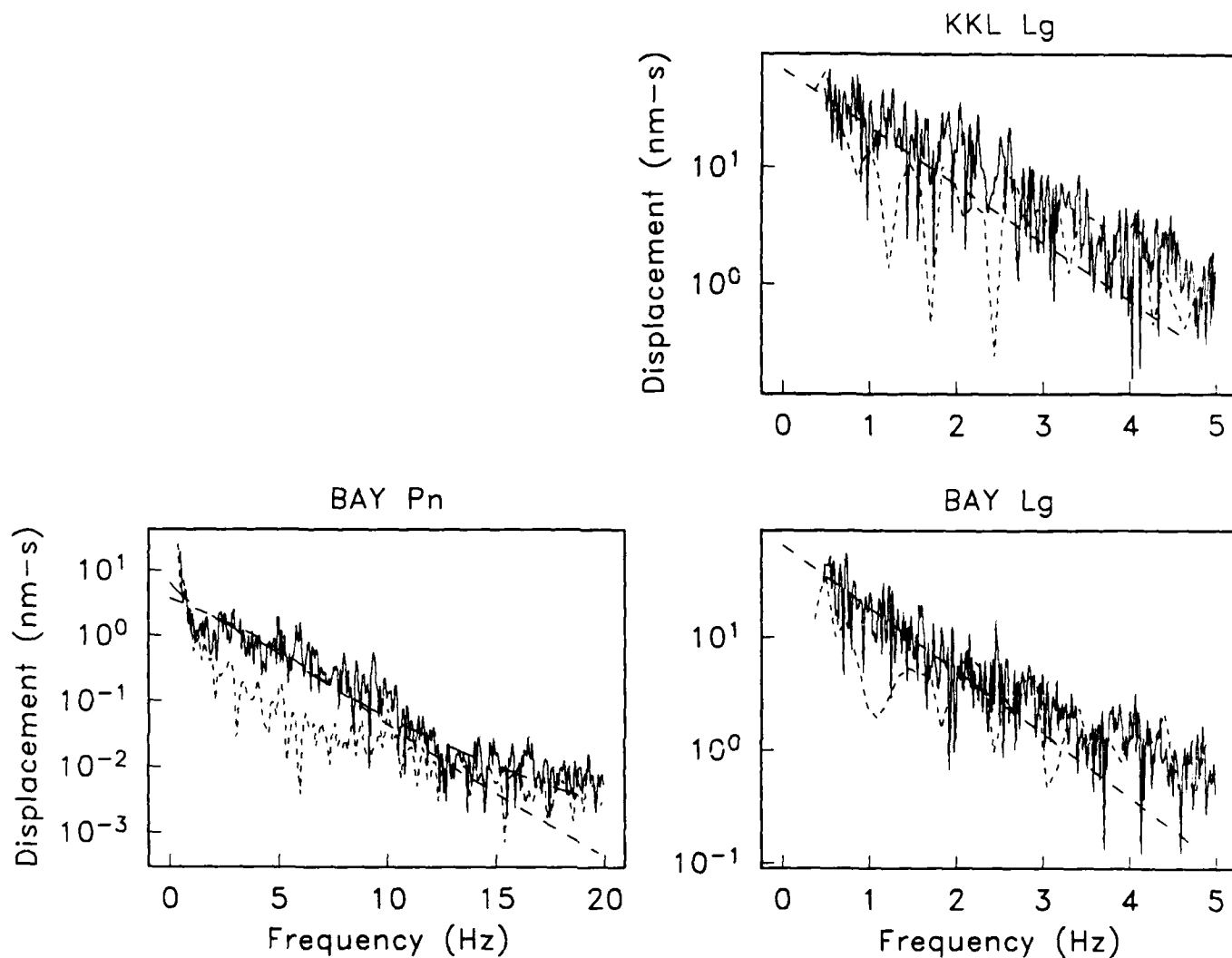


Figure B.10. Spectra for Event 10 (Table 3.2). See text for explanation.

Event 11

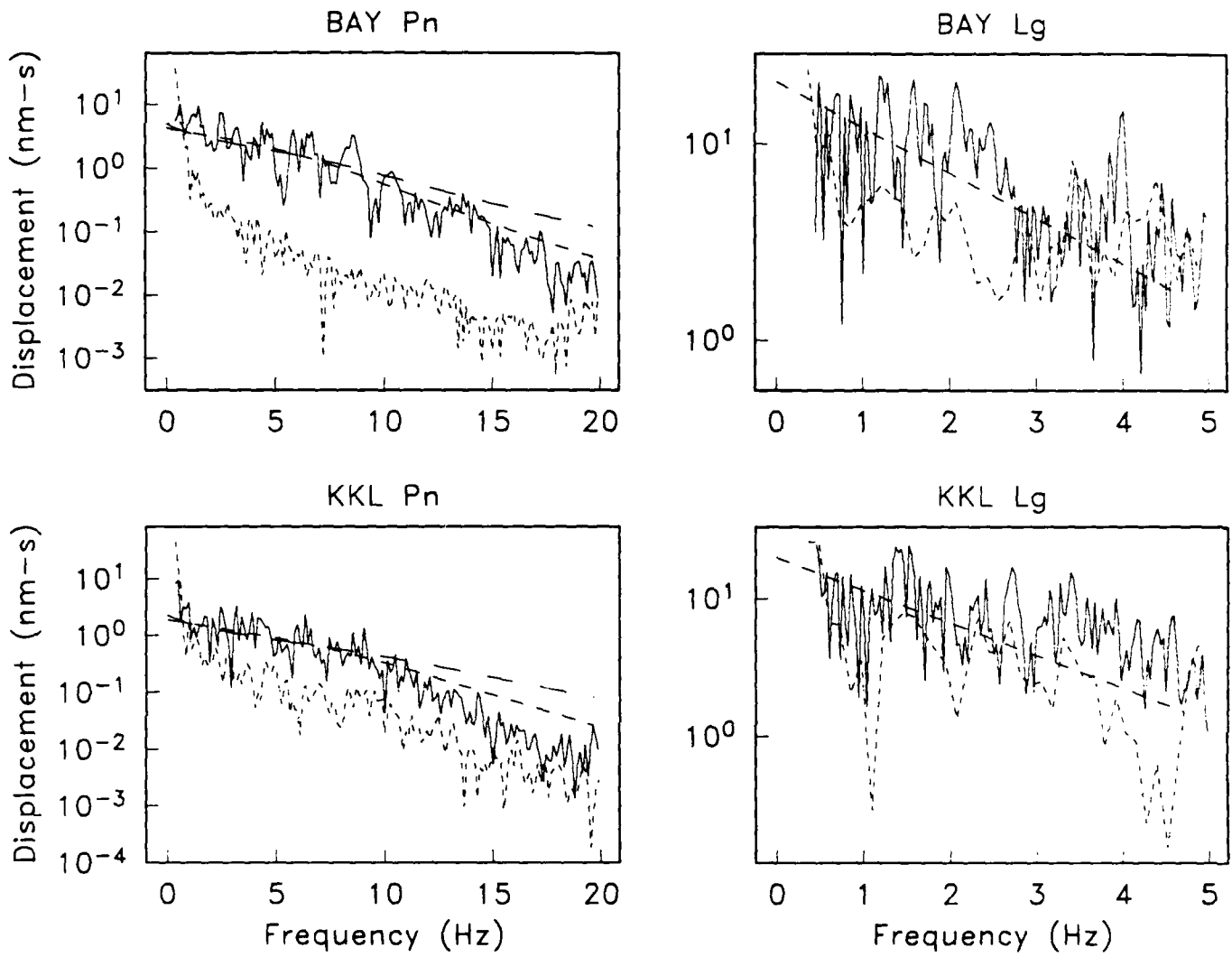


Figure B.11. Spectra for Event 11 (Table 3.2). See text for explanation

Event 12

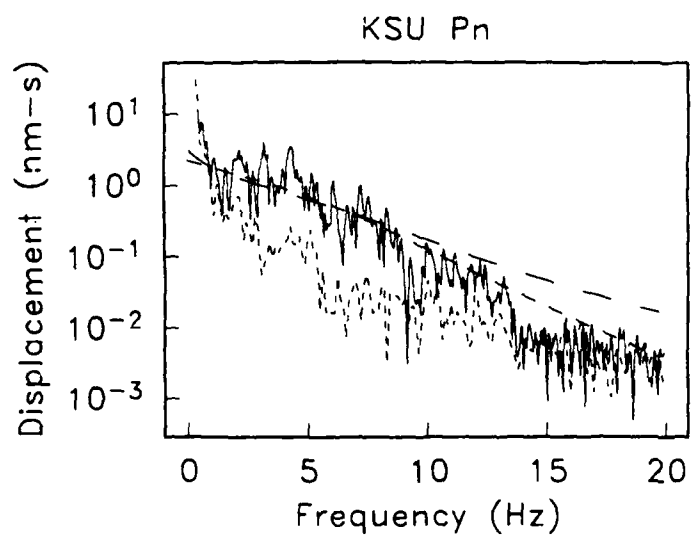


Figure B.12. Spectra for Event 12 (Table 3.2). See text for explanation.

Event 13

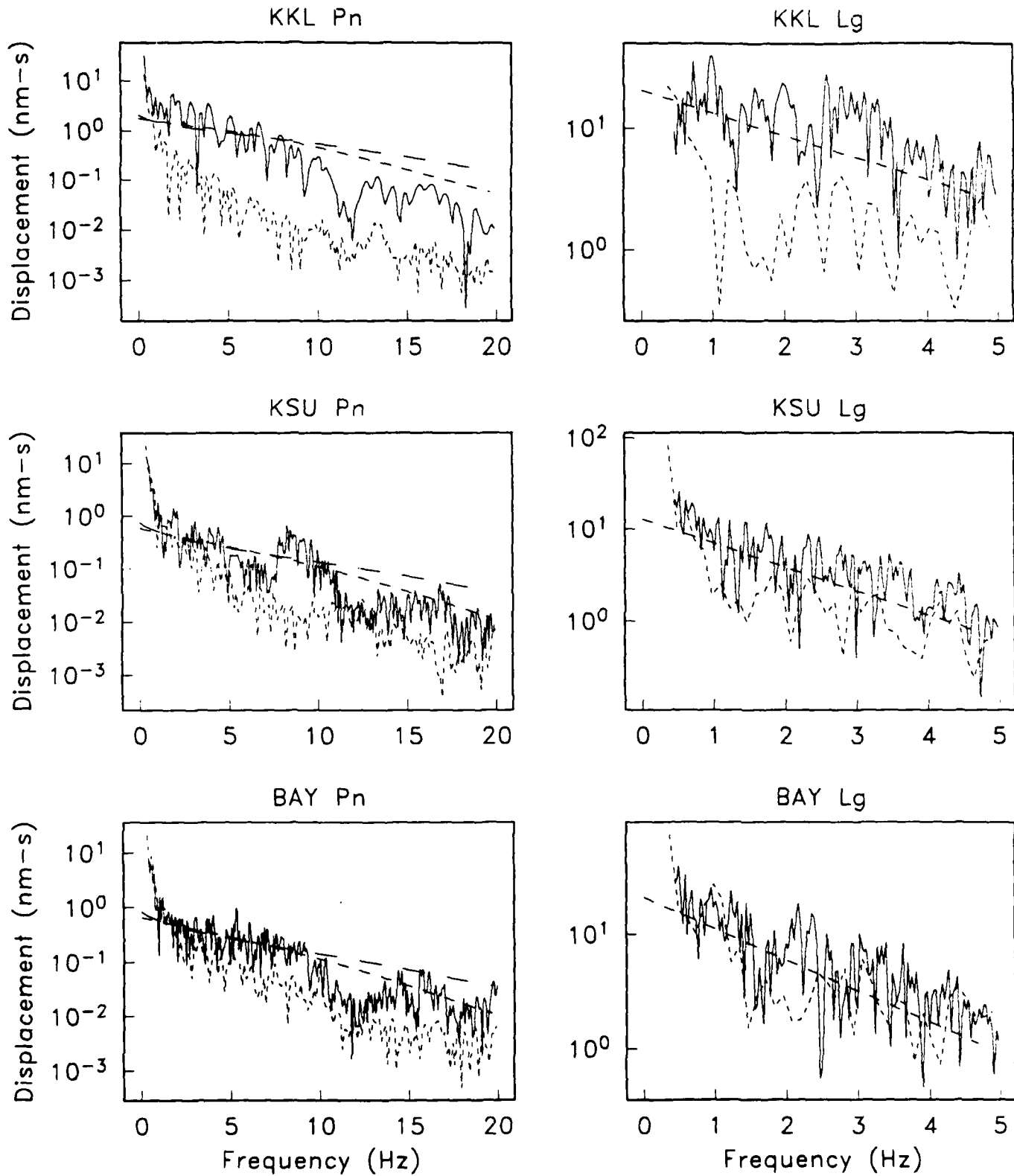


Figure B.13. Spectra for Event 13 (Table 3.2). See text for explanation.

Event 14

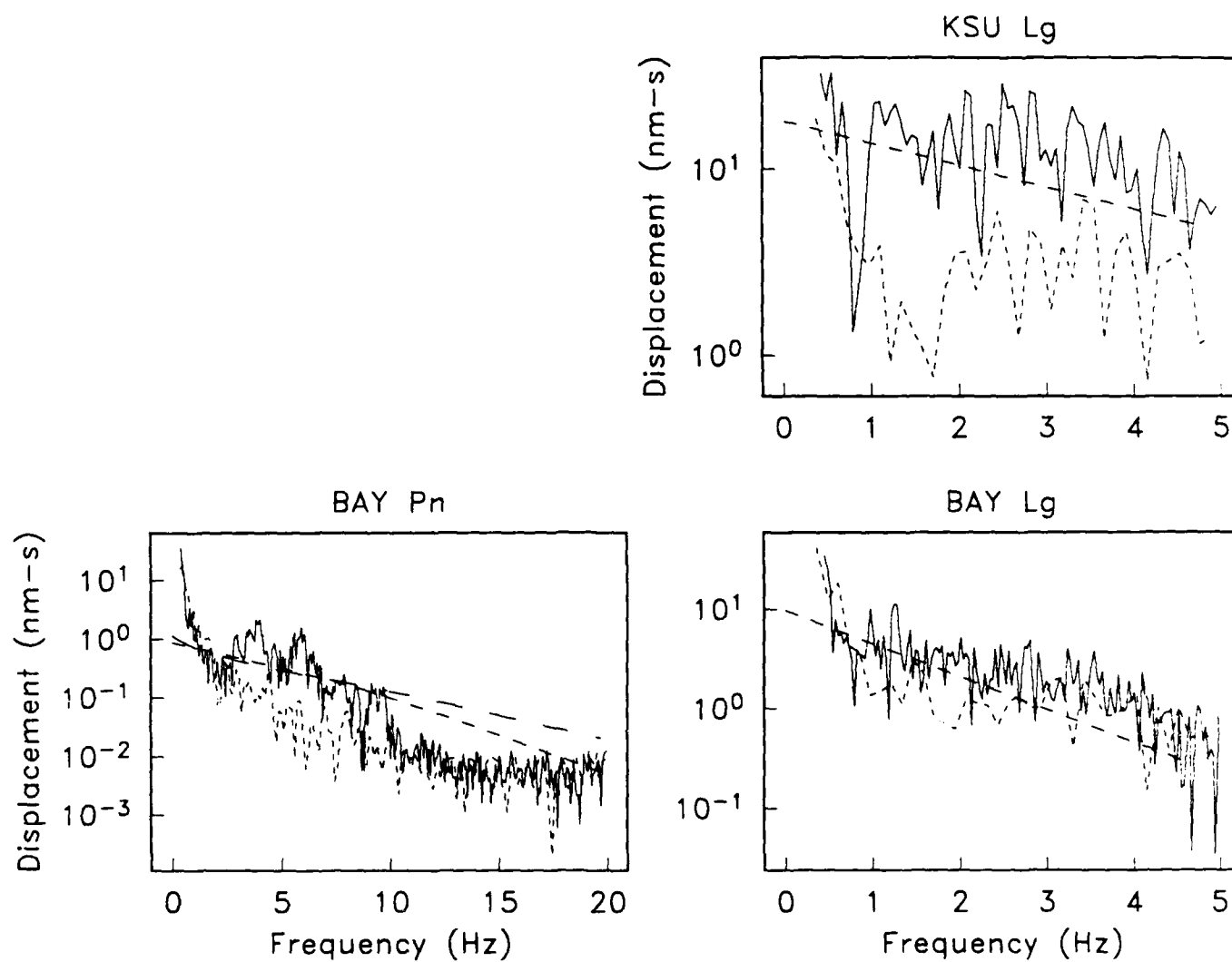


Figure B.14. Spectra for Event 14 (Table 3.2). See text for explanation.

Event 15

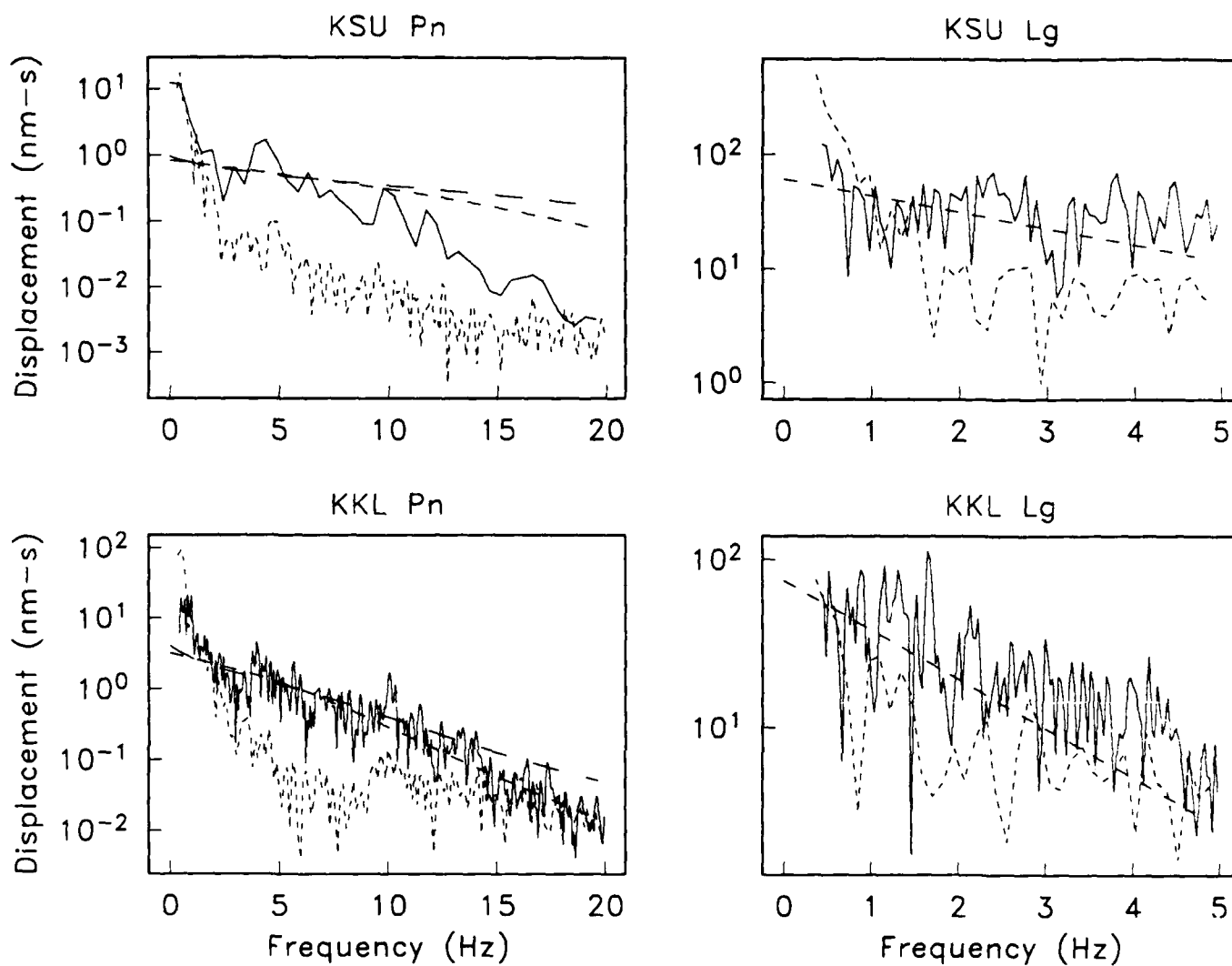


Figure B.15. Spectra for Event 15 (Table 3.2). See text for explanation.

Event 16

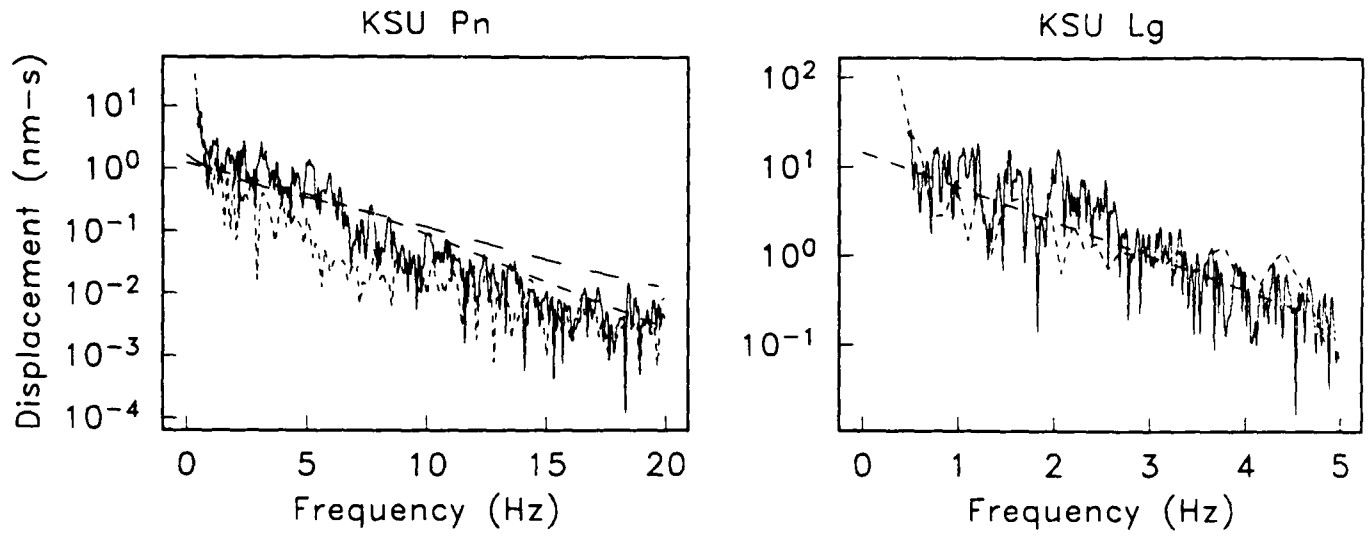


Figure B.16. Spectra for Event 16 (Table 3.2). See text for explanation.

Event 17

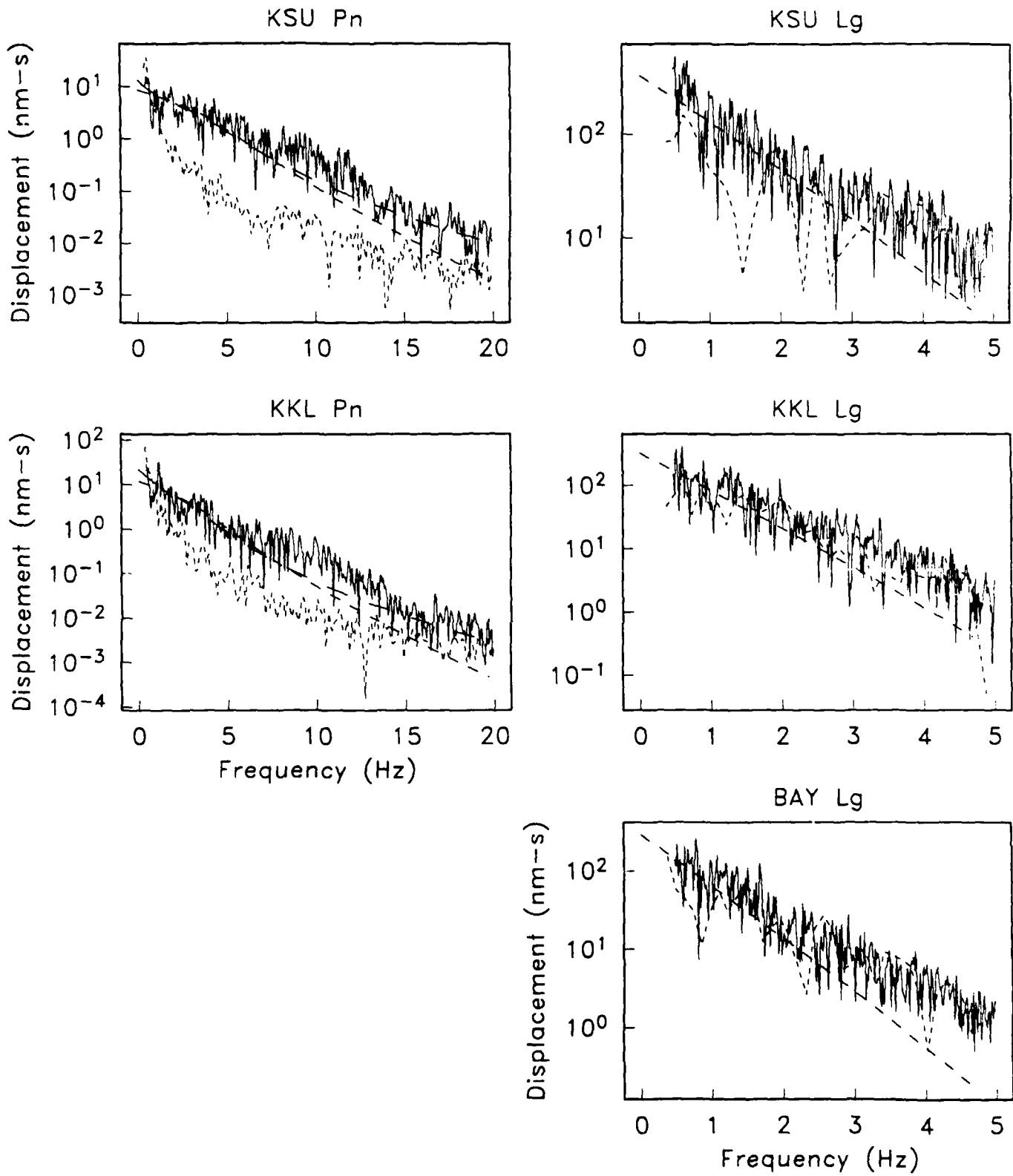


Figure B.17. Spectra for Event 17 (Table 3.2). See text for explanation.

Event 18

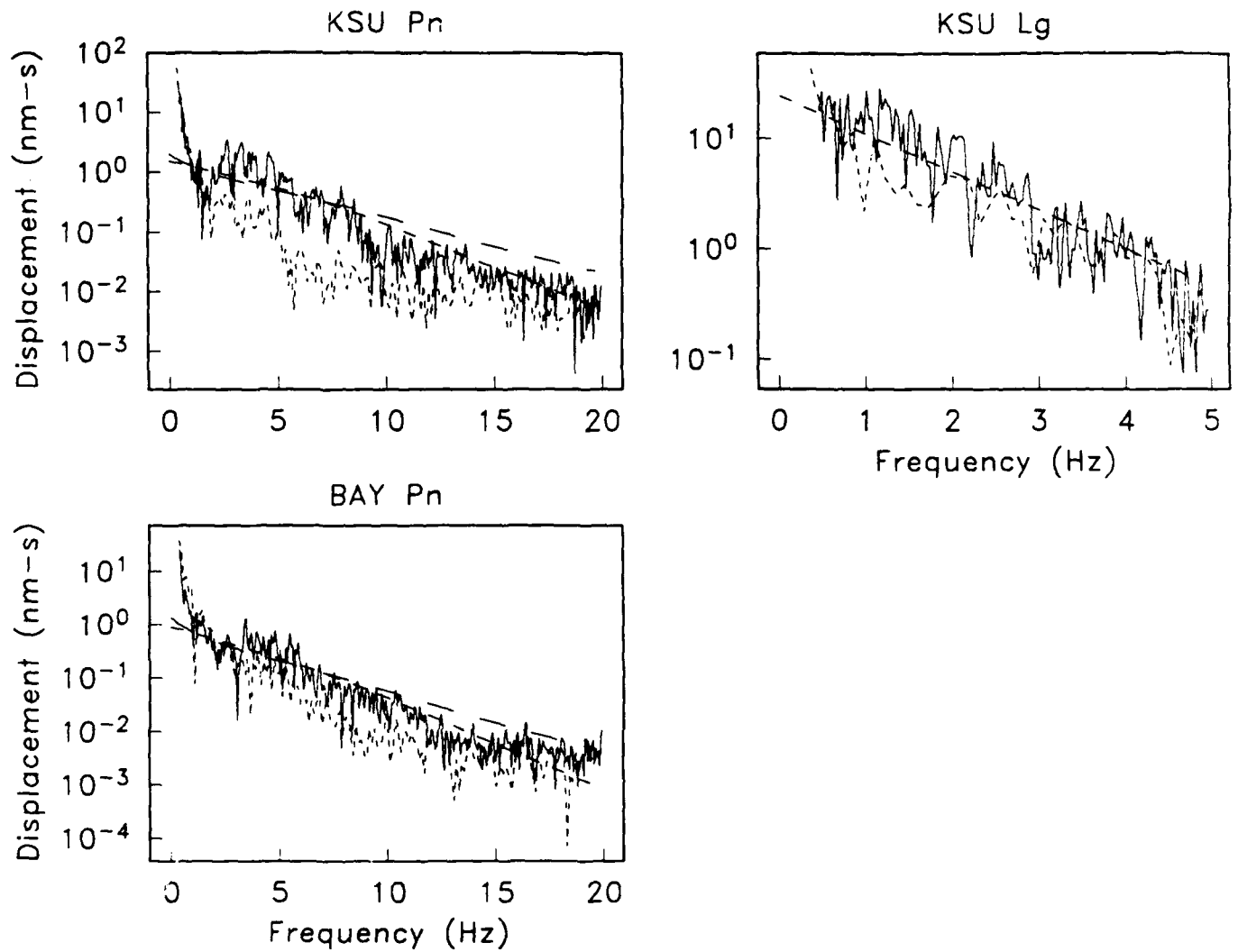


Figure B.18. Spectra for Event 18 (Table 3.2). See text for explanation.

Event 19

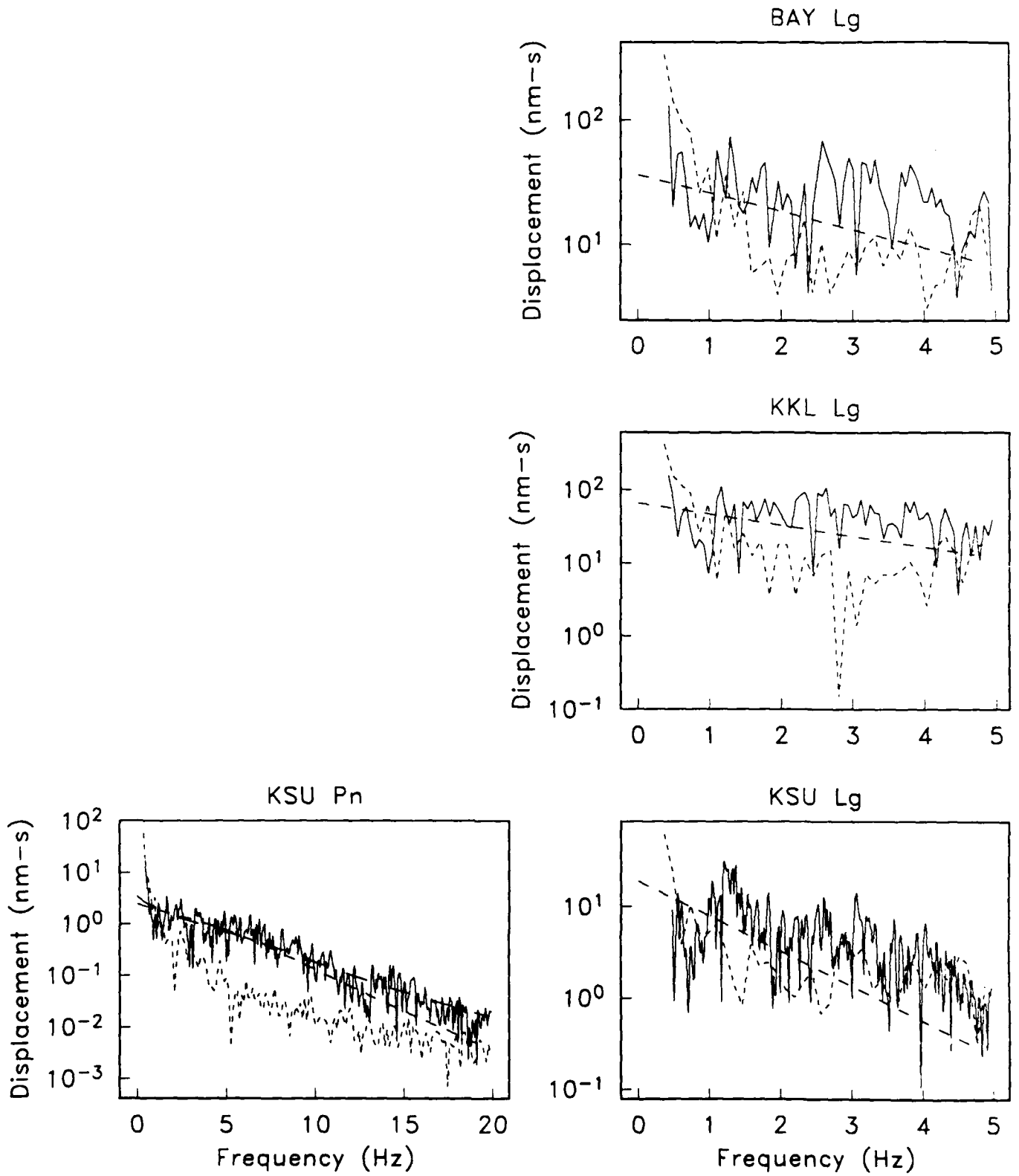


Figure B.19. Spectra for Event 19 (Table 3.2). See text for explanation.

Event 20

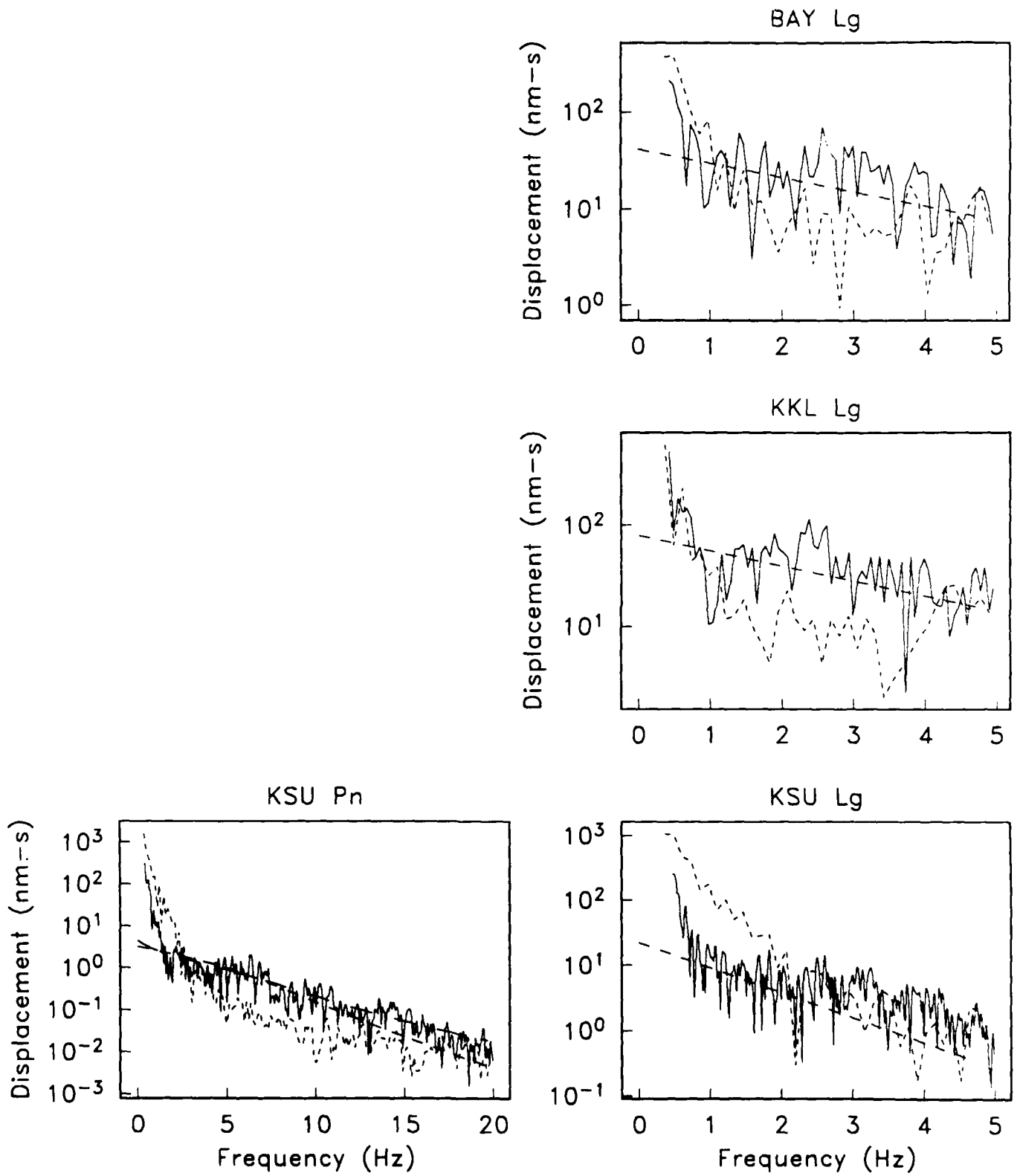


Figure B.20. Spectra for Event 20 (Table 3.2). See text for explanation.

Event 21

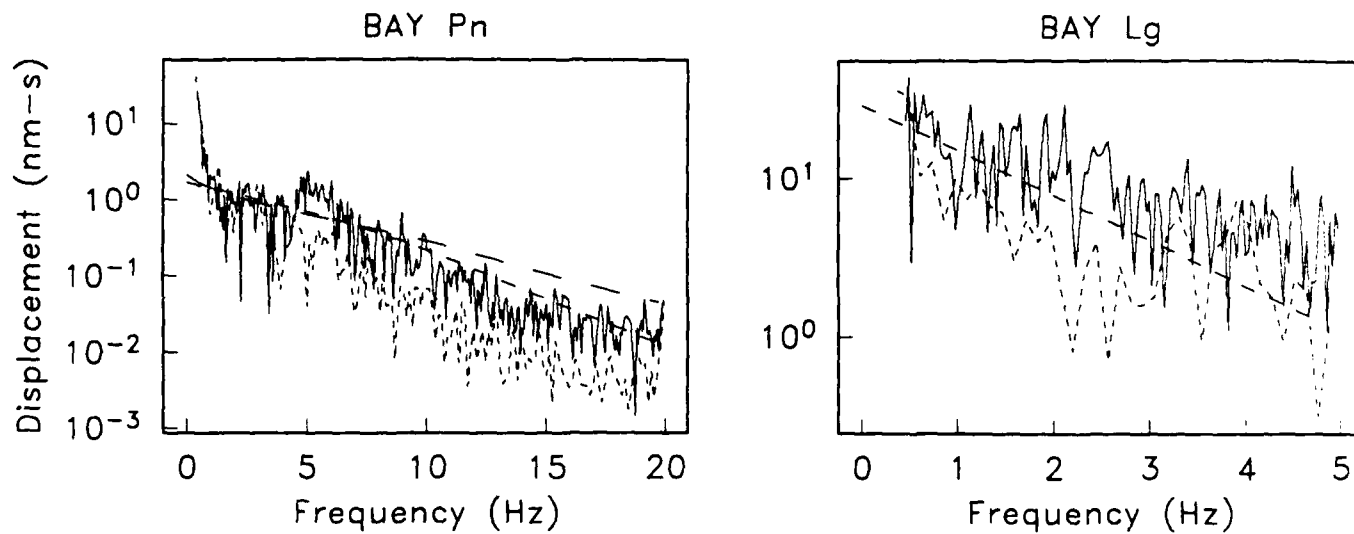


Figure B.21. Spectra for Event 21 (Table 3.2). See text for explanation.

(THIS PAGE INTENTIONALLY LEFT BLANK)

**DISTRIBUTION LIST
FOR UNCLASSIFIED REPORTS
DARPA-FUNDED PROJECTS
(Last Revised: 26 Sep 89)**

RECIPIENT	NUMBER OF COPIES
------------------	-------------------------

DEPARTMENT OF DEFENSE

DARPA/NMRO ATTN: Dr. R. Alewine and Dr. R. Blandford 1400 Wilson Boulevard Arlington, VA 22209-2308	2
Defense Intelligence Agency Directorate for Scientific and Technical Intelligence Washington, D.C. 20340-6158	1
Defense Nuclear Agency Shock Physics Directorate/SD Washington, D.C. 20305-1000	1
Defense Technical Information Center Cameron Station Alexandria, VA 22314	2

DEPARTMENT OF THE AIR FORCE

AFOSR/NP Bldg 410, Room C222 Bolling AFB, Washington, D.C. 20332-6448	1
AFTAC/STINFO Patrick AFB, FL 32925-6001	1
AFTAC/TT Patrick AFB, FL 32925-6001	3
AFWL/NTESG Kirkland AFB, NM 87171-6008	1

GL/LWH 1
ATTN: Mr. J. Lewkowicz
Terrestrial Sciences Division
Hanscom AFB, MA 01731-5000

DEPARTMENT OF THE NAVY

NORDA 1
ATTN Dr. J. A. Ballard
Code 543
NSTL Station, MS 39529

DEPARTMENT OF ENERGY

Department of Energy 1
ATTN: Mr. Max A. Koontz (DP-331)
International Security Affairs
1000 Independence Avenue
Washington, D.C. 20585

Lawrence Livermore National Laboratory 3
ATTN: Dr. J. Hannon, Dr. S. Taylor, and Dr. K. Nakanishi
University of California
P.O. Box 808
Livermore, CA 94550

Los Alamos Scientific Laboratory 2
ATTN: Dr. C. Newton
P.O. Box 1663
Los Alamos, NM 87544

Sandia Laboratories 1
ATTN: Mr. P. Stokes, Dept. 9110
P.O. Box 5800
Albuquerque, NM 87185

OTHER GOVERNMENT AGENCIES

Central Intelligence Agency 1
ATTN: Dr. L. Turnbull
OSI/NED, Room 5G48
Washington, D.C. 20505

U.S. Arms Control and Disarmament Agency 1
ATTN: Dr. M. Eimer
Verification and Intelligence Bureau, Room 4953
Washington, D.C. 20451

U.S. Arms Control and Disarmament Agency 1
ATTN: Mr. R. J. Morrow
Multilateral Affairs Bureau, Rm 5499
Washington, D.C. 20451

U.S. Geological Survey 1
ATTN: Dr. T. Hanks
National Earthquake Research Center
345 Middlefield Road
Menlo Park, CA 94025

U.S. Geological Survey MS-913 1
ATTN: Dr. R. Masse
Global Seismology Branch
Box 25046, Stop 967
Denver Federal Center
Denver, CO 80225

UNIVERSITIES

Boston College 1
ATTN: Dr. A. Kafka
Western Observatory
381 Concord Road
Weston, MA 02193

California Institute of Technology 1
ATTN: Dr. D. Harkrider
Seismological Laboratory
Pasadena, CA 91125

Columbia University 1
ATTN: Dr. L. Sykes
Lamont-Doherty Geological Observatory
Palisades, NY 10964

Cornell University 1
ATTN: Dr. M. Barazangi
INSTOC
Snee Hall
Ithaca, NY 14853

Harvard University ATTN: Dr. J. Woodhouse Hoffman Laboratory 20 Oxford Street Cambridge, MA 02138	1
Massachusetts Institute of Technology ATTN: Dr. S. Soloman, Dr. N. Toksoz, and Dr. T. Jordon Department of Earth and Planetary Sciences Cambridge, MA 02139	3
Southern Methodist University ATTN: Dr. E. Herrin and Dr. B. Stump Geophysical Laboratory Dallas, TX 75275	2
State University of New York at Binghamton ATTN: Dr. F. Wu Department of Geological Sciences Vestal, NY 13901	1
St. Louis University ATTN: Dr. B. Mitchell and Dr. R. Herrmann Department of Earth and Atmospheric Sciences 3507 Laclede St. Louis, MO 63156	2
The Pennsylvania State University ATTN: Dr. S. Alexander Geosciences Department 403 Deike Building University Park, PA 16802	1
University of Arizona ATTN: Dr. T. Wallace Department of Geosciences Tucson, AZ 85721	1
University of California, Berkeley ATTN: Dr. T. McEvilly Department of Geology and Geophysics Berkeley, CA 94720	1
University of California, Los Angeles ATTN: Dr. L. Knopoff 405 Hilgard Avenue Los Angeles, CA 90024	1

University of California, San Diego 1
ATTN: Dr. J. Orcutt
Scripps Institute of Oceanography
La Jolla, CA 92093

University of Colorado 1
ATTN: Dr. C. Archambeau
CIRES
Boulder, CO 80309

University of Illinois 1
ATTN: Dr. S. Grand
Department of Geology
1301 West Green Street
Urbana, IL 61801

University of Michigan 1
ATTN: Dr. T. Lay
Department of Geological Sciences
Ann Arbor, MI 48109-1063

University of Nevada 1
ATTN: Dr. K. Priestley
Mackay School of Mines
Reno, NV 89557

University of Southern California 1
ATTN: Dr. K. Aki
Center for Earth Sciences
University Park
Los Angeles, CA 90089-0741

DEPARTMENT OF DEFENSE CONTRACTORS

Analytical Sciences Corporation, The 1
Dr. Richard Sailor
ATTN: Document Control
55 Walkers Brook Drive
Reading, MA 01867

Applied Theory, Inc. 1
ATTN: Dr. J. Trulio
930 South La Brea Avenue
Suite 2
Los Angeles, CA 90036

Center for Seismic Studies ATTN: Dr. C. Romney and Mr. R. Perez 1300 N. 17th Street, Suite 1450 Arlington, VA 22209	2
ENSCO, Inc. ATTN: Mr. John R. Stevenson P.O. Box 1346 Springfield, VA 22151	1
ENSCO, Inc. ATTN: Dr. R. Kemerait 445 Pineda Court Melbourne, FL 32940-7508	1
Gould Inc. ATTN: Mr. R. J. Woodard Chesapeake Instrument Division 6711 Baymeado Drive Glen Burnie, MD 21061	1
Maxwell Laboratories Inc. S-CUBED Reston Geophysics Office ATTN: Mr. J. Murphy, Suite 1112 11800 Sunrise Valley Drive Reston, VA 22091	1
Pacific Sierra Research Corp. ATTN: Mr. F. Thomas 12340 Santa Monica Boulevard Los Angeles, CA 90025	1
Rockwell International ATTN: B. Tittmann 1049 Camino Dos Rios Thousand Oaks, CA 91360	1
Roudout Associates, Inc. ATTN: Dr. P. Pomeroy P.O. Box 224 Stone Ridge, NY 12484	1
Science Applications International Corporation ATTN: Document Control (Dr. T. Bache, Jr.) 10260 Campus Point Drive San Diego, CA 92121	1

Science Horizons 2
ATTN: Dr. T. Cherry and Dr. J. Minster
710 Encinitas Blvd.
Suite 101
Encinitas, CA 92024

S-CUBED, A Division of Maxwell 1
Laboratories, Inc.
ATTN: Dr. Keith L. McLaughlin
P.O. Box 1620
La Jolla, CA 92038-1620

Sierra Geophysics, Inc. 2
ATTN: Dr. R. Hart and Dr. G. Mellman
11255 Kirkland Way
Kirkland, WA 98033

SRI International 1
ATTN: Dr. A. Florence
333 Ravenswood Avenue
Menlo Park, CA 94025

Teledyne Industries Inc. 1
Teledyne Geotech Alexandria Laboratories
ATTN: Mr. W. Rivers
314 Montgomery Street
Alexandria, VA 22314-1581

Woodward-Clyde Consultants 1
ATTN: Dr. L. Burdick
P.O. Box 93254
Pasadena, CA 91109-3254

NON-US RECIPIENTS

Blacknest Seismological Center 1
ATTN: Mr. Peter Marshall
Atomic Weapons Research Establishment
UK Ministry of Defense
Brimpton, Reading RG7-4RS
United Kingdom

National Defense Research Institute 1
ATTN: Dr. Ola Dahlman
Stockholm 80, Sweden

NTNF NORSAR
ATTN: Dr. Frode Ringdal
P.O. Box 51
N-2007 Kjeller
Norway

1

OTHER DISTRIBUTION

To be determined by the project office

9

TOTAL 81